SEARCH FOR EXOTIC SPIN COUPLINGS WITH THE GLOBAL NETWORK OF OPTICAL MAGNETOMETERS FOR EXOTIC PHYSICS SEARCHES

By

Hector Masia Roig

born in Alzira (Valencia) Spain

Dissertation submitted
for the award of the title "Doctor of Natural Sciences"
to the Faculty of Physics, Mathematics, and Computer Science of
Johannes Gutenberg University Mainz

Mainz, May 2023

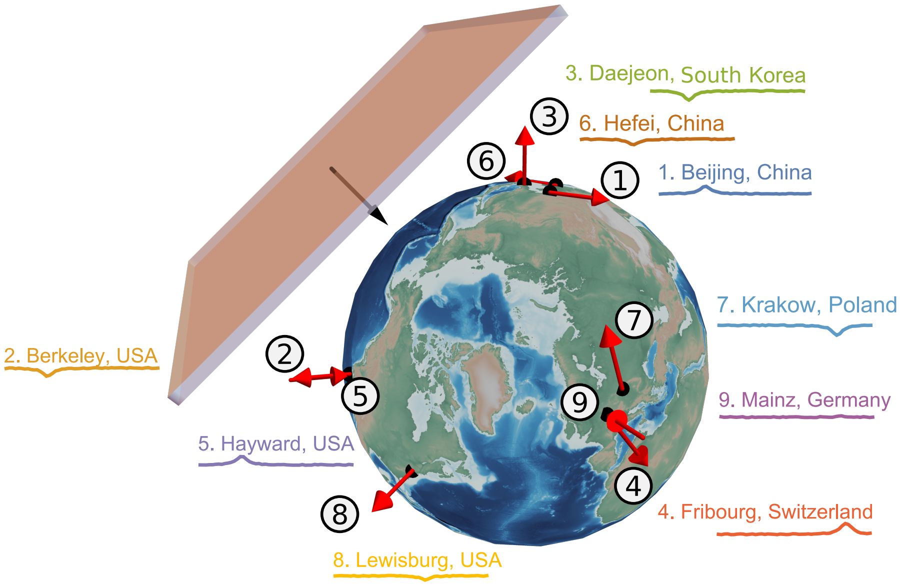

Dedicated to my parents
for their unconditional love and support

ABSTRACT

Current evidence indicates that Standard Model particles and interactions constitute just 4.9% of the energy content in the universe. The largest contribution, 68.3%, is attributed to dark energy, while the rest, 26.8%, is attributed to dark matter. Such an invisible and unidentified matter was postulated to interpret otherwise inexplicable gravitational effects at galactic and larger scales. Even though one could think that everything is known, these percentages emphasize the still huge room for discovery.

Decades of research have not yet been able to identify the nature of dark matter. This inconclusive record is pressing the physics community to find increasingly original and unconventional ideas. The Global Network of Optical Magnetometers for Exotic physics searches (GNOME) surged in an effort to explore unorthodox scenarios.

GNOME is a synchronized network of globally distributed spin-sensitive magnetometers. In other words, an Earth-sized observatory for exotic physics. Its sensors rely on couplings to electron, proton, and/or neutron spins, while its size makes the network well-suited to search for exotic fields with spatial and/or directional dependence.

Axions or more generally axion-like particles (ALPs) are light to ultralight hypothetical bosons that could explain dark matter observations. Under some assumptions, such particles can clump and form structures at sub-galactic scales. Additionally, their possible interactions include couplings to fermionic spins. These properties make GNOME sensitive to such particles.

This thesis is devoted to the search for ALP domain-wall signatures. The ALP field can form 2-dimensional topological defects at sub-galactic scales called domain walls. Earth could encounter such planar structures while traveling through our galaxy. In case of an encounter, a distinctive pattern would be imprinted in the network. An algorithm was developed to identify such patterns, calculate the significance, and evaluate the sensitivity. In an effort to extend the capabilities of GNOME, the possibility of searching for stochastic properties of an axion-like particle background field was also explored.

ZUSAMMENFASSUNG

Die derzeitigen Erkenntnisse deuten darauf hin, dass die Teilchen und Wechselwirkungen des Standardmodells nur 4,9% des Energiegehalts im Universum ausmachen. Der größte Beitrag (68,3%) wird der dunklen Energie zugeschrieben, während der Rest (26,8%) der dunklen Materie zugerechnet wird. Diese unsichtbare und nicht identifizierte Materie wurde postuliert, um ansonsten unerklärliche Gravitationseffekte auf galaktischen und größeren Skalen zu erklären.

Auch wenn man meinen könnte, dass alles bekannt ist, machen diese Prozentzahlen deutlich, dass es noch viel zu entdecken gibt.

Jahrzehntelange Forschung konnte die Beschaffenheit der dunklen Materie noch nicht bestimmen. Dieser nicht schlüssige Befund zwingt die Physik dazu, immer originellere und unkonventionellere Ideen zu entwickeln. Das Globale Netzwerk Optischer Magnetometer für die Suche nach exotischer Physik (GNOME) wurde ins Leben gerufen, um unorthodoxen Szenarien zu untersuchen.

GNOME ist ein synchronisiertes Netzwerk global verteilter spinempfindlicher Magnetometer. Mit anderen Worten: ein erdgroßes Observatorium für exotische Physik. Dessen Sensoren beruhen auf Kopplungen mit Elektronen-, Protonen- und/oder Neutronenspins und aufgrund seiner Größe eignet sich das Netzwerk gut für die Suche nach exotischen Feldern mit Orts- und/oder Richtungsabhängigkeit.

Axione oder allgemeiner axionähnliche Teilchen (ALPs aus dem englischen axion-like particles) sind leichte bis ultraleichte hypothetische Bosonen, die Beobachtungen der dunklen Materie erklären könnten. Unter bestimmten Annahmen können solche Teilchen verklumpen und Strukturen auf subgalaktischen Skalen bilden. Darüber hinaus umfassen ihre möglichen Wechselwirkungen Kopplungen mit fermionischen Spins. Diese Eigenschaften machen GNOME empfindlich für solche Teilchen.

Diese Arbeit widmet sich der Suche nach Signaturen von ALP-Domänenwänden. Das ALP-Feld kann 2-dimensionale topologische Defekte auf subgalaktischen Skalen bilden, die Domänenwände genannt werden. Die Erde könnte auf ihrer Reise durch unsere Galaxie auf solche Strukturen treffen. Im Falle einer Begegnung würde sich ein charakteristisches Muster in das Netzwerk einprägen. Es wurde ein Algorithmus entwickelt, um solche Muster zu erkennen, ihre Bedeutung zu berechnen und ihre Empfindlichkeit zu bewerten. Um die Fähigkeiten von GNOME zu erweitern, wurde auch untersucht, ob es möglich ist, nach stochastischen Eigenschaften eines axionartigen Teilchenhintergrundfeldes zu suchen.

PUBLICATIONS

[1] Hector Masia-Roig et al. "Intensity interferometry for ultralight bosonic dark matter detection." In: (Feb. 2022). arXiv: `2202.02645 [hep-ph]`.

[2] Samer Afach et al. "Search for topological defect dark matter with a global network of optical magnetometers." In: *Nature Physics* 17.12 (Dec. 2021), pp. 1396–1401. ISSN: 1745-2481. DOI: `10.1038/s41567-021-01393-y`. URL: `https://doi.org/10.1038/s41567-021-01393-y`.

[3] Hector Masia-Roig et al. "Analysis method for detecting topological defect dark matter with a global magnetometer network." In: *Phys. Dark Universe* 28 (May 2020), p. 100494. ISSN: 22126864. DOI: `10.1016/j.dark.2020.100494`. URL: `https://linkinghub.elsevier.com/retrieve/pii/S2212686419303760` (visited on 02/17/2020).

[4] Dongok Kim, Derek F. Jackson Kimball, Hector Masia-Roig, Joseph A. Smiga, Arne Wickenbrock, Dmitry Budker, Younggeun Kim, Yun Chang Shin, and Yannis K. Semertzidis. "A machine learning algorithm for direct detection of axion-like particle domain walls." In: *Physics of the Dark Universe* 37 (2022), p. 101118. ISSN: 2212-6864. DOI: `https://doi.org/10.1016/j.dark.2022.101118`. URL: `https://www.sciencedirect.com/science/article/pii/S2212686422000917`.

[5] S Afach, Dmitry Budker, G DeCamp, Vincent Dumont, Zoran Dragan Grujić, H Guo, DF Jackson Kimball, TW Kornack, Victor Lebedev, W Li, et al. "Characterization of the global network of optical magnetometers to search for exotic physics (GNOME)." In: *Phys. Dark Universe* 22 (2018), pp. 162–180.

[6] Runqi Han, Mikhail Balabas, Chris Hovde, Wenhao Li, Hector Masia Roig, Tao Wang, Arne Wickenbrock, Elena Zhivun, Zheng You, and Dmitry Budker. "Is light narrowing possible with dense-vapor paraffin coated cells for atomic magnetometers?" In: *AIP Advances* 7.12 (2017), p. 125224. DOI: `10.1063/1.4997691`.

One always finds in the last place where one looks

ACKNOWLEDGMENTS

My drive for science and research began with my parents. I am very grateful to them. They always allowed me free room to develop my creativity and interests. They encouraged me to learn a lot. Not what could be seen as "useful" but what I most enjoyed. I will always remember that my mother after a long day of work helped me to finish the infinite multiplication tables that I had for homework in school. She trusted me and considerably relieved the pain of such a repetitive task after I understood the concept. Thank you, papa and mama!

I am really thankful to my brother who advised me to take physics at the university. This degree opened a huge range of opportunities and brought me close to wonderful people. At the University of Valencia, I really enjoyed playing smart with my colleagues and friends. We believed that we could meaningfully talk about philosophy, mathematical physics, politics, and sociology. Thanks, [redacted] as well as [redacted] for forcing me to still keep a foot on Earth. I also want to heartily thank [redacted] for her support and patience given my underdeveloped social skills and stubbornness in physics at that time.

The physics quest continued in Mainz where I came for an internship after finishing my physics degree. Thanks, [redacted] for introducing me to experimental atomic physics. You are a great mentor. Lab work was a great discovery and lots of fun! During a causal lunch, [redacted] announced to [redacted]: "Hey [redacted], do you know that Hector is going to Ulm for a master?". To what he answered: "What? Why not with us?". Since then, I am part of the Budker group. I want to thank [redacted] for convincing me to stay in the group, for enabling such a great Ph.D. program full of experiences and learning not only academically but also personally, and for introducing me to such a great community of international researchers.

Both the GNOME collaboration and the Budker group in Mainz were starting when I joined. I am grateful for this. I was able to really contribute and take part in the development of these great groups of scientists. I want to thank the members of the GNOME collaboration, [redacted] and [redacted]. Their advice helped me to move forward even in the darkest periods of this research. I want to especially thank [redacted], who was my companion for the largest part of this work. His very sharp analytical thinking always brought our research forward. I want to thank [redacted]. He walked with me through the first steps as a researcher. He is my reference point in the Budker group and he is always there to discuss and help with any of my concerns both academically and personally. Very warm thanks to [redacted]. His enthusiasm, vision, leadership, and approach to life and science are exemplary. I also want to thank [redacted] for being one of the most admirable and clever people I ever worked with.

Again, I want to thank [redacted] for encouraging me to travel to Berkeley. All three times that I have visited, I had life-changing experiences. I want to thank [redacted] for making me feel at home on this foreign continent.

I am really thankful to happen to land in the Budker group. It is a very colorful mixture of very interesting people with all traits of personality. Everyone left an influence on who I am now. My thanks to [redacted] ...

Even if my friendship and work relationship with [redacted] started relatively late, it allowed enough time for countless fruitful physics discussions in which his extremely deep understanding was always enlightening. I want to thank [redacted] for his friendship and energy to start new enterprises in the group as well as his priceless moral support. Thank you [redacted] for always managing to give me the best words of support when my moral was failing. Thanks, [redacted] for the adventures and scientific exchange that we had together.

All this time was not only filled with physics, programming, papers, and meetings. I also had the joy of starting a family. Thanks, [redacted] for keeping me sane and happy.

CONTENTS

I Appendix

LIST OF FIGURES

LIST OF TABLES

Table 1: List of acronyms.

Acronyms	Description
ALPs	Axion-Like Particles
AOM	Acusto-optical modulator
CMB	Cosmic Microwave Background
DAQ	Data Acquisition System
ECDL	External-Cavity Diode Laser
ECI frame	Earth-Centered Inertial frame
EDM	Electric dipole moment
GNOME	Global Network of Optical Magnetometers for Exotic physics searches
GPS	Global Positoning System
HDF5	Hierarchical Data Format version five
LIA	Lock-In Amplifier
NASDUCK	Noble and Alkali Spin Detectors for Ultralight Coherent darK matter
NMOR	Non-linear Magneto-Optical Rotation
PID controller	proportional-integral-derivative controller
PPS	Pulse-Per-Second
QCD	Quantum Chromodynamics
SAS	Saturated Absorption Spectroscopy
SERF	Spin-Exchange Relaxation Free
SHM	Standard Halo Model
SM	Standard Model
SNO	Sudbury Neutrino Observatory
SUSY	Super-Symmetric theories
UBDM	Ultralight Bosonic Dark Matter
VCO	Voltage controlled oscillator
WIMPS	Weakly Interactive Massive Particle
ZULF	Zero-to-Ultralow field

1

INTRODUCTION

The Global Network of Optical Magnetometers for Exotic physics searches (GNOME) is an international collaboration consisting of several scientific groups and institutions around the world. The network is composed of a time-synchronized and globally distributed array of optical atomic magnetometers. The aim of the collaboration is the construction of such Earth size observatory and the search for evidence of beyond-the-standard-model spin dependent interactions. Generally, each of the groups contributes with a working optical magnetometer as well as data analysis procedures, sensor improvements, and theoretical framework.

GNOME has been possible thanks to the recent developments on optical magnetometry, and motivated by the pressing mystery about the composition of dark matter. Optical magnetometers can achieve $1\,\mathrm{fT}/\sqrt{\mathrm{Hz}}$ sensitivities, meaning changes in the millihertz range in the Larmor frequency. This makes them suitable for probing exotic spin-dependent interactions.

Decades of search for the constituents of dark matter highlight the fact that new and original experimental ideas are needed to shed some light on this problem. GNOME constitutes a global observatory for any exotic interaction with fermion spins. Its network configuration makes it specially suitable to search for scenarios in which transient signals or global patterns are expected. Different dark matter models could be tested by this new way of observing the universe [1] (domain walls [2, 3], boson stars [4], oscillations and stochastic fluctuations of a background field [5, 6], blobs of weakly interacting matter trapped inside Earth [7, 8]).

The main focus of this thesis is the development and application of a data analysis procedure to search the GNOME data for axion-like particle (ALP) topological defects, namely ALP domain walls, being the principal component of dark matter [2]. The ALP field can present different configurations which minimize its energy. During the evolution, expansion and cooling of the universe, the field can acquire distinct energy minima at different locations. Such regions are called domains. Domain walls form in the boundary between domains where the field value monotonically changes to link the two field values. Therefore, within a domain wall the energy of the field does not correspond to its minimum. Since such structures store energy, they could account for the dark matter. The formation of domains walls is a general property of the ALP field because its Lagrangian features a periodic potential [9].

The ALP properties depend on three independent parameters the mass m_a, the symmetry breaking scale f_{SB}, and the interaction scale f_{int}. The symmetry breaking scale is the energy scale at which a global U(1) symmetry is broken and the ALP establishes as a pseudo-

Nambu-Goldstone boson. In the domain wall model such energy scale influences, for example, the size of the domains. The interaction scale governs the coupling strength with standard model particles and differs for each of the fundamental particles in the Standard Model. The mass quantifies the rest energy of the particle.

Typically, searches for light dark matter aim for the QCD axion [10] whose generalization are the already mentioned axion-like particles. The QCD axion was proposed to solve the strong-CP problem in the Standard model Lagrangian [11]. A term in this Lagrangian allows the strong force to violate the charge-party discrete symmetries. However, experimental evidence strongly constraints such possibility [12]. The QCD axion offers an explanation for the CP-violating term being negligible. In addition, if it exists, the QCD axion could account for the dark matter [13]. In the particular case of the QCD axion models, symmetry breaking scale and the interaction scale are proportional [14]. For this reason, even if the QCD axion can form domain walls, they are excluded by observations because they will store to much energy [15]. In contrast, GNOME, since it deals with ALPS, it allows symmetry breaking scale and interaction scale to be independent. This allows a parameter space in which the walls store less energy and evade observations. Note that ALPs have similar properties to the QCD axion but do not solve the strong-CP problem.

Three different possible interactions couple ordinary matter and ALPs [16]. The most popular for direct detection is the coupling with photons. Experiments like ADMX [17] and HAYSTAC [18] use microwave cavities to observe the conversion of axions to photons in a magnetic field.

The coupling to gluons induces oscillating electric dipole moments in different nucleons, atoms and molecules. Measurements on the EDM of neutron and nuclear magnetic resonance experiments have already constrained this coupling [19, 20].

Finally, the fermionic interaction couples the ALP with the axial-vector current of nucleons. The strength of the coupling is typically parameterized as $g_{aNN} = 1/f_{int}$ [2, 21], where N can designate protons or neutrons. Consequently, f_{int} varies for each nucleon. For protons, the ratio between symmetry breaking and interaction scales for the QCD axion model is given by $f_{SB}/f_{int} = c_{ap}$, where c_{ap} is a model dependent dimensionless constant. The most accepted QCD axion models, the so called Kim-Shifman-Vainshtein-Zakharov (KSVZ) and Dine-Fischler-Srednicki- Zhitnitsky (DFSZ) models, predict a value between -0.6 and -0.2 [14]. Because of the sensors used, GNOME focuses on the couple to protons.

The fermionic interaction allows accelerated nucleons to emit ALPs. This effect can be used to search for ALPs by observing cooling rates of supernova [22] and neutron stars [23]. Axions can also be emitted during nuclear transitions. Such reactions can happen inside the Sun and their rate can be measured by observing associated neutrinos. On Earth, the axions can be captured and measured via deuterium dissociation. A model independent search can be derived from these effects since the production and detection mechanisms are well determined [24].

A spin dependent force between nucleons is predicted by the ALP fermionic interaction [25]. Such forces can be of the form of monopole-dipole or dipole-dipole interaction [26]. Different experiments search for such exotic couplings [27–29]. The strength of this forces depend on the product of the coupling constants corresponding to the two interacting bodies $g_q^N g_q^N$, where N is a fermion and q indicates whether it is a monopole or dipole interaction. Forces solely dependent on the proton coupling were constrained by studying the rotational states of hydrogen molecules [30]. More recent results reported in Ref. [31] constraining the coupling to neutrons could also be used to constrain the proton coupling [32]. A polarized ^{3}He sample exerts a dipole-dipole force on the ^{3}He spins within the co-magnetometer cell. Since the total spin of ^{3}He contains a known contribution from the proton spin (-2.7%), the proton coupling can also be constrained to $g_{app} \gtrsim 4 \times 10^{-4}$ in range of masses from 0 to 10^{-6} eV.

If ALPs are the dominant component of dark matter, the virialized particles produce a field oscillating close to their Compton frequency. This background field would be present in the vicinity of Earth. Under the fermionic interaction the gradient of this field couples with spins similarly to a magnetic field. Such a coupling is being investigated by magnetic resonance experiments like CASPEr [33, 34] and NASDUCK SERF [35]. These are classified as dark matter haloscopes because they rely on the galactic dark matter halo. For negligible self-interactions, the ALPs will interfere because the relativistic Doppler effect produces slight shifts on their oscillation frequency . This results on stochastic fluctuations in the amplitude of the field [5]. In case of the fermionic interaction being proportional to the gradient of the square of the field, the stochastic fluctuations in the amplitude produce a near-zero frequency component in the interaction [6]. This is an interesting idea because one can search for this near-zero frequency component for a large range of masses without changing experimental parameters.

The search for domain walls also relies on the ALP field being a dominant component of dark matter. However, the energy density is not stored in the field oscillations but in the potential energy raised by the domain walls. The fermionic interaction couples the gradient of the domain wall with spins. If Earth traverses a domain wall, this transient event would produce a distinctive pattern of signals in the GNOME network.

The results of the domain wall search have been published in two articles. Reference [36] describes the analysis procedure and Ref. [3] presents the results of the search in the data-set spanning between the 29th of November to the 22nd of December 2017. The analysis was conceived and implemented in close team work with [redacted] as well as with advice and help from [redacted] [redacted] and the whole GNOME collaboration through weekly meetings. The development of the algorithm was a long learning process where the people involved had no previous experience with complex data analysis procedures.

Our search did not find any statistically signals above background during the considered measuring time that could point to the existence of ALP domain walls. The excluded region of ALP parameter space is defined by the ALP parameters expected to form domain walls that would cross the earth at least once during the measuring time with 90% confidence level.

One can compare the constraints to the proton coupling accomplished by GNOME [3] with the experiments sensitive to the proton coupling mentioned earlier. A distinction has to be made between the dark matter dependent experiments since their cosmological assumptions greatly differ. GNOME relies on the topological properties of the field with the formation of domain walls. This is shown in Fig. 1.1b. This representation is constrained to $f_{\mathrm{SB}}/f_{\mathrm{int}} = 0.6$ which is the expected value for the QCD axion [14]. A peculiarity of the GNOME search is that the domain wall constraints depend on both f_{SB} and f_{int} while the others are sensitive to f_{int} alone. In contrast to GNOME, CASPEr and NASDUCK assume the typical cosmological model in which domain walls do not survive until today and the ALP field continuously oscillate close to their Compton frequency. Their constraints are shown in Fig. 1.1a. Both plots show the dark matter independent constraints in color.

The GNOME result explores ALP parameter space up to $g_{\mathrm{app}} \sim 10^{-4}\,\mathrm{GeV}^{-1}$. This partially covers the gap between constraints extracted from measurements of molecular hydrogen [30] and the Sudbury Neutrino Observatory (SNO) [24]. However, it cannot surpass the astrophysical observations that suggest that $f_{\mathrm{int}} \gtrsim \times 10^{-9}\,\mathrm{GeV}$. Even if in a different cosmological scenario, GNOME's bounds are comparable to the ones of CASPEr. Note that domain wall search from GNOME is not sensitive to the conventional scenario in which the dark matter field oscillates at the Compton frequency.

The idea of a search based on the coherence properties of the stochastic fluctuations of an ALP field background was explored in Ref. [6]. This publication studies the expected features and sensitivities of GNOME and atomic clock networks to the spatial coherence of the field. In that case, GNOME would be sensitive to the conventional scenario in which the dark matter field oscillates at the Compton frequency. This work was realized in team with [redacted], [redacted] and other GNOME and CASPEr collaboration members.

In addition to the data analysis, I was in charge of the maintenance of the optical magnetometer situated in Mainz which I constructed during my Master thesis. Additionally, I was partially responsible for the magnetometers located in Berkeley. I visited Berkeley in three occasions to perform upgrades and maintenance work. The detailed configuration of GNOME was published in Ref. [38] describing all the magnetometers conforming the network in 2018. Even though some groups joined since then, it is still a good snapshot of the status of the network.

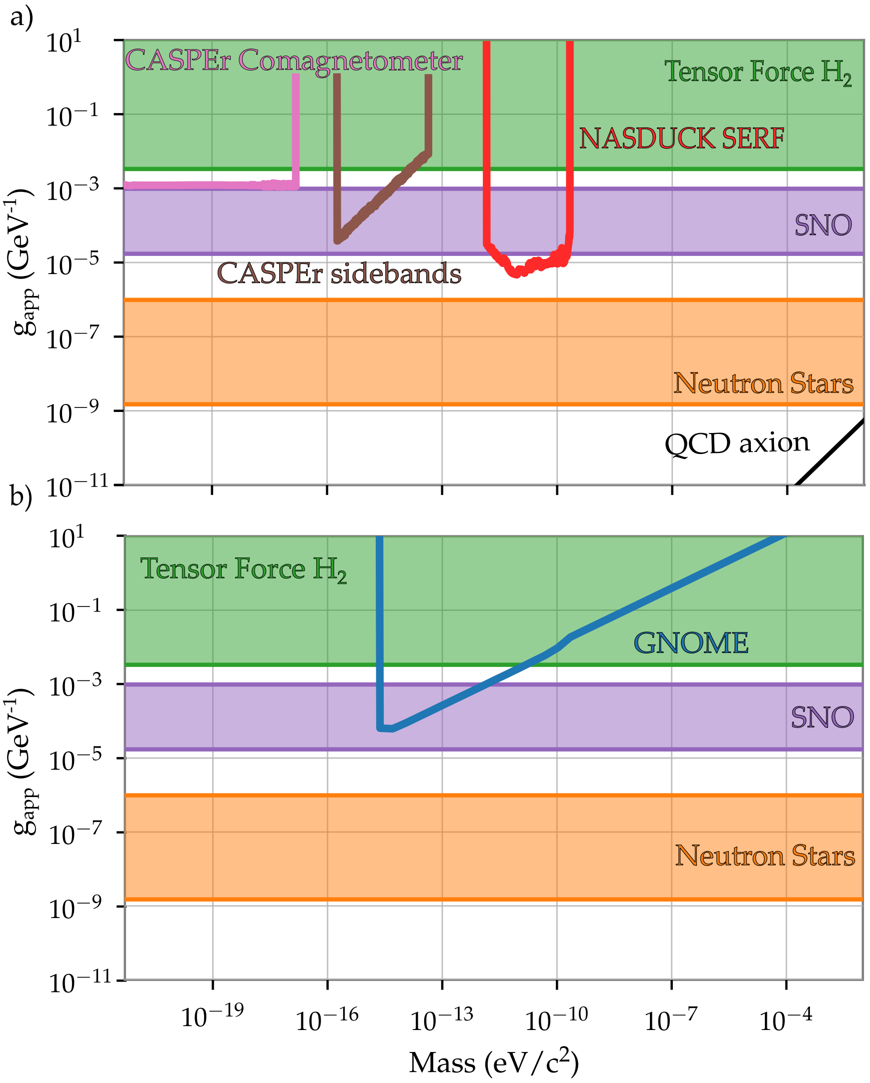

Figure 1.1: Experimental constraints on ALP-proton coupling. The colored areas show excluded regions by dark matter independent measurements. These are; ALP mediated forces: tensor force [30]; astrophysical constraints: SNO [24] and neutron stars [23]. a) Shows dark matter haloscopes which assume an uniformly distributed ALP field: CASPEr-ZULF comagnetometer [33], CASPEr-ZULF sidebands [34], NASDUCK [35] b) Shows a dark matter haloscope which assumes the formation of topological defects; GNOME [3]. Note that this GNOME constraint assume $f_{SB}/f_{int} = 0.6$. The area excluded by the dark matter haloscopes is above the drawn curves. The prediction of the QCD axion is marked in black. Adapted from Ref. [37]

2

DARK MATTER

Cosmological observations such as: abundance of light atoms, large-scale structure distribution of galaxies, the cosmic microwave background (CDM), and the accelerated expansion of the universe can be accounted for by the ΛCDM model. In this model the universe started at a point-like event in hot and dense state (the Big Bang) which expanded over time. In order to explain the observations, the model needs two additional sources of energy density in addition to the Standard Model. These are dark energy, associated to the accelerated expansion of the universe and dark matter which contributes to the formation ordinary matter structures. Even if this model can fit the observations it does not provide an explanation for the nature of dark matter and dark energy. Therefore, despite the success of the Standard Model (SM) to explain the nature of fundamental interactions and particles in the universe, most of the matter content in the cosmos is still of unknown origin. From the total energy content of the universe, approximately, 68.3% corresponds to dark energy, and 26.8% corresponds to dark matter. Ordinary matter, described by the SM, only contributes around 4.9%. The latest result for this estimation of the energy content in the universe comes from the Planck collaboration [39]. The fractional energy content is obtained by fitting the ΛCDM model to the temperature distribution of the cosmic microwave background (CMB). Dark energy and dark matter are not explained by the SM and are of completely unknown origin. Many theorists are devoted to incorporating this evidence into the Standard Model, and several experiments have been built over the last decades to search for these unknown constituents of the universe [21, 40, 41]. However, so far the mystery surrounding dark matter and dark energy remains unresolved. Many models are being developed to solve the dark matter problem that propose specific candidates and observable quantities to measure [16, 42]. Current theory and evidences for dark energy have still some debate within the community [43, 44].

Evidence for the existence of dark matter comes from its gravitational interactions. However, unraveling its nature likely requires observing non-gravitational interactions between dark matter and ordinary matter [45]. One of the leading hypotheses is that dark matter consists of ultralight bosons such as axions [13, 46, 47] or axion-like particles (ALPs) [48, 49]. Axions and ALPs arise from spontaneous symmetry breaking at an unknown energy scale f_{SB}, which, along with their mass m_a, determines many of their physical properties.

2.1 EVIDENCE FOR THE EXISTENCE OF DARK MATTER

Pieces of evidence for the existence of dark matter were first encountered in the 1930s with the observation of galaxy clusters [50]. However, it was not until 1970, that this problem was recognized by the scientific community. The evidence for dark matter that was popularized is the discrepancy in the rotational velocity of galaxies between the value predicted by the measured visible mass and the observed velocity [51]. Currently, this is regarded as one of the weakest attest for the existence of dark matter because alternative models like modified Newtonian dynamics can successfully solve this discrepancy [52].

Since 1930s stronger evidence for the existence of dark matter has been found [53]. This includes simulations of universe formation [54], the dynamics of the Bullet cluster [55, 56], images of gravitational lensing [57], and the anisotropy in the cosmic microwave background [58]. These are indirect evidence of a probably very weakly interacting particle which, until now, has escaped direct detection.

The most accurate account for the energy content in the universe is derived from the measurement of the anisotropies in the CMB. The early universe was hot and dense compared to the present times. Matter and radiation were strongly coupled through Compton scattering. As the universe expanded and cooled, atoms were formed and the primordial radiation was able to freely propagate. The universe continued expanding and this radiation is measured now at the microwave range. Anisotropies in the distribution of matter and radiation in the moment of recombination (first formation of atoms) at different scales can be measured in the power spectrum of the CMB. The anisotropies are originated by sound waves that were traveling through the early Universe. How the sound waves propagated can be studied by quantifying the strength of the temperature fluctuations at different angular scales in the sky, see Fig. 2.1. This provides valuable information about the constituents of the early universe, such as the relative abundances of ordinary matter, dark matter and dark energy. The relative amplitude between the second and third peaks provides an estimate for the amount of dark matter.

General Relativity predicts that mass curves space-time producing a lensing effect on light that passes nearby. Such effect was predicted by Einstein [59] in 1916 and experimentally observed by Dyson et al. [60] in 1920. During a total eclipse in which the Sun was situated in the line of sight of a rich cluster of stars their positions were recorded. Due to the gravitational potential of the Sun, a slight change in the positions was expected. The measured deviation agreed with the predicted value calculated by Einstein some years earlier. Such experiment not only successfully confirmed General Relativity but pioneered a new tool to observe the universe called gravitational lensing. Remarkably the potential of this technique was not foreseen at the time of its discovery [61]. Observing the interaction of gravity with light allows to infer the presence of invisible matter along the line of sight of background objects. This is not only interesting for the study of dark matter but also for the search of exoplanets [62] or massive astrophysical compact halo object (MACHOS) [63].

Gravitational lensing offers a direct observation of the invisible mass that we call dark matter. It can be used to characterize the distribution of such mass at cosmological scales [64], galaxy clusters [65]

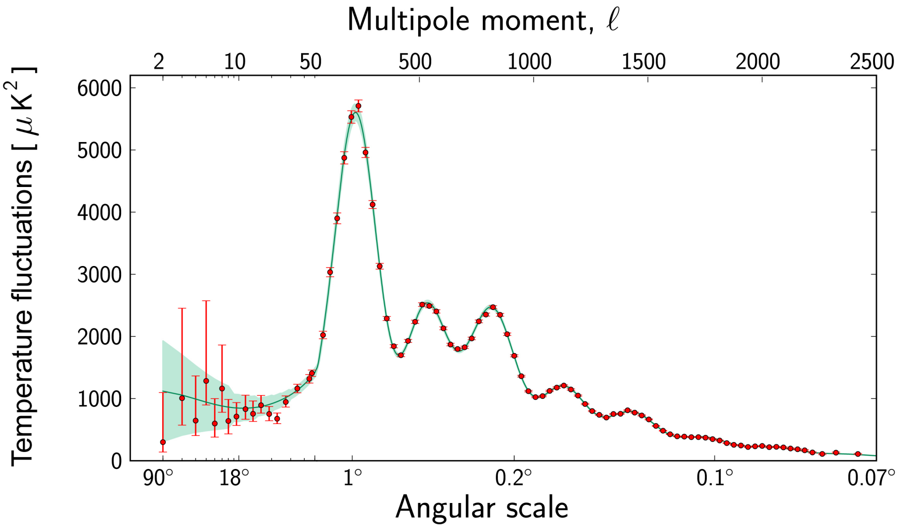

Figure 2.1: Temperature fluctuations in the Cosmic Microwave Background measured by Planck at different angular scales on the sky [58]. The peaks indicate the characteristic angular scale at which anisotropies appear. The relative amplitude of the peaks is governed by the relative content of barionic matter, dark matter and dark energy. The green line shows the best fit to the ΛCDM model. The image is extracted from `https://www.esa.int/`.

and galaxies [66]. It turns out that the mass within these structures is not dominated by the luminous matter but by dark matter. An astonishing reconstruction of the mass in a galaxy cluster can be seen in Fig. 2.2 extracted from Ref. [67]. Dark matter permeates the space between galaxies which are seen as sharp peaks.

2.2 DARK MATTER CANDIDATES

The strong evidences for the existence of dark matter but the lack of non-gravitational observations have forced theoretical physicist to postulate increasingly exotic theories [41]. The most popular explanations are based on adding new particles to the Standard Model. From those, the most prominent are the weakly interactive massive particles (WIMPS) and the axions.

WIMPS are the most studied candidate so far. The predicted mass for WIMPS ranges from $10\,\mathrm{GeV/c^2}$ to $1\,\mathrm{TeV/c^2}$ and they only interact with ordinary matter through the W and Z bosons (the weak interaction). Such particles could be derived from super-symmetric theories (SUSY) introduced to solve problems in the SM and are not directly related to dark matter. Remarkably, such particles could be suitable as dark matter candidates. Some variants of SUSY predict that all super-symmetric particles must decay into other super-symmetric particles. Under this assumption, the lightest SUSY particle cannot decay into anything else and remains stable, just like dark matter is expected to be. The strongest candidate for the end of the decay chain is called a neutralino which is predicted to have a large mass ($> 300\,\mathrm{GeV/c^2}$) and interacts very weakly with ordinary matter [68].

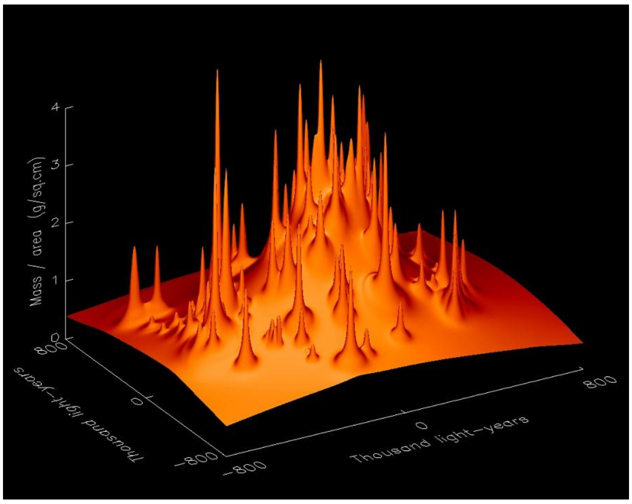

Figure 2.2: Reconstructed mass of the galaxy cluster CL0024+1654 using gravitational lensing . Most of the mass is spread in the intergalactic space between the galaxies. In contrast, the galaxies are shown as sharp peaks in the mass distribution. The image is extracted from Ref. [67].

This theoretical framework even if elegant and suitable, has been largely excluded by experiments like XENON [69–71].

An emerging dark-matter candidate in the light-mass regime is the axion. The three fundamental symmetries in the SM are charge conjugation (C), parity (P) and time reversal (T). If all three parameters are flipped the same physics is obtained. However, these symmetries can be violated individually or in pairs. For example, the weak force violates P and CP. Given a phenomenon mediated by the weak force, the result changes when the spatial coordinates are reversed. Similarly, the portion of the SM Lagrangian describing the strong force interactions contains a charge-parity(CP) violating term,

$$\mathcal{L}_{\mathrm{SM}} = \ldots + \frac{\theta g^2}{32\pi^2} G^a_{\mu\nu} G^{a\mu\nu}, \tag{2.1}$$

here $G^a_{\mu\nu}$ represents the quantum chromodynamics (QCD) field strength and g is the QCD coupling constant which are preceded by the parameter θ. The parameter θ is an angle that can take values from $-\pi$ to π and weights the importance of the CP violating term [72]. Remarkably, a non-zero value of θ will produce a constant electric dipole moment (EDM) in electrons, neutrons and other quantum systems. Consequently, the search for neutron EDM constrained its value to $\theta < 2 \times 10^{-10}$ [12, 73]. Therefore, in order to agree with observations θ must be very close to zero. This is referred to in the literature as the *strong CP problem* because there is no reason in the theory to prefer small over large values.

2.3 AXIONS AND AXION-LIKE PARTICLES

In 1977 Roberto Peccei and Helen Quinn found an elegant solution for θ taking a very small value. They introduced a new symmetry into the theory, promoting θ to a field. In the early universe θ has no preferred value because of the high temperature. However, as times goes by, and the universe cools down, the strong force begins to be relevant, hadrons start to form and θ prefers small values since they minimize the vacuum energy. Due to the shape of the potential of θ, Steven Weinberg and Frank Wilczek realized that this solution implies the existence of a new pseudoscalar[1] particle which was called the axion because it was thought to erase all the problems of the standard model like the popular soap brand does with grease stains [74–76].

The properties of the axion solely depend on the symmetry breaking scale f_{SB} that indicates the energy at which the symmetry of the field is broken and field oscillations can appear as axions with a mass. The symmetry breaking scale was first thought to be similar to the electroweak scale but that hypothesis was quickly discarded by experiments. Later on, theories allowing much higher f_{SB} values were developed. The larger the f_{SB}, the lighter the axions and the weaker the interaction. Nonetheless, this is beneficial because the lower the mass of the particle, the higher the abundance in the cosmos. Several production mechanism for axions in the early universe exist. The most popular is the so-called misalignment mechanism. In the early universe the energy is high enough so that the axion is massless and the field does not have a preferred value. When the universe cools down the axion acquires mass and starts feeling a potential at a random field value. Such potential has a minimum at the CP-conserving value of the field. The dynamics of the axion field rolling from the randomly acquired value to the minimum result in oscillations. Such oscillations produce the particles and their cosmological energy density grows as $f_{SB}^{7/6}$ [77]. For this reason this lighter axions emerged as a suitable candidate for DM. This is the so-called quantum QCD-axion.

Currently, the axion is waking great experimental interest. On the one hand, the stringent constraints on the WIMP parameter space eroded theories predicting it. On the other hand, the low-mass nature of axions allow the use of atomic-physics experiments. These are well-known for reaching great sensitivities and being relatively easy to implement in comparison to particle colliders or astronomical observatories. Additionally, axions can have a variety of sources, they can be produced in the lab, in the sun, in supernovae or be a constituent of dark matter. A plethora of experiments are being planned or are already searching this particle using cutting-edge experimental techniques. Constraints are being placed on the axion coupling to photons and nucleons. A review of the experimental landscape and brief summary of the axion physics can be seen in Refs. [21, 78].

As discussed above, the properties of the axion depend only on one parameter: the symmetry-breaking scale which governs the mass and the coupling to SM particles. However, when evaluating the experimental constraints on such particles, mass and coupling strength are allowed to freely vary creating a two dimensional parameter space.

---

[1] This refers to a quantity that behaves like a scalar but it is not invariant under parity transformations.

The symmetry-breaking scale and coupling strength have a fixed relationship. However, this condition can be also relaxed leaving the particle to be described by three independent quantities. This last scenario even if incompatible with the QCD-axion can be endorsed by generalized theories and are referred to as axion-like particles (ALPs). When one considers beyond-the-SM theories for explaining the universe, such as string theory or SUSY, a whole range of ALPs appear [79]. These particles have similar properties as the QCD axion but they are not a solution the strong-CP problem.

Additionally, ALPs can form stable, macroscopic field configurations in the form of topological defects [2, 15, 80–84] or composite objects bound together by self-interactions such as boson stars [4, 85, 86] or Q-balls [87, 88]. Similarly to magnetic moments in ferromagnetic materials the ALP field can acquire different values as it cools down and form sharp boundaries between regions. The boundaries could concentrate the dark matter energy density into compact spatial regions that are small compared to the galaxy but much larger than the Earth [2, 15, 82, 84]. Earth-bound detectors could be used to sense the passage of Earth through such objects. A wide range of parameter space for such dark-matter objects, consistent with observations, can have the required size and abundance such that the characteristic time between encounters could be on the order of one year or less [2, 4, 83]. This opens up the possibility of searching for ALP domain walls with terrestrial detectors. While some models suggest that ALP domain walls cannot survive to the present epoch [89] — particularly those involving the QCD-axion [13, 46, 47] — there do exist a number of non-trivial ALP models demonstrating the theoretical possibility that ALP domain walls can survive to modern times [90–92] and have the characteristics of cold dark matter [2, 83, 93, 94].

ALPs do not necessary form topological defects that boost the detection strength of GNOME. Therefore, other hypothesized properties should be exploited to enhance the expected signal. Generally, the ALP field oscillates at the Compton frequency, $\omega_c = m_a c^2/\hbar$. Where m_a is the mass of the ALP, c is the speed of light and $\hbar$ the reduced Plank constant. If an interaction with SM particles is quadratic on the field i.e. $\propto$ *intensity*, part of the signal is down-converted to near-zero frequency, regardless of the particular Compton frequency. Furthermore, assuming the standard halo model (SHM) the bosons are virialized in the galaxy. This dynamics produce slight changes on the Compton frequency of the individual bosons resulting in stochastic fluctuations of this near-dc component [95, 96]. The spectral width of this near-dc feature in frequency space is $\approx 10^6$ times smaller than ω_c, allowing sensors with limited bandwidth to be sensitive to masses 10^6 times larger than if the sensors were used to search for direct field-oscillations at ω_c.

This thesis focuses on the search for ALP domain walls using GNOME data. Additionally, it discusses the expected sensitivity of GNOME to features produced by stochastic fluctuating ALP field on the GNOME network.

3

OPTICAL ATOMIC MAGNETOMETRY

Optical atomic magnetometry is a collection of techniques to measure magnetic field using atomic spins which features great precision. It was first realized by Bell and Bloom in 1957 [97]. Since then the technology has greatly improved and matured. Compact atomic magnetometers are already commercialized by companies like Twinleaf LLC and Quspin Inc.. Optical magnetometry features a large range of uses from medicine [98] and biology [99, 100] to fundamental physics [3, 12, 34] as well as various technological applications [101, 102].

These techniques are based on the accurate determination of the Zeeman energy splitting in atoms or nuclear spins. Generally, a laser beam is used to optically pump the atomic populations into a magnetically sensitive state. An additional (or the same) laser beam is used to determine the magnetic field by observing the dynamics of the atomic populations through polarization rotation or intensity modulation. Some magnetometer realizations include additional fields or light intensity modulation to excite the Zeeman levels.

Classically, a magnetic moment in a magnetic field experiences a torque given by,

$$\mathfrak{T} = \boldsymbol{\mu} \times \boldsymbol{B}, \tag{3.1}$$

where $\mathfrak{T}$ represents the torque, $\boldsymbol{\mu}$ the magnetic moment and $\boldsymbol{B}$ the magnetic field. In turn, if the magnetic field is low enough to not perturb the atomic structure, the magnetic moment of an atom is proportional to the total angular momentum $\boldsymbol{\mu} = \gamma \boldsymbol{J}$, where γ is the gyro-magnetic ratio. The solution of the Eq. (3.1) results in an oscillation at a frequency only proportional to the magnetic field magnitude and independent of the relative angle between $\boldsymbol{\mu}$ and $\boldsymbol{B}$, provided that the angle is larger than zero, given by

$$f_{\mathrm{Larmor}} = \frac{\gamma B}{2\pi}. \tag{3.2}$$

The quantum mechanical description of this precession can be seen as the atomic populations moving through the ground-state Zeeman levels at a rate given by the Larmor frequency. The movement of populations changes the absorptive and refractive properties of the atomic vapor. Therefore, the Larmor frequency can be precisely measured by probing these changes with laser light.

A plethora of realizations of optical atomic magnetometers exist in the literature. In this chapter, I will just introduce the basic working principles of optical magnetometers.

3.1 ENERGY LEVELS IN ALKALI ATOMS

Alkali atoms are often used in atomic magnetometry because their quantum states can be easily manipulated by optical means. All electrons lie in closed shells except for a single valence electron in the outermost layer. This results in a simple energy-level structure similar to that of hydrogen.

The accurate determination of the energy states of alkali atoms is complicated and out of the scope of this thesis. However, a qualitative argument for the energy-level structure can be given. The conserved quantities in an isolated atom are known and an alkali atom system can be simplified by considering a single electron orbiting a fixed core (inner electrons and nucleus).

In order to describe the energy-level structure, one should find operators that commute with the Hamiltonian and therefore can be determined simultaneously with the energy. Since an atom features a central potential, the total atomic angular momentum $\hat{\boldsymbol{F}}$ is conserved. This is the sum of the total electron angular momentum $\hat{\boldsymbol{J}}$ and the nuclear spin $\hat{\boldsymbol{I}}$, $\hat{\boldsymbol{F}} = \hat{\boldsymbol{J}} + \hat{\boldsymbol{I}}$. In turn, the total electron angular momentum $\hat{\boldsymbol{J}}$ is the sum of the electron spin $\hat{\boldsymbol{S}}_e$ and the electron orbital angular momentum $\hat{\boldsymbol{L}}$, $\hat{\boldsymbol{J}} = \hat{\boldsymbol{S}}_e + \hat{\boldsymbol{L}}$. Since this operators act on independent Hilbert spaces, they commute with each other. However, only the magnitude square of the operators $\hat{\boldsymbol{F}}^2$, $\hat{\boldsymbol{J}}^2$, $\hat{\boldsymbol{S}}_e^2$, $\hat{\boldsymbol{L}}^2$, $\hat{\boldsymbol{I}}^2$ commute with the Hamiltonian due to the interaction among these angular momenta. Since $\hat{\boldsymbol{F}}$ is conserved, $\hat{\boldsymbol{F}}_z$ is also conserved and commutes with the magnitude square operators.

Since all these operators commute, we can find a common basis of eigenfunctions that characterizes the possible states of the system. The eigenfunctions are indexed in terms of quantum numbers. The quantum numbers are denoted by the same letter as the magnitude squared operators while m_z is used for $\hat{\boldsymbol{F}}_z$.

The eigenvalues for the magnitude squared of the angular momentum operators are given in terms of the quantum numbers by,

$$\hat{\boldsymbol{F}}^2|n, S_e, L, J, I, F, m_F\rangle = \hbar^2(F(F+1))|n, S_e, L, J, I, F, m_F\rangle. \tag{3.3}$$

The eigenvalues of $\hat{\boldsymbol{F}}_z$ are given by,

$$\hat{\boldsymbol{F}}_z|n, S_e, L, J, I, F, m_F\rangle = \hbar m_F|n, S_e, L, J, I, F, m_F\rangle. \tag{3.4}$$

The energy could depend on all quantum numbers, however, since the magnitude of $\hat{\boldsymbol{S}}_e$ and $\hat{\boldsymbol{I}}$ can only take one value, and the properties of the atom are independent of the orientation is space (in absence of external fields), the energy only depends on the principal quantum number n, L, J and F. Therefore, we can write the eigenvalues of the Hamiltonian as,

$$\hat{\mathcal{H}}|n, S_e, L, J, I, F, m_F\rangle = E_{nLJF}|n, L, S_e, L, J, I, F, m_F\rangle. \tag{3.5}$$

Simple rules describe the possible combinations of quantum numbers. These are given in any introductory quantum mechanics book, for example Ref. [103]. Here, we focus on the ground and first excited states of alkali atoms.

The term-symbol notation is a standard to label the different energy levels of atoms, E_{nLJF}. The ground state electronic configuration of the outermost electron in an alkali atom is written as

$$^{2}S_{1/2}, \tag{3.6}$$

where the following notation is used $^{2S+1}L_J$. The electron orbital angular momentum follows special notation for historical reasons $L = 0, 1, 2, 3$ are indicated by the letters S, P, D, F. The spin multiplicity is given by $2S + 1$, where S is the total electronic spin quantum number. In the case of an alkali atom, it is $S = S_e = 1/2$. The spin multiplicity represents the number of possible values of the total angular momentum quantum number, J. It can take values between

$$|L - S| \leqslant J \leqslant L + S \tag{3.7}$$

in intervals of unity. In the ground state of alkali atoms, the orbital momentum quantum number $L = 0$ and the electron spin quantum number $S = 1/2$. Therefore the total electron angular momentum can just be $J = 1/2$. Note that if $L < S$, the maximum number of possible J is $2L + 1$.

In the same way one can consider the first excited electronic state of an alkali atom. In that case $L = 1$ then the total electron angular momentum quantum number can take two values $J = 1/2$ and $J = 3/2$. This gives rise to the two excited energy levels $^{2}P_{1/2}$ and $^{2}P_{3/2}$.

The term symbol notation just considers S, L and J. However, further electronic configurations are possible when considering the nuclear spin. Similarly to the total electron angular momentum quantum number J, the atomic spin quantum number, F can take values ranging between

$$|J - I| \leqslant F \leqslant J + I. \tag{3.8}$$

Each of this configurations possess different energies and therefore an alkali atom features the energy diagram shown in Fig. 3.1.

The orbital structure splitting is produced by the valence electron interacting with the inner shells. The fine structure splitting is produced by interaction between the $\hat{\boldsymbol{S}}_e$ and $\hat{\boldsymbol{L}}$. The hyperfine structure splitting is produced by the interaction between $\hat{\boldsymbol{J}}$ and $\hat{\boldsymbol{I}}$. Note the hierarchy between the energy splittings. The fine structure splitting is weighted by a factor α^2 with respect to the binding energy, where α is the fine structure constant. While the hyperfine splitting is weighted by $\alpha^2(m_e/m_N)$ where m_e is the mass of the electron and m_N is the mass of the nucleon.

3.1.1 *Zeeman effect*

An external magnetic field interacts with an atom lifting the degeneracy on the m_F states. The interaction of a magnetic field $\boldsymbol{B}$ with an atom can be described by the Hamiltonian,

$$\hat{\mathcal{H}}_{\text{Zeeman}} = \hat{\mathcal{H}}_{\text{fs}} + \hat{\mathcal{H}}_{\text{hfs}} - \hat{\boldsymbol{\mu}} \cdot \boldsymbol{B}, \tag{3.9}$$

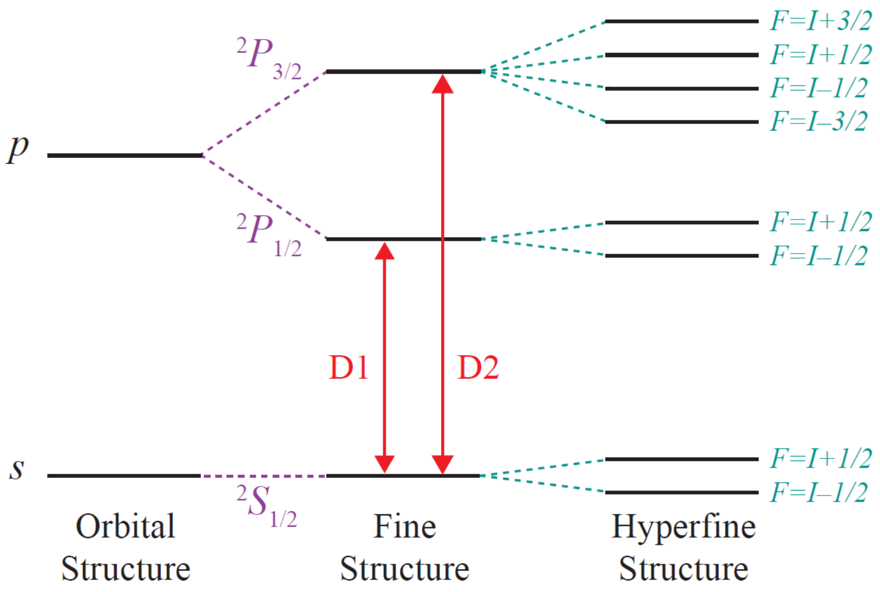

Figure 3.1: Energy-level structure of the ground state and the first excited state in an alkali atom. The energy splitting is not shown in scale. The designation of D1 and D2 are the historical names of the optical transitions shown. Image extracted from Ref. [104].

where $\hat{\mathcal{H}}_{\text{fs}}$ and $\hat{\mathcal{H}}_{\text{hfs}}$ are the fine and hyperfine splitting Hamiltonians. The first couples $\hat{\boldsymbol{S}}_e$ with $\hat{\boldsymbol{L}}$, and the second $\hat{\boldsymbol{J}}$ with $\hat{\boldsymbol{I}}$ [105]. For weak magnetic fields, the magnetic interaction, $\hat{\boldsymbol{\mu}} \cdot \boldsymbol{B}$, is similar in magnitude to $\hat{\mathcal{H}}_{\text{fs}}$ and $\hat{\mathcal{H}}_{\text{hfs}}$. Therefore the basis presented in Eq. (3.3) should still be adequate to describe the system. The atomic magnetic moment, $\hat{\boldsymbol{\mu}}$ can be written as a function of the different spin components as

$$\hat{\boldsymbol{\mu}} = -\frac{\mu_B}{\hbar}(g_S \hat{\boldsymbol{S}} + g_L \hat{\boldsymbol{L}} + \frac{\mu_N}{\mu_B} g_I \hat{\boldsymbol{I}}), \tag{3.10}$$

where $\mu_N = \mu_B(m_e/m_N)$ is the nuclear magneton, μ_B is the Bohr magneton [105]. The g-factors of electron, angular momentum and nucleus are given by $g_S \approx 2$, $g_L = 1$ and g_I respectively. Due to the fine and hyperfine interactions, only the projection of $\hat{\boldsymbol{F}}$, $\hat{F}_z$ is conserved. The expectation value of each terms in a sum of angular momentum is proportional to the expectation value of the sum. This is known as the projection theorem which is a special case of the Wigner-Eckart theorem [106]. This can be written as

$$\langle \hat{\boldsymbol{J}} \rangle = \frac{\langle \hat{\boldsymbol{J}} \cdot \hat{\boldsymbol{F}} \rangle}{\langle |\hat{\boldsymbol{J}}| \rangle} \langle \hat{\boldsymbol{F}} \rangle. \tag{3.11}$$

After some algebra, the expectation value of $\hat{\boldsymbol{\mu}}$ in the eigenbasis of the atom presented in Eq. (3.3) is given by

$$\langle \hat{\boldsymbol{\mu}} \rangle = \frac{g_F \mu_B}{\hbar} \langle \hat{\boldsymbol{F}} \rangle, \tag{3.12}$$

where the Landé factor for the hyperfine structure is given by

$$g_F = g_J \frac{F(F+1) + J(J+1) - I(I+1)}{2F(F+1)}, \tag{3.13}$$

and the Landé factor for the fine structure is given by

$$g_J = 1 + \frac{J(J+1) + S(S+1) - L(L+1)}{2J(J+1)}. \tag{3.14}$$

Note that the terms proportional to the ratio μ_N/μ_B have been neglected because this factor is around 1/2000.

From here it follows that the variation of energy produced by a magnetic field pointing along the z-axis is given by

$$E_{\text{Zeeman}} = g_F \mu_B m_F B_z, \tag{3.15}$$

and the splitting between two adjacent Zeeman levels is

$$\Delta E_{\text{Zeeman}} = g_F \mu_B B_z = \hbar\omega_L. \tag{3.16}$$

The energy splitting can be characterized by the Larmor frequency ω_L.

3.1.2 *Perturbation on nuclear spins*

Even if GNOME is a network of magnetometers, the main aim of the collaboration is not to measure magnetic fields but to search for beyond-the-SM pseudo-magnetic interactions. These can couple with protons, electrons and neutrons with an unknown coupling strength that differs from the known magnetic interaction. The magnetometers are placed in a magnetically shielded environment. The enclosure, made of highly permeable soft ferromagnetic material, cancels effects related to the electron spin couplings since they act like a magnetic field in the material. On the contrary, the shielding material responds weakly to nuclear couplings [107]. For this reasons, through this work it is assumed that the exotic pseudo-magnetic interactions solely couple to protons. Since magnetometers measure changes on the total atomic spin, the signal must be re-scaled to account for fact that the interaction just affects protons. Alkali atoms feature a single valence proton and therefore they are primary sensitive to the proton coupling.

Since alkali atoms feature a single valence proton, a reasonable estimate for the contribution of $\hat{\boldsymbol{S}}_p$ to $\hat{\boldsymbol{F}}$ can be obtained for K, Rb, and Cs. Assuming the Schmidt model [108] for the nuclear structure, $\hat{\boldsymbol{I}}$ is given by sum of the orbital spin and the intrinsic spin the valence proton $\hat{\boldsymbol{I}} = \hat{\boldsymbol{S}}_p + \hat{\boldsymbol{\ell}}$. Using the projection theorem, the expected value of the proton spin is proportional to the expected value of the total atomic angular momentum. Therefore, the expected value of the proton spin can be written as

$$\langle \hat{\boldsymbol{S}}_p \rangle = \frac{\langle \hat{\boldsymbol{S}}_p \cdot \hat{\boldsymbol{I}} \rangle}{I(I+1)} \frac{\langle \hat{\boldsymbol{I}} \cdot \hat{\boldsymbol{F}} \rangle}{F(F+1)} \langle \hat{\boldsymbol{F}} \rangle. \tag{3.17}$$

The fractional spin polarization of the nucleus relative to the spin polarization of the atom is

$$\sigma_{N,F} = \frac{\langle \hat{\boldsymbol{I}} \cdot \hat{\boldsymbol{F}} \rangle}{F(F+1)} = \frac{[(F(F+1) + I(I+1) + S_e(S_e+1))]}{2F(F+1))}. \tag{3.18}$$

The fractional spin polarization of proton spin relative to the nuclear spin is

$$\sigma_p = \frac{\langle \hat{\boldsymbol{S}}_p \cdot \hat{\boldsymbol{I}} \rangle}{I(I+1)} = \frac{[(S_p(S_p+1)+I(I+1)+\ell(\ell+1))]}{2I(I+1))}. \tag{3.19}$$

Finally the expected value of the proton spin polarization can be written in terms of the expected value of the total atomic angular momentum as

$$\langle \hat{\boldsymbol{S}}_p \rangle = \sigma_{p,F} \langle \hat{\boldsymbol{F}} \rangle, \tag{3.20}$$

where $\sigma_{p,F} = \sigma_p \sigma_{N,\,F}$.

The uncertainty on the contribution of the proton spins to the total atomic angular momentum can be estimated by comparing different models describing the nuclear spin structure of atoms. Other more sophisticated calculations are obtained from semi-empirical models [109, 110] and nuclear shell-models [111–113]. Comparing the estimations by the different models, we find that the accuracy of the Schmidt model is around 50% [32].

3.2 OPTICAL PUMPING

Optical pumping is a nonlinear process that changes the properties of an atomic sample by means of optical excitation. Using light with selected frequency, polarization, and intensity to interact with particular optical transitions, the atoms can be brought to a desired state. In magnetometry, this is used to polarize the atoms and produce a macroscopic magnetization along a given direction.

Under thermal equilibrium at temperature T, the distribution of an atomic ensemble in their different possible states is given by the Boltzmann distribution. For a two level system it can be written as

$$\frac{n_1}{n_2} = \exp\frac{(E_2 - E_1)}{kT}, \tag{3.21}$$

where n_i is the probability of the system being in state i, E_1 is the energy of that state, k is the Boltzmann's constant and T the thermodynamic temperature . The energy difference between the Zeeman sublevels is given by Eq. (3.16). A typical magnetic field value for the magnetometers is around $0.5\,\mu T$. Note that this is much smaller that Earth magnetic field $\approx 50\,\mu T$.

At such low magnetic fields at room temperature, the levels are equally populated. Therefore there is no macroscopic magnetization that could undertake Larmor precesion among a magnetic field. In order to reach a measurable macroscopic magnetization the energy difference must be much larger. Nuclear magnetic resonance set-ups typically operate at magnetic fields in the order of a Tesla or higher. The benefit of this is two fold. A large magnetic field increases the thermal nuclear polarization as seen in Eq. (3.21). Also, a high Larmor frequency can be more efficiently measured by coils. However, for a thermally polarized sample, the population difference between

Zeeman sublevels is still relativelly small, in the range of parts per million.

In many cases, one can alter the distribution of populations in the atomic ensemble much more efficiently by using optical excitation. In a cycle of absorption and emission of photons the total angular momentum is conserved. Resonant light can couple the ground and excited state of alkali atoms $^2S_{1/2} \rightarrow {}^2P_{1/2}$ or $^2P_{3/2}$. Additionally, the frequency accuracy and specificity (narrow linewidths) of lasers allows addressing a specific F state. When exciting the atoms with right (left) circularly polarized light, the absorbing atom is excited to a state $m_{F'} = m_F + 1\ (-1)$. Then the atom decays into the ground state $m_{F''} = m_{F'} + 1, 0, -1$. After some cycles, the population distribution is skewed towards positive (negative) m_F levels. This results in a macroscopic magnetization of the atomic sample.

3.3 SPIN RELAXATION

Mainly three mechanisms contribute to reduce the macroscopic polarization of the atomic ensemble. These mechanisms are: collisions with the cell walls, spin-exchange collisions and spin-destruction collisions, given in order of importance. These relaxation mechanisms are reviewed in Refs. [104, 114]

An alkali vapor gas at room temperature moves at ≈500 m/s which means that in a $5^3\,\text{cm}^3$ container the atoms will hit the wall at a rate $\approx 10^4\,\text{s}^{-1}$ [115]. When an atom hits the cell walls, it becomes adsorbed inside the surface and experiences the strong local electromagnetic fields in the glass. After a short time $\approx 10^{-5}$ to 10^{-7} s the atom is ejected with a completely random polarization [116]. The depolarization rate given by the collision rate is typically on the order of the Larmor frequency preventing the observation of the precession. Therefore, this effect can strongly limit the performance of optical atomic magnetomters.

Spin-exchange collisions preserve the total atomic angular momentum of the two colliding atoms $\hat{\boldsymbol{F}}_1 + \hat{\boldsymbol{F}}_2 = \hat{\boldsymbol{F}}_1' + \hat{\boldsymbol{F}}_2'$ [104, 114, 117]. As a result, the sum of the projections is also conserved $m_{F_1} + m_{F_2} = m_{F_1}' + m_{F_2}'$. However, the sum of the magnitudes is not conserved. This produces a redistribution of the populations among the ground state hyperfine sublevels. An example of such a collision is given in Fig. 3.2. Note that since the total atomic angular momentum is conserved, the populations are not redistributed if the sample is totally polarized in the $|2,2\rangle$ state. Spin-exchange collisions are specially detrimental for the performance for a magnetometer because the two hyperfine sublevels in an alkali atom precess in opposite directions. This prevents a coherent precession among the Zeeman sublevels. Spin-exchange collisions are specially relevant for high atomic densities.

Other type of collisions are the spin destruction collision. In this case the information about the polarization of the atoms before the collision is completely lost. Fortunately, the cross-section for such

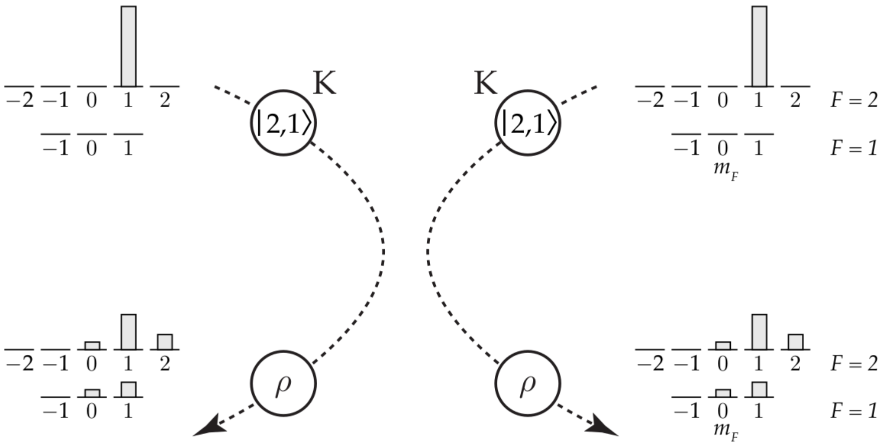

Figure 3.2: Illustration of the effect of spin-exchange collisions between alkali metal atoms. Such collision distribute the population between the F and m_F states. Extracted from Ref. [114].

collisions is typically four orders of magnitude smaller than spin exchange collisions [115].

3.3.1 *Reducing spin relaxation*

Reducing the spin relaxation mechanisms in the alkali vapor cell is an important factor when constructing a magnetometer. A relevant sensitivity limit for magnetometers is given by the fundamental quantum-mechanical uncertainty in the measurement of atomic spin projection. For a total number of atoms N and a spin relaxation rate Γ_{rel} this limit is given in magnetic field units by [118]

$$\delta B \approx \frac{1}{\gamma}\sqrt{\frac{\Gamma_{\text{rel}}}{N\tau}}, \tag{3.22}$$

where τ is the measuring time and γ is the gyro-magnetic ratio. Here, factors of order unity that depend on the particular setup are ignored.

From Eq. (3.22) it becomes apparent that the more atoms and the slower the spin-relaxation rate, the better the sensitivity. Bouncing into the glass cell walls completely randomizes the spin state of atoms and results in a high spin-relaxation rate. Mainly, two methods are commonly used to prevent wall depolarization: the use of anti-relaxation coating or the addition of a buffer gas. The walls of the alkali vapor cell can be coated with an inert material, typically a paraffin. This coating prevents direct interaction of the atom with the cell walls and allows many bouncing cycles without altering the spin state.

Despite intensive research on surface coating, it remains an artisan work that does not always yields reproducible results. High-quality coatings can allow more than 10^4 bounces before depolarization while one collision with the bare glass completely destroys the spin state. Therefore even if a small fraction of the surface has defects, this will ruin the performance of the coating.

Another technique to prevent wall depolarization is to hinder the free movement of the atoms by adding an additional gas into the cell. Due to the presence of this buffer gas, alkali atoms diffuse at much more slowly than their thermal (balistic) speed. Therefore they take much longer to reach the walls and depolarize. Typically, a noble gas like Xe or He is used since these are chemically inert. Spin-exchange collisions between an alkali and a noble gas atoms occur through the coupling between the alkali electronic spin and the nuclear spin of the noble gas. Therefore, they are negligible when the noble gas used has nuclear spin zero [119]. Even though collisions with the buffer gas increase the spin-destruction collision rate, it overall decreases spin relaxation (see Fig. 2.23 in Ref. [104]).

The next, by importance, spin relaxation mechanism is the spin-exchange collisions. By operating in the so called Spin-Exchange Relaxation Free (SERF) regime, the effects of these collisions can be avoided [118]. As seen in Fig. 3.2, the hyperfine ground-level population gets mixed by the collisions. The coherence in the precession is reduced because the two ground hyperfine states oscillate in opposite directions. However, if the collision rate is much higher than the Larmor frequency a coherent oscillation is recovered, but with at slower frequency. In this regime, an atom jumps several times between hyperfine ground states and Zeeman sublevels within a Larmor cycle. Since one of the hyperfine levels carries more statistical weight, the atoms will predominantly precess in one direction and the depolarization effects of spin-exchange collisions are greatly reduced. For an alkali atom with ground state hyperfine levels F=1 and F=2, the atoms will predominantly precess in the direction given by the F=2 level. The transition into the SERF regime is very well illustrated in Fig. 5.2 in Ref. [104].

3.4 ATOMIC POPULATION DYNAMICS

The interaction between an ensemble of alkali atoms and light can be described using the density matrix formalism and the Liouville equations. Such equations describe the time evolution of the atomic ensemble states under the action of a Hamiltonian. Moreover, this formalism allows the ad-hoc addition of effects not considered by the Hamiltonian such as relaxation. A similar analysis to the one presented in this section is given in Ref. [106].

The Hamiltonian of an atomic ensemble interacting with light in an external magnetic field can be written as

$$\hat{\mathcal{H}} = \hat{\mathcal{H}}_0 - \boldsymbol{\mathcal{E}} \cdot \hat{\boldsymbol{d}} - \hat{\boldsymbol{\mu}} \cdot \boldsymbol{B}. \tag{3.23}$$

The Hamiltonian of the unperturbed atom is given by $\hat{\mathcal{H}}_0$, the interaction of the atoms with the oscillating electric field of light is described by $-\boldsymbol{\mathcal{E}} \cdot \hat{\boldsymbol{d}}$, and the interaction of the atomic magnetic moment with an external magnetic field is given by $-\hat{\boldsymbol{\mu}} \cdot \boldsymbol{B}$. The symbols $\mathcal{E}$ and $\hat{\boldsymbol{d}}$ denote electric field from the laser beam and the electric dipole moment operator respectively.

The time evolution of the atomic populations is given by Liouville equation as

$$i\hbar\frac{d}{dt}\rho = [\hat{\mathcal{H}}, \rho] - i\hbar\frac{1}{2}(\hat{\Gamma}\rho + \rho\hat{\Gamma}) + i\hbar\Lambda. \tag{3.24}$$

Originally, the evolution of the density matrix, ρ, describing the atomic ensemble is given by the commutator with the Hamiltonian. Relaxation and repopulation mechanisms are not considered in that picture. Therefore, they are added ad-hoc by the matrices $\hat{\Gamma}$ and Λ. The rate $\hat{\Gamma}$ characterizes the relaxation of the atomic state due to complicated interactions not included in the Hamiltonian. Since the number of atoms in the system is conserved the relaxed atoms must appear again in an incoherent state. The rate Λ accounts for such repopulation mechanism. These matrices can be used to model the spin relaxation mechanisms described in Sec. 3.3, spontaneous emission or atom moving out of the light beam.

3.5 EFFECTS ON TRANSMITTED LIGHT

The dynamics of the atomic populations are observed through effects on the transmitted light. The electric field $\boldsymbol{\mathcal{E}}$ of a plane wave of frequency ω and wave-vector $\boldsymbol{k}$ can be written as

$$\begin{aligned}\boldsymbol{\mathcal{E}} = \mathrm{Re}\{\mathcal{E}_0 e^{i\boldsymbol{k}\boldsymbol{r}-\omega t+\phi}[(&\cos\alpha\cos\epsilon - i\sin\alpha\sin\epsilon)\hat{\boldsymbol{e}}_1 \\ &+(\sin\alpha\cos\epsilon - i\cos\alpha\sin\epsilon)\hat{\boldsymbol{e}}_2]]\}.\end{aligned} \tag{3.25}$$

The vectors $\hat{\boldsymbol{e}}_1$ and $\hat{\boldsymbol{e}}_2 = \hat{\boldsymbol{k}} \times \hat{\boldsymbol{e}}_1$ are two orthogonal unitary vectors perpendicular to $\boldsymbol{k}$. These form the polarization plane in which the electric field, with amplitude $\mathcal{E}_0$ and overall phase ϕ, oscillate. The polarization is described by the polarization angle α with respect to the $\hat{\boldsymbol{e}}_1$ axis, and the ellipticity ϵ.

As light propagates through a medium the properties of light, such as the electric field amplitude or the polarization angle, may change. These changes are driven by the interaction between the atomic population and the light. Note that in order to sense the medium properties, the light must couple atomic states and therefore influence the system being measured even if weakly.

The interaction between light and medium can be described using the Maxwell equations. An atomic ensemble does not feature free current density nor free electric charge density which simplifies the equations. Moreover, we assume that the magnetic response of the atoms to the probing light is negligible and therefore $\boldsymbol{H} = (1/\mu_0)\boldsymbol{B}$. The constant μ_0 is the permeability of free space. Note that the interaction can be seen in the definition of electric displacement,

$$\boldsymbol{D} = \epsilon_0\boldsymbol{\mathcal{E}} + \boldsymbol{P}, \tag{3.26}$$

where ϵ_0 is the permittivity of free space. The induced polarization of the medium, $\boldsymbol{P}$, indicates the electric dipole moment per unit volume of the atomic ensemble. This quantity can be expressed in terms of the atomic populations described by the density matrix obtained from solving Eq. (3.24) as

$$\boldsymbol{P} = n\mathrm{Tr}(\rho\boldsymbol{d}). \tag{3.27}$$

The atomic density is given by n and the dipole operator defined as $\boldsymbol{d} = e\hat{\boldsymbol{r}}$.

Simplifying the Maxwell equations for a plane wave and assuming the same time dependence for $\mathcal{E}$ and $\boldsymbol{P}$ we find that,

$$\frac{\partial^2\mathcal{E}}{\partial^2\ell} + k^2\mathcal{E} = -\frac{k^2}{\epsilon_0}\boldsymbol{P}, \tag{3.28}$$

where ℓ is the distance along the light propagation direction.

The solution of Eq. (3.28) characterizes the dynamics of the polarization angle and ellipticity as light travels through a medium. These polarization parameters were defined in Eq. (3.25) for a plane wave. The influence of the medium is hidden in the definition of the induced polarization in Eq. (3.27). In turn, this definition relies in the quantum description of the interaction of an atomic medium with light given in Eq. (3.24).

3.6 INTUITIVE APPROACH TO OPTICAL ATOMIC MAGNETOMETERS

Given the large array of implementations for optical atomic magnetometers and the heterogeneity of the GNOME network, general expressions were provided in the first part of this chapter. These formally describe how magnetic field, atoms and light interact with each other, and serve as an introduction to the tools for modeling any magnetometer set-up. However, it is difficult to develop and intuition for the fundamentals of magnetometry looking at the equations. This sections provides a qualitative description of the basic physics involved in atomic magnetometers.

Consider a simple case for a two level system with the ground state having spin $F = 1$, and excited state $F = 0$. Light propagation and magnetic field are aligned along the z-axis. An external magnetic field shifts the Zeeman levels by $\Delta E_{\text{Zeeman}} = g_F\mu_B B_z$ while light couples ground and excited states. The unperturbed energy difference between ground and excited state is given by $\Delta E_0 = \hbar\omega_0$. If exciting with circular polarized light, transitions satisfy the condition that $\Delta m_F = 1$ or -1. The described system is graphically represented in Fig. 3.3b.

The effect of the medium on the properties of light in the system presented in Fig. 3.3b, can be completely described by Eqs. (3.28) and (3.27). A general solution can be cumbersome to obtain (see Ref. [106]). However, for getting a qualitative picture, it is enough to consider the resonance properties of the medium to the circular components of light.

The phase shift and the attenuation experienced by a weak light field can be modeled by the complex refractive index η. For a circularly

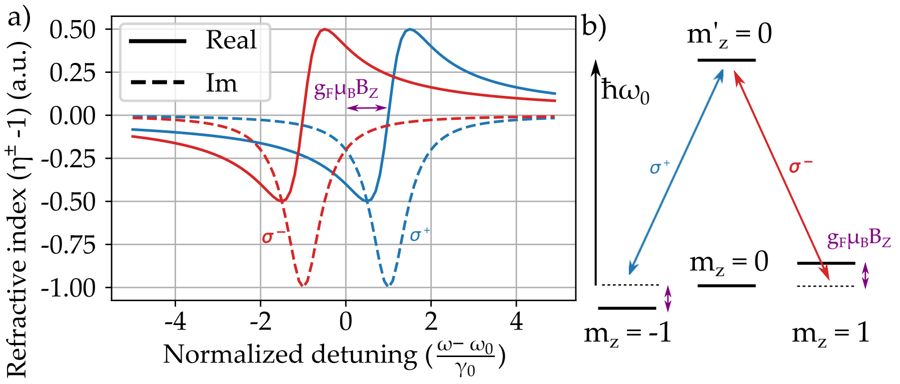

Figure 3.3: Magnetic field dependence of the refraction index and transition frequency. a) Complex refraction index $\eta - 1$ of an atomic ensemble for circularly polarized light under the influence of a constant magnetic field along the light propagation axis B_z. Blue and red indicate the effect on right and left circularly polarized light while solid and dashed lines show the real and imaginary components of $\eta - 1$. b) Energy-level diagram for an atomic transition with ground state $F = 1$ and excited state $F' = 0$. Zeeman sublevels are shifted in the presence of a magnetic field in the z-axis, changing the resonance frequencies for left- and right-circularly polarized light propagating along z.

polarized light field, η depends on the frequency of the light ω_0 and the magnetic field B_z around the optical resonance frequency as

$$\eta^{\pm}(\omega) \approx 1 + \chi_0 \frac{\gamma_0}{4(\omega - \omega_0 \pm g_F \mu_0 B_z) + 2i\gamma_0}, \tag{3.29}$$

where γ_0 spontaneous decay rate from excited to ground state and χ_0 is the amplitude of the linear electric susceptibility. The imaginary part describes absorption and the real part refraction. The dependence of the components of η on magnetic field and detuning from resonance is plotted in Fig. 3.3a.

The difference in absorption and refraction for the circular components of light are called circular dichroism and circular birefrigence respectively. The first changes the elipticity of an incoming beam while the latter tilts the polarization. One could directly use this effect to measure magnetic fields. However, such a measurement would strongly dependent on experimental parameters like the optical path and the light frequency. Additionally, the effect occurs at d.c. which is experimentally challenging to measure accurately.

Contrarily, most magnetometers are based on magnetic resonance effects. By optical pumping, ground level spin projection states can be depopulated preventing light to interact with some of the levels. For example if all the atomic population lies in the ground $m_F = 1$ state, only σ^--light propagating along z-axis can interact with the atoms while resonant σ^+-light cannot. Additionally, the frequency of an external oscillating magnetic field along x-axis can be scanned. When coinciding with the Larmor frequency $\omega_L = g_F \mu_0 B_z$, the ground state levels are coupled and a sudden change in the optical properties of the atomic ensemble can be observed. A general schematic can be seen in Fig. 3.4.

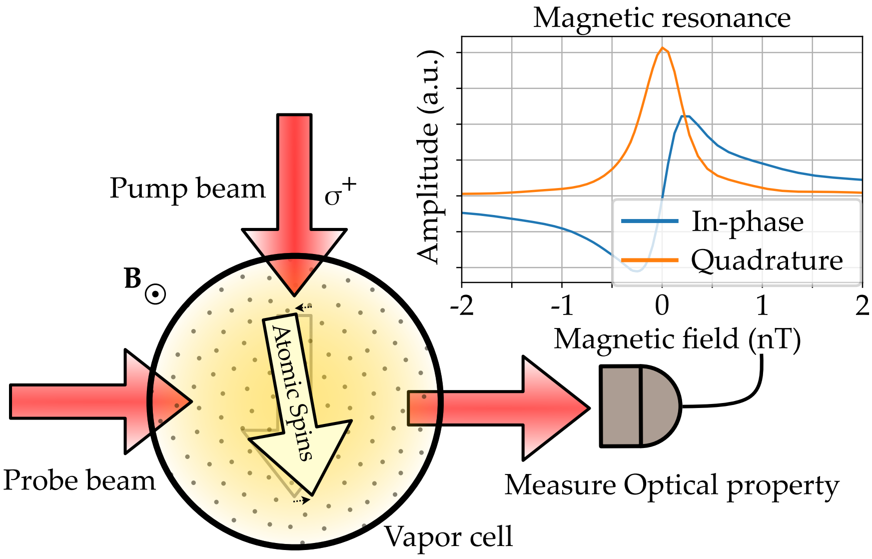

Figure 3.4: General schematic of an optical magnetometer. The magnetic resonance serves to determine an applied magnetic field $\boldsymbol{B}$. Magnetometer image adapted from Twarge , CC BY-SA 4.0, via Wikimedia Commons

A popular magnetometer type in the GNOME network is the so called non-linear magneto-optical rotation (NMOR) magnetometer. These are based on resonant driving of atomic spins in the atomic ensemble. A linearly polarized probe light, i.e. the beam whose properties are being measured, propagates along the x-axis. An offset magnetic field is aligned along the z-axis producing a Zeeman splitting along that axis. The atomic ensemble is optically pumped by a circularly polarized beam propagating along the z-axis. This directs the spins producing a macroscopic magnetization. Finally, a magnetic field along the y-axis is modulated at the Larmor frequency. This tilts the magnetization of the ensemble which is not anymore aligned with the magnetic field. Therefore, the atoms start precessing in the xy-plane at the modulation frequency. Changes on the amplitude of the precesion are detected if the modulation frequency slightly differs from the Larmor frequency. Due to the offset magnetic field, the Larmor frequency is to first order of approximation proportional to magnetic fields along the z-axis. This is typically called the sensitive axis of the magnetometer. Here is just one in a plethora of realizations. A similar effect can be measured by omitting the modulated magnetic field. Then the pump beam should be modulated (intensity, frequency or polarization) and aligned along the y-axis.

SERF magnetometers can reach higher magnetic field sensitivities than NMOR by avoiding spin-exchange collisions as discussed in Sec. 3.3. High vapor density and a near-zero magnetic field cause the Larmor frequency to be much slower than the spin-exchange collision rate. This effectively averages out the effect of spin-exchange collisions (see Fig. 3.2). A typical two-beam configuration for a SERF magnetometer utilizes a circularly polarized pump beam along the z-axis creating a magnetization along that axis. Through polarization or intensity the probe beam measures the magnetization component along its propagation axis. It is common to propagate the probe beam along the x-axis. Even though the magnetometer is sensitive to all magnetic field direction, the configuration presented is to first order (in the magnetic field) sensitive to the projection of the field onto the y-axis. A magnetic field along the y-axis produces a steady state tilt of the magnetization towards the x-axis. This tilt depends on different experimental parameters but it can be calibrated to extract a magnetic field measurement.

4

GLOBAL NETWORK OF OPTICAL MAGNETOMETERS FOR EXOTIC PHYSICS SEARCHES

This chapter is intended to give an overview of GNOME. It discusses the general characteristics of the magnetometers as well as the infrastructure used for data collection and storage. In Ref. [120] this information was published by the GNOME collaboration. Therefore parts of this chapter are directly extracted and adapted from Ref. [120].

The Global Network of Optical Magnetometers to search for Exotic physics (GNOME) is a network of geographically separated, time-synchronized, optically pumped atomic magnetometers that is being used to search for transient or permanent correlated signals heralding exotic physics.

All the existing GNOME sensors are optically pumped atomic magnetometers (see Chapter 3) that measure the spin precession of alkali atoms by observing the time-varying optical properties of the alkali vapor with a laser beam. The alkali vapor is contained within a glass cell which can contain a buffer gas or feature an anti-relaxation coating. The vapor cell is located inside a set of magnetic-field coils that enable control of homogeneous longitudinal and transverse components of an applied magnetic fields as well as (for some stations) magnetic field gradients.

Each magnetometer is located within a multi-layer magnetic shield to reduce the influence of magnetic noise and perturbations, while retaining sensitivity to exotic fields and interactions [121]. The shield provides an attenuation to external fields to a part in 10^5 or better. Even with magnetic-shielding techniques, there is inevitably some level of magnetic and non-magnetic transients from both local (such as movement of magnetized objects, devices turning on, vibrations, temperature changes etc.) as well as global sources (such as solar wind, changes of the Earth's magnetic field, etc.). Therefore, each GNOME magnetometer uses auxiliary sensors (unshielded magnetometers, accelerometers, gyroscopes, and other devices) to measure relevant environmental conditions, allowing for exclusion/vetoing of data for which there are identifiable sources generating transient signals. If the readings from these auxiliary sensors present abnormalities, the data from the corresponding magnetometer are flagged as suspect during this time.

The signals from the GNOME magnetometers are recorded with accurate timing provided by the Global Positioning System (GPS) using a custom GPS-disciplined data acquisition system [122]. The data are then redundantly uploaded to two data storage facilities in Mainz (Germany) and Daejeon (South Korea). The analysis work is predominantly executed in a server with sit in Mainz. The server, which has convenient access to the data, is used remotely by all members of the collaboration.

4.1 THE SENSORS CONSTITUTING GNOME

GNOME is a heterogeneous set of magnetometers. At the time of writing this thesis, GNOME embraces 12 magnetometers in the following locations: Mainz (Germany), Jena, (Germany) Krakow (Poland), Belgrade (Serbia), Beersheba (Israel), Beijing (China), Hefei (China) , Daejeon (South Korea), Canberra (Australia), Berkeley (USA), Hayward (USA), Los Angeles (USA), Lewisburg (USA), Oberlin (USA) and Plainsboro (USA). These feature different characteristics. While most are based on NMOR, there are also SERF and rf-driven magnetometers [123]. Mostly two different alkali atoms are used as sensing material: cesium and rubidium. As a result of the specific experimental configuration, each station features different bandwidth and sensitivities.

The heterogeneous nature of the network requires careful characterization of each station. The magnetometer signals are calibrated according to the dark matter model to force a comparable exotic coupling signal. Even though this variety can make the analysis complicated, it offers extra degrees of freedom to check the properties of a given exotic transient event. The characteristics of the stations that took part in Science Run 2 are summarized in Table 4.1. The table gives information about the location, orientation, magnetometer type, probed transition, and bandwidth of the different sensors.

Table 4.1: Characteristics of the magnetometers active during Science Run 2. Station name, geographic coordinates, orientation of the sensitive axis, magnetometer type, and probed transition are listed. The bandwidth indicates the measured -3 dB point of the magnetometers' frequency response to oscillating magnetic fields. Extracted from Ref. [3].

	Location		Orientation				
Station	Longitude	Latitude	Az	Alt	Type	Probed transition	Bandwidth
Beijing	116.1868° E	40.2457° N	+251°	0°	NMOR	^{133}Cs D2 F=4	115 Hz
Berkeley	122.2570° W	37.8723° N	0°	+90°	NMOR	^{133}Cs D2 F=4	7 Hz
Daejeon	127.3987° E	36.3909° N	0°	+90°	NMOR	^{133}Cs D2 F=4	10 Hz
Fribourg	7.1581° E	46.7930° N	+190°	0°	rf-driven	^{133}Cs D1 F=4	94 Hz
Hayward	122.0539° W	37.6564° N	0°	−90°	NMOR	^{85}Rb D2 F=3	37 Hz
Hefei	117.2526° E	31.8429° N	+90°	0°	SERF	^{85}Rb & ^{87}Rb D1	127 Hz
Krakow	19.9048° E	50.0289° N	+45°	0°	NMOR	^{87}Rb D1 F=2	3 Hz
Lewisburg	76.8825° W	40.9557° N	0°	+90°	SERF	^{87}Rb D2	200 Hz
Mainz	8.2354° E	49.9915° N	0°	−90°	NMOR	^{87}Rb D2 F=2	99 Hz

4.1.1 *Sensitivity*

The magnetometers in GNOME feature a range of different sensitivities to magnetic fields from tens to hundreds of $\mathrm{fT}/\sqrt{\mathrm{Hz}}$ at around 10 Hz. Fundamentally, the sensitivity of the magnetometer is limited by the combination of different quantum uncertainty sources from which the spin projection noise is the most relevant (see Eq. 3.22).

However, from the point of view of the sensor operator, the sensitivity is determined by the characteristics of the magnetic field resonance lineshape (see Fig. 3.3). The higher the ratio amplitude over width, the greater the sensitivity. This ratio is mainly determined by factors that influence the coherence time of the spin precession such as: collision rate, laser powers, magnetic field inhomogeneities, and atomic density.

The environment imposes a noise floor that needs to be surpassed in order to detect a signal. Different factors contribute to this noise floor such as vibrations, laser noise, electronic noise, temperature fluctuations etc. Typically, such systematic noises determine the sensitivity at different frequencies as well as the measurement stability. The stability limits how long the data can be effectively averaged. Figure 4.1 shows the Fourier transform and the Allan deviation of some GNOME magnetometers. The figure shows that the sensors feature different noise floors. In Mainz, one can observe a broad peak at around 10^2 Hz corresponding to the overshot of the feedback loop used to adjust the bandwidth to 100 Hz. The Allan deviation plot shows a typical structure in which the deviation increases for short and long time periods while it founds a minimum or a plateau in the middle. The averaging time is optimized at the value of τ having the minimal deviation. Past that point longer averages do not improve the sensitivity of the sensor.

4.1.1.1 *Directional sensitivity*

As mentioned in Sec. 3.6 the magnetometers used in GNOME are first-order sensitive along their sensitive axis $\hat{\boldsymbol{n}}_j$, where j indexes the magnetometer. Consider ALP domain walls (see Sec. 2.3) to produce a uniform normalized pseudo-magnetic field[1] with magnitude $\mathcal{B}_p$ over Earth. Such a field points along a fixed direction in the galactic frame, $\hat{\boldsymbol{n}}_{dw}$. The response in each magnetometer varies based on the dot product between $\hat{\boldsymbol{n}}_j$ and $\hat{\boldsymbol{n}}_{dw}$. Table 4.1 lists the directional sensitivity and locations of the GNOME sensors.

The dominant speed of Earth in the galactic frame is the rotation of the solar system among the galaxy. This results in an apparent velocity towards the constellation Cygnus $|\boldsymbol{v}_L| \approx 220\,\mathrm{km/s}$. Assuming $\mathcal{B}_p$ along $-\boldsymbol{v}_L$, the daily modulation of the sensitivity due to Earth rotation can be seen in Fig. 4.2.

---

[1] This name chosen to be consistent with Ref. [3]. It refers to the magnetic field strength equivalent to the ALP domain wall interaction, see Eq. (5.14).

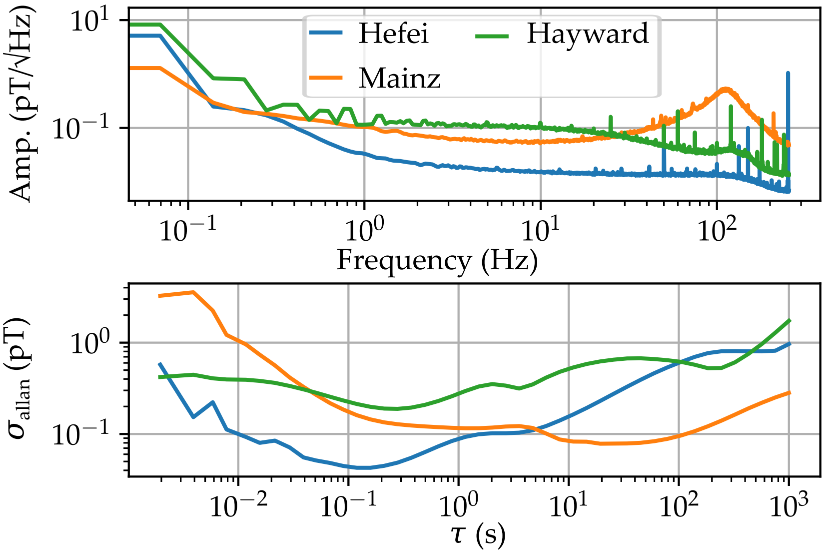

Figure 4.1: Noise floor and frequency stability of three GNOME magnetometers. Upper plot: amplitude spectral density (ASD). Lower plot: Allan variance. Calculated using two hours of data sampled at 512 Samples/s from Science Run 2 starting on 02.12.2017 at 18:00. A moving average for 10^3 points and a downsampling to one point each 5×10^2 points are applied to the figures.

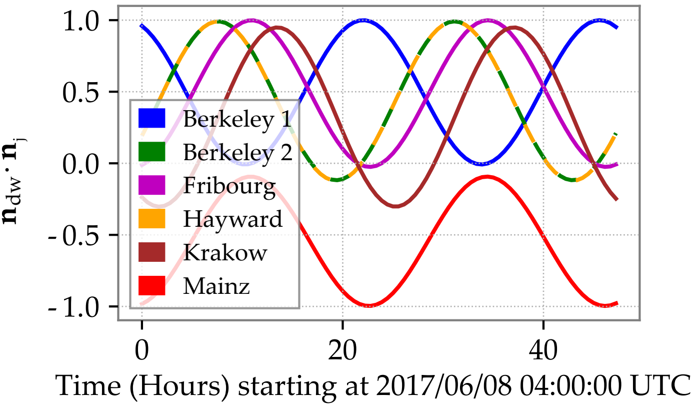

Figure 4.2: Daily modulation of the effective sensitivity of six GNOME magnetometers. This results from Earth rotation with respect to a constant direction in the galactic frame. The domain wall direction, $\hat{n}_{\text{dw}}$, is assumed to point from the Cygnus constellation.

4.1.1.2 *Calibration error*

The magnetometers rely on a proportionality factor in order to convert the output signal (usually voltage) to magnetic field. The central part of the dispersive quadrature (or the phase) component of the resonance can be approximated by a straight line (see Fig. 3.3). After calibrating this linear regime one can convert signal amplitude to magnetic field through a proportionality factor. This factor is fixed when collecting data until the magnetometer is re-calibrated.

Auxiliary measurements have shown that the calibration factors experience fluctuations over time due to, for example, changes in

Table 4.2: Estimation of the calibration error for the magnetometers active during Science Run 2.

Station	Calibration Error
Beijing	20%
Berkeley	40%
Daejeon	20%
Fribourg	5 %
Hayward	5 %
Hefei	5 %
Krakow	20%
Lewisburg	10%
Mainz	2 %

the environmental conditions (temperature, humidity, laser configuration...). Upper limits on the calibration factor errors due to such drifts over the course of Science Run 2 have been evaluated and are listed in Table 4.2. Errors in the calibration factor result in magnetic field measurement uncertainties proportional to the local pseudo-magnetic field response B_j.

4.1.2 *Bandwidth*

The magnetometers in GNOME feature a range of different bandwidth capabilities; from few to a couple hundreds Hertz (see Table 4.1). This parameter quantifies the speed of the magnetometer response to a transient. If the bandwidth does not cover all the frequency components, the signal lineshape will be deformed. Due to the disparity in bandwidths, the same signal could be deformed differently by each magnetometer. In order to avoid this, the analysis is restricted to a frequency window within the bandwidth of all sensors. In latter Science Runs, the magnetometers are forced to have the same bandwidth.

The bandwidth of a magnetometer is fundamentally determined by the width of the magnetic resonance. This is normally in the range of few Hz to hundred Hz. It is determined by $(2\pi T_2)^{-1/2}$, where T_2 is the transverse spin coherence time of the alkali vapor cell. Such a quantity accounts for all processes that decohere the atomic spin precession. Note that the sensitivity is also dependent on this parameter (see Eq. (3.22)). Techniques to increase this fundamental bandwidth deteriorate the sensitivity. One needs to find the optimal trade-off for the particular application at hands. During Science Run 2, the different research groups in GNOME chose their optimization parameters according to their preferences. This gave rise to the range of bandwidth in the network.

The magnetometer's bandwidth can be tuned in different ways. When operating the in the so called open loop mode, no feedback is provided to keep the system on resonance. The external field modulation frequency is fixed, initially near the Larmor frequency. A signal is obtained by exploiting the magnetic field dependence of an optical property near resonance (see Sec. 3.6). The signal amplitude depends on the frequency difference between Larmor and excitation frequencies. Atoms respond instantaneously to a magnetic field shifting their Larmor frequency. However, the atoms need some time to precess at a new frequency. The characteristic time for the atoms to recover the maximum amplitude at this new frequency is given by the inverse of the resonance width. Spin decoherence mechanism in the cell determine the resonance width. The longer the coherence time, the smaller the width. In order to increase the bandwidth, decoherence mechanisms must be enhanced such as light power, collisions etc.

In contrast, when operating in the so called close loop mode, a feedback to excitation field is provided to keep the system on resonance. The excitation field is set to follow changes on the Larmor frequency. In this case, the response to a magnetic field is given by the amplitude of the feedback signal needed to keep the system on resonance. Now, the limiting factor for the bandwidth is the speed of the electronics following the variations in the Larmor frequency. Changing the parameters of the feedback, such as the gain, the bandwidth can be increased precisely to the desired value. However, as the open loop case, the sensitivity is reduced.

Just at the start of Science Run 2 a train of sinusoidal magnetic field signals at different frequencies was applied to the magnetometers to characterize their bandwidth. The result of this calibration exercise can be seen in Fig. 4.3 for three magnetometers. One can see that the sensor in Hayward has significantly shorter bandwidth than the other two. The Mainz sensor has faster roll-off than Hefei. This plot is really important for complementing the sensitivity information delivered by Fig. 4.1.

In latter runs such a pulse is given every hour to monitor sensitivity and bandwidth. In order to suppress frequency components higher than the bandwidth a low-pass filter with a cut-off frequency at 150 Hz is inserted at the output of each magnetometer.

4.1.3 *Projection of the proton spin onto the magnetization*

Although the GNOME is a network of magnetometers, ultimately the goal of the GNOME is not to search for magnetic-field transients but rather to search for exotic couplings to nuclear spins. While it is practical to measure and compare the sensitivities of the magnetometers to magnetic fields, the exotic spin interactions couple to proton, neutron, and electron spins with different strengths in comparison to magnetic fields. Here, it is assumed that the targeted exotic

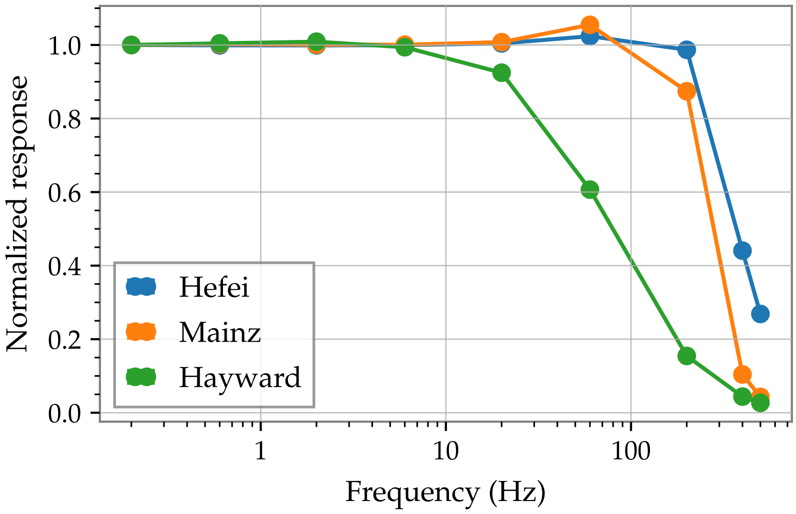

Figure 4.3: Transfer functions of three GNOME magnetometers just before Science Run 2.

spin interaction just couples to proton spins. Two reason backup this assumption: couplings with electron spins are counteracted by the magnetic shield [121] and alkali atoms have a single valence proton which makes them particularly sensitive to the coupling with protons [32].

Magnetometers sense perturbations to the total atomic spin $\hat{\boldsymbol{F}}$. To interpret the data in terms of the proton spin $\hat{\boldsymbol{S}}_p$, a relatively simple framework for modeling the response of magnetometers to exotic spin-dependent interactions is employed [32]. Such model is valid to first-order for electrons and valence nucleons. The factors that relate the total atomic angular momentum and the proton spin are discussed in Sec. 3.1.2. Table 4.3 lists the fractional proton spin polarization $\sigma_{p,F}$ for the GNOME magnetometers.

In the SERF regime the effective response of the magnetometer is the result of an average over the hyperfine ground state levels. The magnetization precession is reduced due to the average performed by the high rate of spin-exchange collisions over the hyperfine levels. This can be considered by an effective Landé g-factor $\langle g \rangle_{hf}$. Additionally, the average projection of the proton spin over the hyperfine states onto the total magnetization $\langle \sigma_p \rangle_{hf}$ must also be considered. This effective parameters are included in Table 4.3. Details in the determination of these parameters can be found in Appendix B in Ref. [3].

Uncertainties in the values for $\sigma_{p,F}$ describe the range of different results from calculations based on the Schmidt model, semi-empirical models [109, 110], and large-scale nuclear shell model calculations where available [111–113].

4.2 THE MAINZ STATION

Mainz had a dedicated two beam atomic optical magnetometer. The set-up was constructed during my master thesis and maintained dur-

Table 4.3: Effective parameters relating a direct coupling with the valence proton to the magnetic response. Fractional proton spin polarization $\sigma_{p,F}$, Landé g-factors g_F and their ratios for the ground state hyperfine levels used in GNOME. The weighted average of these values across both hyperfine levels ($\langle\sigma_p\rangle_{hf}/\langle g\rangle_{hf}$) is applicable to SERF magnetometers in the low-spin-polarization limit. The uncertainties in $\sigma_{p,F}$ and $\langle\sigma_p\rangle_{hf}$ are one-sided because alternative methods to the Schmidt model generally predict smaller absolute values of the proton spin polarization. See Ref. [32] for further details.

Atom (state)	$\sigma_{p,F}$	g_F	$\sigma_{p,F}/g_F$	$\langle\sigma_p\rangle_{hf}/\langle g\rangle_{hf}$
^{39}K ($F = 2$)	$-0.15^{+0.06}_{-0.00}$	0.50	$-0.30^{+0.12}_{-0.00}$	$-0.5^{+0.2}_{-0.0}$
^{39}K ($F = 1$)	$-0.25^{+0.10}_{-0.00}$	-0.50	$0.50^{+0.00}_{-0.19}$	
^{85}Rb ($F = 3$)	$-0.12^{+0.02}_{-0.00}$	0.33	$-0.36^{+0.05}_{-0.00}$	$-0.8^{+0.1}_{-0.0}$
^{85}Rb ($F = 2$)	$-0.17^{+0.02}_{-0.00}$	-0.33	$0.50^{+0.00}_{-0.07}$	
^{87}Rb ($F = 2$)	$0.25^{+0.00}_{-0.05}$	0.50	$0.50^{+0.00}_{-0.11}$	$0.8^{+0.0}_{-0.2}$
^{87}Rb ($F = 1$)	$0.42^{+0.00}_{-0.09}$	-0.50	$-0.83^{+0.18}_{-0.00}$	
^{133}Cs ($F = 4$)	$-0.10^{+0.05}_{-0.00}$	0.25	$-0.39^{+0.19}_{-0.00}$	$-1.2^{+0.6}_{-0.0}$
^{133}Cs ($F = 3$)	$-0.13^{+0.06}_{-0.00}$	-0.25	$0.50^{+0.00}_{-0.24}$	

ing this work. The main drawback of such set-up is the long term stability of the lasers. Since Science Run 4 a commercial sensor from Quspin Inc. is employed as the Mainz station. This is a miniaturized and robust SERF magnetometer based on a rubidium vapor cell. In the future, we envision the use of a co-magnetometer using helium, potassium and rubidium. This more sophisticated device compared to a SERF magnetometer is insensitive to magnetic fields. However, the sensitivity to neutron and proton couplings is greatly improved. A comparison of the sensitivity to exotic spin coupling SERF and co-magnetometers can be found in Ref. [124].

4.2.1 *Set-up during Science Run 2*

The Mainz GNOME station is a two-beam amplitude modulated NMOR magnetometer. The sensor is based on an evacuated paraffin-coated ^{87}Rb vapor cell placed in a magnetically shielded environment. This system is located in the basement of the Helmholtz Institute Mainz in a temperature-stabilized laboratory.

The paraffin-coated ^{87}Rb vapor cell at the center of the apparatus has a cylindrical shape with length of 5 cm and diameter of 5 cm. The measurements are performed at a stabilized room temperature of 21 °C. At this temperature the atomic density is 8.2×10^9 atoms/cm^3. The cell is placed inside a custom four-layer mu-metal shield. A set of

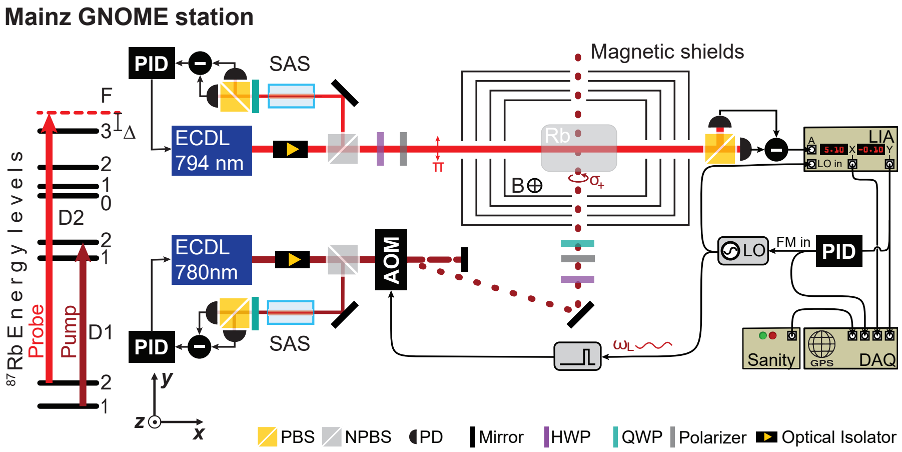

Figure 4.4: Schematic diagram of the GNOME magnetometer in Mainz. Extracted from Ref. [120]. Notation: ECDL = extended-cavity diode laser; SAS = saturated absorption spectroscopy setup; NPBS = non-polarizing beamsplitter; OI = optical isolator; PMF = polarization-maintaining fiber; AM = amplitude modulator; PI = proportional-integral control loop electronics; LPF = low-pass filter; P = linear polarizer; PD = photodiode; NDF = neutral density filter; $\lambda/2$ = half-wave plate; $\lambda/4$ = quarter-wave plate; WP = Wollaston prism; BPR = balanced photo receiver; VCO = voltage controlled oscillator; LIA = lock-in amplifier; Sanity = Sanity monitor (see Sec. 4.3.2); DAQ = DM DAQ (see Sec. 4.3.1).

three square magnetic coils is located inside the shields with their axes aligned so that they are mutually perpendicular. The coil that defines the $\hat{z}$-axis is oriented perpendicular to the ground. It establishes the direction of the leading magnetic field which has a magnitude of 525 pT pointing towards the ground. The current supply SEL-1 manufactured by Magnicon provides a highly stable current for driving the coils.

The linearly polarized probe beam, which propagates in the $\hat{x}$-direction, is generated by a external-cavity diode laser ECDL system (Moglabs CEL002). The optical frequency is locked to the D2 crossover between the $5\ ^2S_{1/2},\ F = 3 \rightarrow 5\ ^2P_{3/2},\ F' = 3$ and $F' = 4$ transitions of ^{85}Rb using a custom-made saturated absorption spectroscopy system (SAS); the error signal is produced by frequency modulation at 100 kHz. This locking point is detuned by $+1.2$ GHz from the ^{87}Rb $5\ ^2S_{1/2},\ F = 2 \rightarrow 5\ ^2P_{1/2},\ F' = 2$ transition. Before going through the atomic sample, the beam is linearly polarized. The probe beam measures the population dynamics in the Zeeman sublevels of the $5\ ^2S_{1/2},\ F = 2$ state. The beam power is fixed to 368 μW. The optical rotation produced by the precessing spins is measured with a differential polarimeter composed of a Wollaston prism and a balanced photoreceiver (Thorlabs PDB210A).

The sinusoidal signal from the polarimeter which oscillates at the pump beam amplitude pulsing frequency ω_{mod} is processed with a two-phase lock-in amplifier (LIA) (Standford Research Systems SR830). The reference signal is given by the local oscillator that produces the pump-pulse frequency. The LIA outputs the two quadratures of the signal. In order to cut before the Nyquist frequency of 250 Hz, the bandwidth is limited to 150 Hz. A time constant of 300 µs with roll-off −24 dB/octave is set in the LIA. The out-of-phase output is used to lock the local oscillator frequency on resonance, $\omega_{\text{mod}} = \omega_{\text{L}}$. Since the in-phase component is maximal on resonance it can be used to confirms that the resonance condition is matched.

The pump beam is produced by an ECDL manufactured by Vitawave. Its optical frequency is locked to the resonance with the ^{87}Rb $5\ ^2S_{1/2}, F = 1 \rightarrow 5\ ^2P_{1/2}, F' = 2$ transition using a custom-made SAS. In order to produce the error signal for the SAS and lock to the transition, the pump beam is frequency-modulated at 10 kHz. The propagation takes place in the $\hat{y}$-direction and before interacting with the cell volume, the light is circularly polarized. To realize a stroboscopic excitation of the spin precession, the beam is periodically pulsed with a pulse duration of 1 µs from 0 to 4.1 mW using an acusto-optical modulator (AOM) manufactured by Isomet.

The AOM is driven by a function generator (Tektronix AFG2021) which allows modulation of the pulsing frequency ω_{mod} according to a voltage input through a voltage controlled oscillator (VCO). This feature is used to lock the pulsing frequency to the Larmor frequency using a proportional-integral-derivative (PID) controller based on the out-of-phase output of the lock-in amplifier. This feedback loop keeps the pulsing frequency tuned to the Larmor frequency ($\omega_{\text{mod}} = \omega_{\text{L}} = 2\pi \times 3791$ Hz). In this configuration, the magnetic-field changes are measured through the PID output voltage that controls the local oscillator. This signal scales with the magnetic field as 714.3 pT/V. In order to avoid aliasing due to the limited sampling rate of 512 samples/s the signal is further filtered before the DM DAQ. The filter used is a second-order Butterworth filter with a cut-off frequency of 200 Hz.

In order to monitor the magnetometer operational status, the amplitude of the absorption peak and the error signal from the SAS as well as the magnetic resonance amplitude are fed to the sanity monitor (Sec. 4.3.2).

4.2.2 *Mainz station update*

The Mainz station was replaced by a Quspin Inc. sensor enclosed in a MS-1 Twinleaf LLC magnetic shield. The new sensor is reliable and much more compact that the custom-made magnetometer. The QuSpin is a commercial SERF magnetometer based on rubidium. It features a very compact form factor being only 12.4x16.6x24.4 mm including calibration coils and laser system within the case. It requires a background magnetic close to zero and achieves a magnetic field sensitivity of less than 15 $\text{fT}/\sqrt{\text{Hz}}$ in a 3 to 100 Hz band.

The MS-1L Twinleaf magnetic shield features a shielding factor of 10^6 with 4 layers of mu-metal. The design incorporates a complete coil system with three axes coils and six gradient coils which are used to zero residual magnetic fields. A de-gaussing coil is also incorporated. The whole system is comprised in a compact cylinder with 220 mm diameter and 326 mm long. It has holes for optical access but these are not required for our purposes.

With this update a compact design, a low-maintenance and reliable sensor is obtained. In order to keep the magnetometer running without undesired interruptions, the calibration of the QuSpin sensor should be updated approximately once a week, otherwise it tends to malfunction. In addition, the automatic updates from the computer that retrieves the data must be deactivated. Otherwise the computer restarts automatically and data taking process is interrupted. Once a week the computer should be updated and restarted to guarantee continuous operation.

4.3 NETWORK'S HARDWARE AND SOFTWARE

In order to form a synchronized network with a set of scattered magnetometers, dedicated hardware and software is required. A global positioning system (GPS)-synchronized data acquisition system (DAQ) is used to record the magnetometer's signals and time-stamp them. The centralized and standardized storage of the data is accomplished by two programs. These are in charge of extracting the data from the GPS-DAQ, and sending it to a centralized storage service. Collaborators can independently access reliable and predictable data files.

4.3.1 *GPS-disciplined data acquisition system*

An important aspect of the operation of GNOME is the synchronous measurement by various stations spread all over Earth. This requires precise global timing, which needs to be available across the Earth. For this purpose, GPS is used. Depending on the number of visible satellites, the system can provide a time-accuracy better than 50 ns.

The Krakow GNOME group designed and built a dedicated GPS-disciplined data acquisition system (DM Technologies Data Acquisition System) used by all GNOME magnetometers to stream their data. It relies on a GPS antenna that is typically situated on the roof of the building in which the GNOME station is located. The GPS-DAQ has the ability to store several analog signals with precise timing and transfer them to a computer when needed. Additionally, the system provides a pulse-per-second (PPS) signal with an accuracy of 45 ns synchronized with GPS. This can be used to trigger synchronized signals. Details on the GPS-DAQ can be found in Ref. [122].

While GPS time is provided with a ±45 ns precision, it is not the only source of delay and uncertainty present in the system. Accounting for different sources, the cumulative delay corresponds to roughly 2 μs with an uncertainty of about ±200 ns. In case of signals propagating at the speed of light, this corresponds to a position uncertainty of less than 100 m; dark matter objects trapped in the Milky Way are expected to travel at a mean speed of $\sim 10^{-3}$ c, based on the timing accuracy the corresponding position uncertainty is less than 0.1 m.

4.3.2 *Sanity Monitor*

The magnetometers can occasionally become unreliable or experience strong environmental perturbations. The Fribourg GNOME group developed an system to automatically flag such unreliable periods. The device sends a 5 V constant voltage if the data is reliable and 0 V if the data in unreliable. This output is received by the GPS-DAQ and is used flag the data. The sanity monitor system features several analog inputs. The condition in the analog inputs for an unreliable magnetometer are set by the operator.

Technical issues that might produce transient spikes or false readings can be caused by, for example, loss of laser lock or failure of a system component, mechanical shocks, magnetic or electric pulses from neighboring devices, or human activity. If such identifiable errors are not properly flagged they might be falsely interpreted as or lead to missing an evidence of exotic physics.

The GNOME sanity monitor system is based on an Arduino MEGA 2560 microcontroller board with additional accelerometer, gyroscope, geomagnetic sensor Bosch BNO055 SiP on a single chip. The sensors are read out in 40 ms intervals. If a reading differs from the mean by a number of standard deviations specified by the operator, the data is marked with a 0 V output. Due to the diversity of factors that can trigger these sensors, and the lack of study about how much do these influence the magnetometer reading, the thresholds for marking the data are set relatively high. Such sensors aim to flag large perturbations in the set-up.

A dedicated Python-based software communicates with the Arduino microcontroller using the built-in USB interface. The graphical user interface (GUI) of the software enables the operator to set the values allowed for the analog inputs and Bosch BNO055 SiP sensors. After setting up the sanity monitor, the microcontroller can run without being connected to the PC. However, the software is able to log the readings if the sanity monitor remains connected allowing crosscheck and calibration.

4.3.3 *Data format, transfer, and storage*

The data from the GPS-DAQ are transferred to a computer. A Python-based program developed by Samer Afach parses and saves the data in files using the Hierarchical Data Format HDF5 [125]. The program is called GNOME Acquirer and can be downloaded from the collaboration web-page (https://budker.uni-mainz.de/gnome) under the downloads section. Each GNOME HDF5 file contains 60 s of data. HDF5 provides a tree data structure with multi-dimensional datasets which can also include meta-data and header-data referred to as “Attributes.”

A standard for the files is enforced in order to systematically process data. If the standards are not fulfill the data is not uploaded to the server. The files must contain two datasets named "Magnetic-

Fields" and "SanityData". These contain the magnetic field data and the sanity information respectively. The "MagneticFields" dataset contains floats with values convertible to the measured magnetic field. The "SanityData" dataset contains booleans sampled at one sample per second. These are true when the data is reliable and false when unreliable corresponding to the the sanity monitor giving 5 V and 0 V respectively.

Additionally, some attributes are required to interpret correctly the data. These are: sample rate, start and end time of the segment, an equation in string form to convert the raw data (e.g., voltage) into magnetic field units (e.g., pT), altitude, latitude and longitude of the station, and sensitive direction of the magnetometer. Stations can add additional datasets and attributes to the files if necessary enabling station-specific information.

After locally writing data to HDF5 files in the computer, the data are uploaded to two data-servers located in Mainz and Daejeon. The data transfer is done through a server/client pair developed in C++ by Samer Afach. The client can be downloaded from the collaboration web-page under the downloads section. The program, upon connecting to the server, is set to monitor a single directory. When a new data file appears, it is added to a queue for uploading, then it is tested for its integrity and compliance to the standards mentioned in the previous paragraph. If the conditions are fulfilled it is uploaded to the data servers.

Once uploaded to the server, the data can be visualized in real time at the collaboration web-page and downloaded at any time. A map shows the location of the stations together with a short description of the magnetometer, and the responsible operator. Active stations are shown in green, inactive stations are shown in red. Underneath the map, a time interval can be selected for visualization. The time series of each active station is shown together with the power spectral density of the showed time-series.

4.4 PERFORMANCE OF THE NETWORK

The first data taking of the history of GNOME was performed in 2013 [2]. Only two magnetometers took part in this data taking campaign. Namely, a magnetometer in Krakow and a magnetometer in Berkeley. This was a proof of principle to demonstrate the synchronous operation of two magnetometers. As well as the possibility of looking for coincidences between different sensors. Starting in 2016 the GNOME is established as a collaboration involving different groups around the world. Since then, data is reliably time stamped according to the GPS and saved in a structured fashion in common data server.

4.4.1 *Data collected*

GNOME started taking data as a network in 2016. The first runs where short, one day, and were focused on figuring out the requirements for running simultaneously during longer times. Different challenges were addressed in these characterization runs. The GPS synchronization was tested by inserting GPS-timed signals. Such signals were synchronously inserted using the PPS signal from the GPS-DAQ to all magnetometers in the network. Combination of sinusoidal signals were used in order to asses the time accuracy and bandwidth of the sensors. It was observed that due to technical problems, the sensors become insensitive or the calibration changed drastically while still streaming data. This made obvious the necessity of an interlock system to flag unreliable data. By measuring technical parameters of the magnetometer, like the magnetic resonance amplitude, one can identify when the system is not operating correctly. The standard for the HDF5 files was agreed upon, the sanity monitor was developed, and the software to retrieve and update the data was created.

The first official data taking period (SR1) took place between 6th of June and the 5th July of 2017. Six station conformed the network at that time: Berkeley 1 (USA), Berkeley 2 (USA), Fribourg (Switzerland), Hayward (USA), Krakow (Poland) and Mainz (Germany). Unreliable data was flagged with the sanity monitor. When observing the outcome of the run, the continuous data stream was frequently interrupted by flagged data. This limited the length of continuous data segments. The Berkeley stations went out of operation at the middle of the run. This made apparent that the long term stability of the magnetometers was a limiting factor. This left only four stations running which is the bare minimum to characterize the velocity and magnitude of a transient event. The frequent interruptions of the data stream drastically decrease the sensitivity of the network. Altogether a successful run but with a characteristic poor sensitivity.

A second run (SR2) was taken between 29th of November and the 22nd of December 2017. Four stations where added to the network: Beijing (China), Daejeon (South Korea), Hefei (China) and Lewisburg (USA) with respect to the first run. The number of magnetometers active was consistently above four. Previous to the run several characterization procedures were performed. The transfer function of each magnetometer was recorded. A random square pulse was inserted to offer an additional test to the bandwidth and timing. However, no characterization was performed periodically during the run. Drifts on the calibration factor made a correction during the analysis necessary (see Sec. 4.1.1.2). The data used for the domain wall search presented in this work is taken from this run.

A third run (SR3) spanned a larger period of time from the 1st of June 2018 to the 1st of June 2019. One station was added to the network: Oberlin (USA). The aim of the run was to take data for the longest time possible. Additionally a minimum value for the sensors' bandwidth of 100 Hz was established. Unfortunately, many stations underwent updates during the run. SR3 is characterized by a relatively low mean number of magnetometers active. It is just above 4 but it features a long time of operation. Most stations are experimental set-ups that cannot be dedicated exclusively to the GNOME network for long periods of time. Therefore, a clear finite plan needs to be

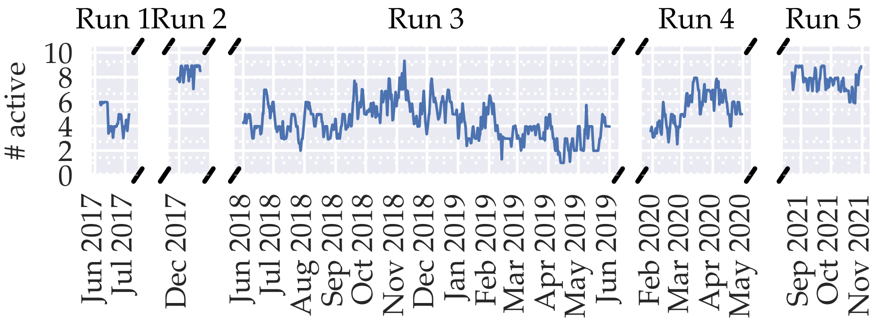

Figure 4.5: Overview of the number of sensors active during the GNOME science runs. It shows the one day rolling average of the number of sensors active.

communicated to the different teams. SR3 made obvious the necessity to state clear scientific and technical goals for the runs.

A forth run (SR4) spanned between the 30th of January and the 30th of April of 2020. The Fribourg set-up was transferred to Moxa (Germany). The run was interrupted by the COVID-19 pandemic. Since the magnetometer maintenance could not take place, the magnetometers stopped working. The run incorporated a new characterization procedure, a pulse containing four second sinusoidal signals at 1 Hz, 10 Hz and 100 Hz was given to the magnetometer once an hour. This made possible to identify the calibration drift experienced by the magnetometers (see Sec. 4.1.1.2). Then an estimate was done for SR2. This showed the need to periodically calibrate the magnetometers.

The fifth run (SR5) spanned between 23rd of August 2021 and the 31st of October 2021. It features a mean of seven magnetometers active. Additionally the sensitivity of the sensors is periodically tracked by a calibration pulse every hour. The calibration pulse consists of a set of a sinusoidal signals with 100 pT constant amplitude and a total duration of 9 s. It is divided in 11 sections in which the frequency is scanned from 1 to 190 Hz. This monitors the sensitivity and transfer function of the magnetometers allowing for a re-calibration in the analysis stage.

A summary of the science runs performed by GNOME since 2016 is shown is Fig. 4.5. It shows one day rolling average of the mean number of magnetometer active for one hour.

4.4.2 *Network sensitivity*

The GNOME data can be used in very different ways to search for exotic physics. Depending on the analysis procedure the sensitivity of the network is evaluated differently. A simple, model independent evaluation of the networks' sensitivity is given by

$$\sigma_{\text{network}} = \sqrt{\frac{1}{\sum_j \sigma_j^{-2}}}. \tag{4.1}$$

The equation shows the uncertainty propagated to the weighted mean $\bar{x}_i = \sum_j w_j x_j / \sum_j w_j$, where x_j denotes a measured value and j labels

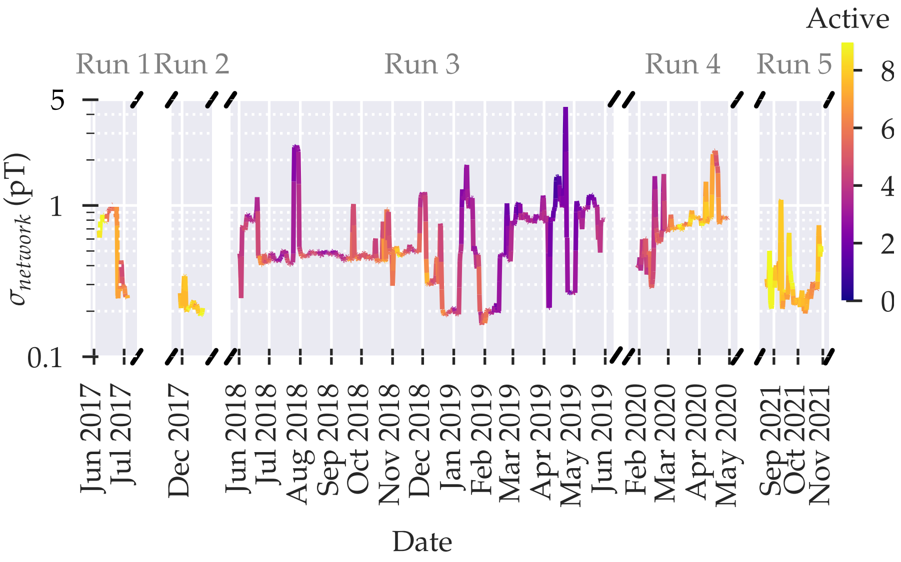

Figure 4.6: Overview of the sensitivity during the GNOME science runs. One-day rolling average of the standard deviation of the network. This is calculated according to Eq. (4.1). The standard deviation is calculated over a second of data. Then this information is averaged for one hour.

the magnetometers. This is the weighted mean over the measurement at each magnetometers at a given time. The weights are equal to the inverse of the variance, $w_j = 1/\sigma_j^2$. A weighted mean defined in this manner provides the best estimator for the mean under the assumption that local measurements are independent and normally distributed with the same mean. Even though the magnetometer's noise is not strictly Gaussian, σ_{network} allows for a rough estimation the network's performance.

A noise assessment considering the peculiarities of the domain-wall search was published in Refs. [3, 36]. To effectively observe domain walls, the sensitive axis of the active sensors must cover the three spatial directions. Otherwise, the network sensitivity to such objects strongly degrades.

The network performance for the five GNOME Science Runs can be seen in Fig. 4.6. The figure shows the one-hour-average noise level as defined in Eq. (4.1). This average is calculated using the standard deviation for each second of data. Since the measurements are taken in one-second intervals, no missing or insane are possibly present within the second. Insane or missing full seconds are dropped when calculating the one-hour average.

4.4.3 *Network directional sensitivity*

Since the magnetometers measure along one axis, the sensitivity of the network is directional. Magnetic fields pointing at an angle to the sensitive axes are attenuated. One can assess the directional sensitivity of the network by considering the attenuation for different directions in Earth's reference frame. It is important to note that the local noise level of each magnetometer have a considerable impact in global directional sensitivity. The ideal configuration should reach an isotropic network sensitivity.

To first order, the attenuation experienced by a magnetometer, j, to the direction $\hat{\boldsymbol{n}}_{\mathrm{dw}}$ is given by the dot product with the sensitive axis, $\hat{\boldsymbol{n}}_j$. The network sensitivity to such direction can be approximated by

$$\sigma_{\hat{\boldsymbol{n}}_{\mathrm{dw}}} = \sqrt{\frac{1}{\sum_j (\hat{\boldsymbol{n}}_{\mathrm{dw}} \cdot \hat{\boldsymbol{n}}_j)^2 / \bar{\sigma}_j^2}}, \tag{4.2}$$

where $\bar{\sigma}_j$ is the estimated average noise level of a magnetometer. Such equation follows from the uncertainty propagated to the weighted mean as in Eq. (4.1). The weight is defined to consider the attenuation of the signal due to the sensitive axis as $w_j = (\hat{\boldsymbol{n}}_{\mathrm{dw}} \cdot \hat{\boldsymbol{n}}_j)/\bar{\sigma}_j^2$. Such definition will provide the best estimation of the mean considering directional sensitivity and local noise. The estimated average noise level $\bar{\sigma}_i$ is calculated by averaging the standard deviation evaluated for 1 s segments for the whole Science Run 2 data.

Figure 4.7 shows the estimated directional sensitivity during Science Run 2. One can observe that the ratio between most and least sensitive direction is a factor of 2.3. The worst-case scenario for the network would be a magnetic field perpendicular to the earth surface at around Bolivia or equivalently the Chinese sea. An optimal location and/or orientation of a new sensor would be the one covering such direction. Note that the new sensors does not have to be at a specific location but the directional sensitivity has to be tuned to cover such worst direction. A comprehensive study of the sensitivity of a network of vector-field sensors can be found in Ref. [126].

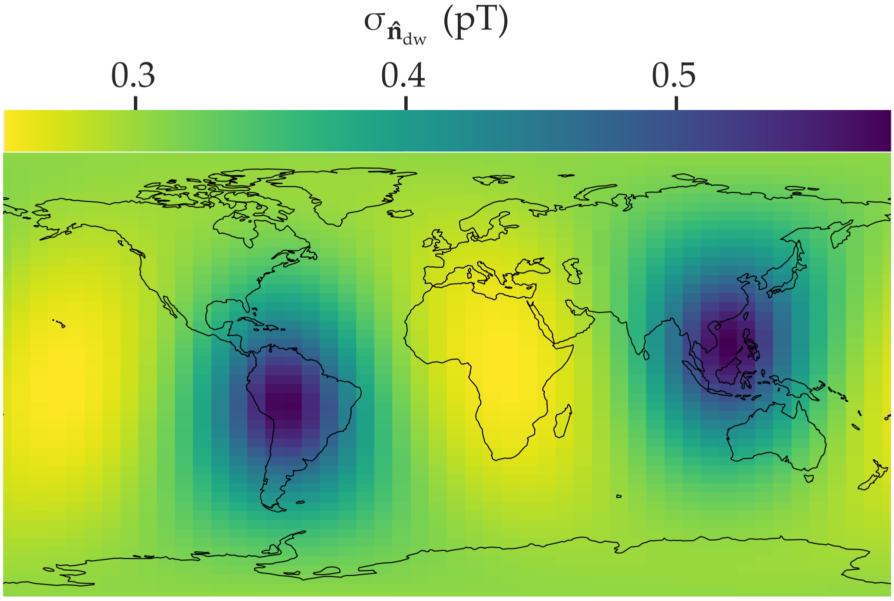

Figure 4.7: Directional sensitivity of GNOME during Science Run 2 in geographic coordinates. This quantity is defined in Eq. (4.2). Here $\hat{n}_{\text{dw}}$ is a vector perpendicular to the surface at each point on Earth. The color shows the magnitude needed to produce a one signal-to-noise ratio signal in the GNOME network.

5

TARGET DARK MATTER SCENARIO

The main piece of work discussed in this dissertation is the search for ALP domain walls using the GNOME Science Run 2 data. This chapter is dedicated to define the properties of the ALP domain walls. Particular to ALPs is the independence between mass, symmetry breaking scale, and coupling strength with ordinary matter. Section 5.1 relates the symmetry breaking scale and the ALP mass with the domain wall thickness and expected crossing rate with earth. The coupling to ordinary matter is described in Sec. 5.2. The dynamics of the domain walls influence our observations changing, for example, the observed thickness. A generalization of the SHM for planar objects is discussed in Sec. 5.3 which is used to constraint the domain wall dynamics.

This chapter is an adaptation of the information published in Ref. [3] and Ref. [36]. These two realize the proposal presented in Refs. [2, 127] to search for ALP domain walls using a network of optical magnetometers. Additionally my colleague Joseph A. Smiga extensively studied the theory, formation and shape of ALP domain walls in his doctoral thesis [128].

5.1 AXION-LIKE PARTICLE DOMAIN WALLS

ALPs arise by considering the Lagrangian of a complex scalar field ϕ with a $\mathbb{Z}_N$ symmetry. This means that the Lagrangian is invariant under the transformation $\phi \to e^{2\pi i k/N}\phi$, where k is an integer. Such Lagrangian can be written as

$$\mathcal{L} = |\partial_\mu \phi|^2 - V(\phi), \tag{5.1}$$

where any potential $V(\phi)$ that respects the $\mathbb{Z}_N$ symmetry can be used. In order to produce ALP domain wall solutions, we chose a potential with N distinct minima,

$$V(\phi) = \frac{\lambda}{S_0^{2N-4}} |2^{N/2}\phi^N + S_0^N|^2 , \tag{5.2}$$

where λ is dimensionless and S_0 has dimensions of energy [2]. Note that Eqs. (5.1) to (5.5) are expressed in natural units ($\hbar = c = 1$) as is common in the literature for theoretical calculations. The extracted observables are again later on expressed in SI units.

The axion field is obtained by reparameterizing the complex field ϕ in Eq. (5.1) in terms of the real fields S (Higgs) and a (axion) as

$$\phi = \frac{S}{\sqrt{2}} \exp(ia/S_0) . \tag{5.3}$$

The N distinct minima are obtained when the Higgs mode equals the vacuum expectation value $S \to S_0$, and the axion field has the values

$a = (2k+1)\pi S_0/N$ for integer k. The symmetry-breaking scale can be defined as $f_{SB} = S_0/N$. Reparameterizing the complex scalar field in Eq. (5.1) and setting the Higgs mode to the vacuum expectation value yields the following axion Lagrangian:

$$\mathcal{L}_a = \frac{1}{2}(\partial_\mu a)^2 - 2m_a^2 f_{SB}^2 \cos^2\left(\frac{a}{2f_{SB}}\right) , \tag{5.4}$$

where the axion mass is $m_a = NS_0\sqrt{2\lambda}$.

Solving the classical field equations, the ALP field in the region between two distinct domains with constant value of the field can be expressed as

$$a(x) = 2f_{SB} \arcsin\left[\tanh(m_a x)\right] . \tag{5.5}$$

The domains are considered static and the wall spans on the yz-plane, so that the variation in the field appears in the x-axis. The value of the axion field monotonically changes to reach the value of the adjacent domain with a shape similar to an arc-tangent function. The gradient of the field in the direction perpendicular to the domain wall plane is

$$\frac{da}{dx}(x) = \frac{2f_{SB}m_a}{\cosh(m_a x)} . \tag{5.6}$$

Such a function can be approximated by a Lorentzian lineshape. The thickness Δx of the domain wall can be defined by the full width at half maximum of the Lorentzian. We find that the thickness of a domain wall is given in terms of the ALP mass as

$$\Delta x \approx 2\sqrt{2}\frac{\hbar}{m_a c} . \tag{5.7}$$

This an the following quantities in this section are expressed in SI units.

Using the domain-wall solution [Eq. (5.5)] and integrating the energy density of the domain wall over x the surface tension can be obtained as (energy per unit area)

$$\sigma_{dw} = \frac{8}{\hbar^2} m_a f_{SB}^2 . \tag{5.8}$$

Assuming that all the dark matter is in form of domain walls, the average separation between domains $\bar{L}$ can be estimated. In the Milky Wall, the dark matter energy density can be approximated by $0.4\,\mathrm{GeV/cm^3}$[1]. Therefore, the energy density of domain walls is then assumed to be $\rho_{dw} \leqslant 0.4\,\mathrm{GeV/cm^3}$. Given the energy per unit area in a domain wall σ_{dw}, the average domain size is approximated by

$$\bar{L} \approx \frac{\sigma_{dw}}{\rho_{dw}} = \frac{8}{\hbar^2}\frac{m_a f_{SB}^2}{\rho_{dw}} . \tag{5.9}$$

The mass of the ALP m_a governs two important observables of the experiment, namely the thickness of the wall Δx, and the average size of the domains $\bar{L}$. The equations presented assume static domain walls.

---

[1] Note that this value has an statistical uncertainty of ~ 30 % [129].

5.2 LINEAR COUPLING BETWEEN THE SPINS AND THE AXION FIELD

GNOME is constituted by sensors primarily sensitive to couplings with proton spins. Such interaction is predicted by the coupling between the axion field gradient and the axial-vector current of a fermionic field. For a fermion field ψ, the interaction in natural units is given by

$$\begin{aligned}\mathcal{L}_{\text{int}} =& \frac{i(\phi\partial_\mu\phi^* - \partial_\mu\phi\phi^*)}{S_0 f_{\text{int}}}\bar{\psi}\gamma^\mu\gamma^5\psi \\ &\xrightarrow{S\to S_0} \frac{\partial_\mu a}{f_{\text{int}}}\bar{\psi}\gamma^\mu\gamma^5\psi\,. \end{aligned} \tag{5.10}$$

Here, only the linear coupling of the axion field with the axial-vector current is considered. Higher order couplings can also be considered as in the search for the stochastic properties of an ALP field [6]. However, a higher order suppression by the coupling constant appears.

The spin $\hat{\boldsymbol{S}}$ is related to the axial-vector current. Then the Hamiltonian of the interaction can be written as

$$H_{\text{int}} = \frac{-(\hbar c)^{3/2}}{f_{\text{int}}}\boldsymbol{\nabla} a \cdot \frac{\hat{\boldsymbol{S}}}{||S||}\,, \tag{5.11}$$

where $\hat{\boldsymbol{S}}$ represents the spins being considered which can be proton, neutron or electron.

Fundamentally, an optical magnetometer measures the Zeeman energy splitting in a particular hyperfine level due to a magnetic field. By including the interaction from Eq. (5.11) into the Hamiltonian of the atom, an additional non-magnetic energy shift is induced. Such shift is given by the expected value of H_{int}. Since the sensors are primarily sensitive to interactions with the valence proton, it is assumed that the exotic interaction just affects the proton spins. The energy shift can be written as

$$E_{\text{int}} = \frac{(\hbar c)^{3/2}}{f_{\text{int}}||S_p||}\langle\hat{\boldsymbol{S}}_p\rangle\boldsymbol{\nabla} a\,. \tag{5.12}$$

An optical magnetometer is sensitive to the total atomic angular momentum. By using Eq. (3.20), the effect on hyperfine levels can be approximated. At the point where the ALP field gradient is maximal, the energy shift is

$$E_{\text{int}} = \frac{\cos\theta_{dw}}{f_{\text{int}}||S_p||}\sigma_{p,F} m_F f_{SB} m_a\,, \tag{5.13}$$

where θ_{dw} is the angle between the total atomic angular momentum[2] and the direction of the ALP field gradient. For protons $||S_p|| = 1/2$. This energy shift feature the same structure as the one produced by the magnetic interaction with spins, $E_B = g_F \mu_B m_F B$. By asking what would be the magnetic field would produce the same effect as the

---

[2] In an atomic magnetometer the average direction of the atomic angular momentum defines the sensitive direction.

axion gradient, the normalized pseudo-magnetic field can be written as

$$\mathcal{B}_p = \frac{g_F^j B_j}{\sigma_{p,F}^j \cos\theta_{dw}^j} = \frac{4}{\mu_B} m_a \xi, \tag{5.14}$$

where B_j is the locally measured pseudo-magnetic field measured along the sensitive direction and $\xi \equiv f_{SB}/f_{int}$. The normalized pseudo-magnetic field, $\boldsymbol{\mathcal{B}}_p = \mathcal{B}_p \hat{\boldsymbol{n}}_{dw}$, is used to characterize a domain wall since it is independent on the atomic properties. This way the observation of a set of magnetic field B_j in the network can be related to the parameters of the axion field: m_a, f_{SB} and f_{int}. The dependence of B_j, g_F^j, $\sigma_{p,F}^j$, and θ_{dw}^j on the magnetometer is marked with the index j.

5.3 DOMAIN WALL DYNAMICS

In order for the domain walls to survive until today, they have to be stable in the galaxy and therefore feature some dynamics. To approximate these dynamics, the standard halo model [130], which describes cold particle dark matter trapped in a galaxy, is generalized to two dimensional objects. By knowing the velocity probability density function of domain walls, the expected encounter rate and crossing speed can be estimated. In order to estimate the probability of domain walls crossing Earth one should consider that faster domain walls will cross Earth more frequently than slower ones. As a result one obtains the event rate probability density function. By modeling the speed of domain walls and the incident angle, the duration of the encounters can estimated as well as the encounter rate.

Observations of the galactic rotation curves suggest that the visible matter in the galaxy is embedded in a much greater dark matter halo. Within the SHM, the density profile of this halo is obtained by considering a thermalized, self-gravitating, collisionless gas of particles. The distribution of velocities in the galactic reference frame is isotropic and feature a threshold at the galactic escape speed $v_e = 544\,\mathrm{km/s}$ above which no dark matter particles are bound. The probability density function for the velocity follows a three dimensional Gaussian in the galaxy reference frame as

$$f_{gal}^{(3)}(\boldsymbol{v}) = (2\pi s^2)^{-3/2} e^{-\frac{(\boldsymbol{\mu}_{gal}-\boldsymbol{v})^2}{2s^2}} \tag{5.15}$$

with expected velocity $\boldsymbol{\mu}_{gal} = 0$ and variance $s^2 = v_0^2/2$. The variance of the distribution is related to the galactic orbital speed v_0. At a distance from the galactic center similar to that of the sun $v_0 = 220\,\mathrm{km/s}$. The earth velocity among the galaxy can be approximated with the same value $v_L = v_0$ when ignoring the orbital speed. Earth velocity has an apparent direction towards the Cygnus constellation.

The SHM can be modified to include the fact that domain walls are two dimensional objects. An analytical expression for the probability density function for crossing between Earth and domain walls was presented in Ref. [131] and derived in detail in Ref. [128]. Here, I present a Monte Carlo numerical method to extract the parameters of interest from the distribution.

The main difference in the dynamics between particle dark matter and domain walls is that the later features internal structure. The orientation of the wall with respect its velocity can take any value. This extra degree of freedom is not observable. Only the velocity component normal to the plane of the wall can be measured by GNOME. However this alters the expected distribution of velocities observed on Earth.

Starting from the SHM at the galactic rest frame, a sample of random velocities can be generated as

$$\boldsymbol{v}_{\mathrm{gal}} \sim \mathcal{N}(0, v_0/\sqrt{2}), \tag{5.16}$$

where $\mathcal{N}$ denotes a random sample from a three dimensional Gaussian distribution. The z-axis is taken along the direction of movement of Earth $\boldsymbol{v}_{\mathrm{L}}$. Since particles traveling faster than v_e escape the galaxy, such velocities are discarded from the generated sample. By subtracting $\boldsymbol{v}_{\mathrm{L}}$, the velocity sample is moved to the Earth-centered inertial (ECI) frame $\boldsymbol{v}_{\mathrm{ECI}} = \boldsymbol{v}_{\mathrm{gal}} - \boldsymbol{v}_{\mathrm{L}}$.

The internal degree of freedom of domain walls is considered by assuming that $\hat{\boldsymbol{n}}_{\mathrm{dw}}$ and direction of movement are independent and take both random angles. This is taken into account by generating as many random directions in 4π solid angle from a flat distribution as velocities were generated. These directions are the normal to the wall $\hat{\boldsymbol{n}}_{\mathrm{dw}}$. By finding the dot product between $\hat{\boldsymbol{n}}_{\mathrm{dw}}$ and $\boldsymbol{v}_{\mathrm{ECI}}$, one finds the observable speed perpendicular to the domain wall $\boldsymbol{v}_{\perp}$. The relative angle between Earth's velocity and the domain wall is given by

$$\theta_{\mathrm{rel}} = \arccos[(\boldsymbol{v}_{\perp} \cdot \boldsymbol{v}_{\mathrm{L}})/(|\boldsymbol{v}_{\perp}||\boldsymbol{v}_{\mathrm{L}}|)]\,. \tag{5.17}$$

Using the generated velocities and performing the operation outlined, an approximation to the cumulative event probability distribution as a function of the crossing velocity is obtained, see Fig. 5.1a. The event probability density as a function of the perpendicular speed can be seen in Fig. 5.1b. Note that to obtain the event probability density, each sample is weighted by their perpendicular speed when calculating the histogram since the event probability is proportional to the speed.

The analysis method used is inefficient when searching for slow domain walls[3]. For this reason, we decided to consider a subset of the fastest velocities. We chose the range of velocities that gives us a confidence level on the possible domain wall dynamics of $\varepsilon_s = 97.5\,\%$ when just including the fastest domain walls. Figure 5.1a shows the domain wall dynamics that satisfy this condition as the leftmost contour line. All possible directions are included in order to reach the 97.5 % confidence level. Figure 5.1b shows the distribution of perpendicular speeds. If one considers all speeds above 47 km/s up to the escape speed the condition of $\varepsilon_s = 97.5\,\%$ is satisfied. The median and mean of the distribution are 235 km/s and 339 km/s

---

[3] The delay times between signals becomes increasingly sensitive to the direction $\hat{\boldsymbol{n}}_{\mathrm{dw}}$. Additionally, Earth rotation starts to play a role.

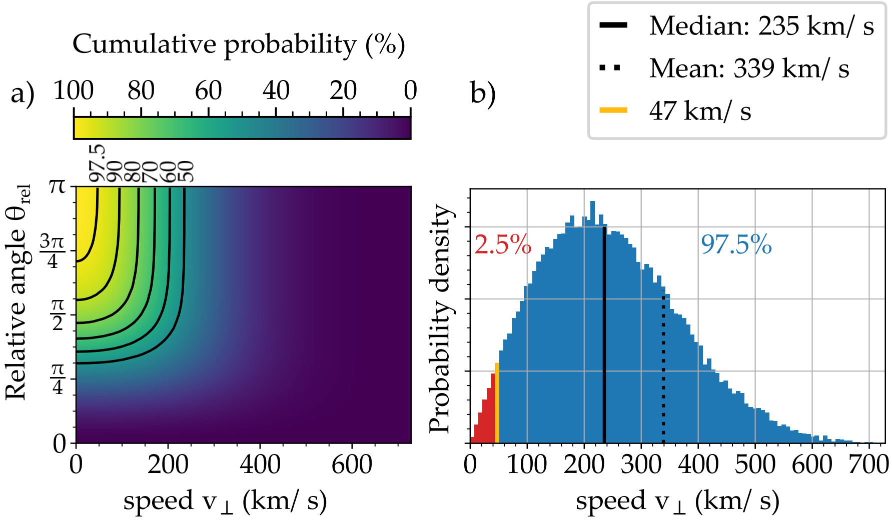

Figure 5.1: Probability distributions for domain wall crossings. a) Cumulative domain wall event probability: the integration is performed from ∞ to $v_\perp$ and from 0 to θ_{rel}. The contour lines indicate areas of constant cumulative probability. b) Event probability density of the perpendicular speed of a domain wall crossing earth integrated over the full 4π solid angle. The orange line marks the speed above which the confidence on the domain wall dynamics is $\varepsilon_s = 97.5\,\%$.

respectively. We chose the typical perpendicular domain wall speed to be $\bar{v} = 300\,\mathrm{km/s}$ comparable to other domain wall searches [131].

There are two factors which depend on the dynamics that must be considered when determining if ALP domain walls are observable by the network. These are the duration, and the rate of encounters. For a domain-wall velocity $\boldsymbol{v}_\perp$, the duration of a signal is

$$\Delta t = \Delta x / v_\perp . \tag{5.18}$$

Therefore, the duration is not only dependent on the parameters of the ALP but also on the dynamics. GNOME would be able to determine Δx since the crossing speed $v_\perp$ can be inferred by the delay between the signals.

If the domain walls could induce a strong enough signal to be observed, but are so infrequent that GNOME is unlike encounter them in the course of a measurement, then the network would be effectively insensitive to these. The expected average rate of domain walls passing through Earth can be estimated using the expected domain velocity as

$$r = \frac{\bar{v}}{\bar{L}} = \frac{\bar{v}\rho_{dw}}{8 m_a f_{SB}^2} . \tag{5.19}$$

5.4 RELATE GNOME OBSERVABLES TO ALP DOMAIN-WALL PARAMETER SPACE

The physical parameters describing the ALP domain walls (m_a, f_{SB}, and f_{int}) must be related to the parameters observable by the network ($\mathcal{B}_p$ and Δt).

Domain walls are assumed to randomly encounter Earth and these encounters are sparse. The number of crossings in a given time window can be described using Poison statistics. The probability of observing k events in a given time interval is

$$P(k;\mu) = \frac{\mu^k}{k!}e^{-\mu} \tag{5.20}$$

for a mean of μ events expected.

Additionally, GNOME has a detection efficiency $\epsilon < 1$ due to the noise in the sensors. The chance of identifying all domain walls given k crossings is $(1-\varepsilon_s\epsilon)^k$. For an event rate r and measurement time T, the probability that no events are detected is then

$$\sum_{k=0}^{\infty}(1-\varepsilon_s\epsilon)^k\frac{(rT)^k}{k!}e^{-rT} = e^{-\varepsilon_s\epsilon rT}\,. \tag{5.21}$$

If no events are found in the time interval T, a bound on the event rate, R_C, at confidence level C can be placed. This is then given by demanding that the probability of observing at least one event is $1-e^{-\varepsilon_s\epsilon R_C T} \geqslant C$. In other words, one would expect to observe event rates of

$$r \geqslant R_C \equiv \frac{-\log(1-C)}{\varepsilon_s\epsilon T}\,. \tag{5.22}$$

The physical parameter space of the ALPs is constrained by demanding that $r \geqslant R_C$. Similar arguments for defining constraints can be found, e.g., in Ref. [132]. The detection probability $\epsilon(\Delta t, \mathcal{B}_p', \zeta)$ is the probability of a domain wall of duration, Δt, and normalized pseudo-magnetic field, $\mathcal{B}_p$, producing a signal with a magnitude-to-uncertainty ratio above ζ[4]. These parameters are related to the physical parameters of ALPs via Eq. (5.7) and Eq. (5.14). One finds a sensitivity bound for f_{int} in terms of m_a and ξ to be

$$f_{int} \leqslant \frac{1}{\xi}\sqrt{\frac{-\bar{v}\rho_{dw}T}{8m_a\log(1-C)}\varepsilon_s\epsilon\left(\Delta t, \mathcal{B}_p, \zeta\right)} \tag{5.23}$$

$$\text{for}\quad \Delta t = \frac{2\sqrt{2}}{\bar{v}m_a} \quad\text{and}\quad \mathcal{B}_p = \frac{4m_a\xi}{\mu_B}.$$

---

[4] During the analysis it is convenient to express the relevance of a signal in terms of the magnitude-to-uncertainty ratio. The analysis procedure fits a domain wall to the GNOME data. The magnitude-to-uncertainty ratio is the value of the fitted normalized pseudo-magnetic field over the uncertainty in the fit (see Chapter 6).

6

DATA ANALYSIS PROCEDURE

The main part of this thesis is the conception and implementation of a data analysis procedure to search for domain walls in the GNOME data. This chapter discusses the details of this analysis as well as the calibration of their parameters. Parts of this chapter are adapted from Refs. [36] and [3].

The analysis procedure is composed of three stages designed to select candidate domain-wall events. First, in the pre-processing stage (see Sec. 6.1), the raw data are rolling averaged and filtered. This enhances the signal-to-noise ratio of a domain-wall signal in a magnetometer for a certain range of parameters. This operation also considerably reduces the amount of data to be processed. Additionally, in this stage the noise in the data is estimated. Finally, the data is structured in uniform segments of data with fixed duration.

Second, in the velocity-scanning stage (see Sec. 6.2), the data and corresponding noise from each magnetometer are time-shifted according to a range of possible domain-wall velocities. For each velocity and time, the set of network measurements are expressed in terms of the domain-wall-crossing model. That is the domain wall direction and magnitude that could most likely reproduce the data as well as a p-value quantifying the agreement with the model.

Third, in the post-selection stage (see Sec. 6.3) the consistency of the fitted domain wall is checked. Conditions are applied to the relative angle between the scanning velocity and the fitted domain-wall direction as well as to the obtained p-value. These conditions are set based on a false-negatives and false-positives study. These characterize the detection probability for a domain wall present in the data, and the probability of noise faking a signal, respectively. The magnitude-to-uncertainty ratio of the fitted domain wall that passed the consistency is given as output. The magnitude is the estimated normalized pseudo-magnetic field produced by the domain wall and the uncertainty corresponds to the noise of the data propagated to this parameter. If there is an excess of events passing the consistency with respect to the background. Then a detection can be claimed. The background is estimated by applying the same algorithm to background data. This set of data is created by randomly shuffling the time of the different station to make sure that no real domain-wall crossing is present. A flowchart describing the procedure can be seen in Fig. 6.1.

6.1 PRE-PROCESSING

Before searching the data for domain walls, subsequent pre-processing steps are applied to the data: namely averaging, baseline removal, filtering and noise estimation. The data are processed in segments of

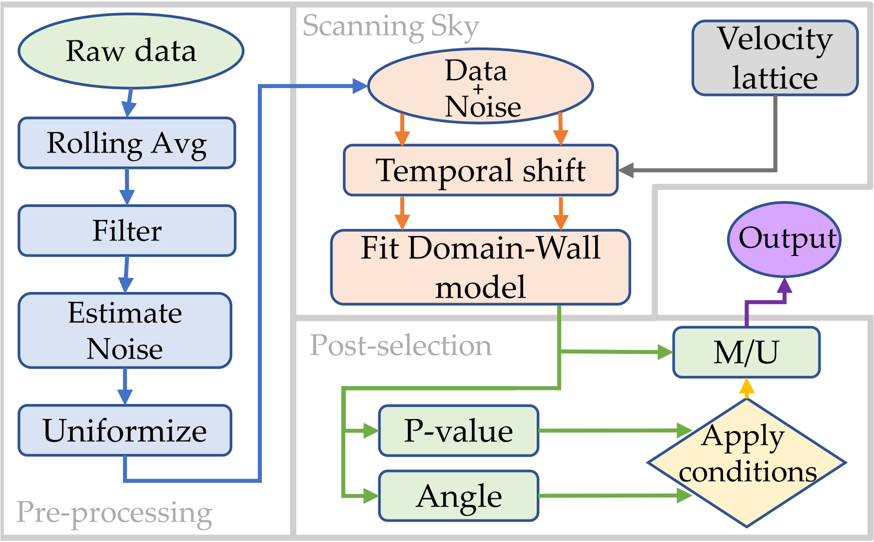

Figure 6.1: Summary of the steps performed to analyze the GNOME data to search for ALP domain wall crossings.

400 minutes. The pre-processing stage aims to optimize the amount of data to be processed, remove noisy frequency bands and offsets, and estimate the uncertainty in the data points. For the later analysis it is important that the data do not contain any systematic offset.

First, a rolling average with a 20 s time constant is applied to the data. This way the amount of information is reduced but the time accuracy is maintained. In a later stage the data are down-sampled to 0.1 Samples/s resulting in overlapping bins. To reduce edge effects when applying filters, the constant and linear trends in the data are removed. Noisy frequency bands are suppressed by applying a first-order Butterworth high-pass filter at 1.67 mHz together with the notch filters corresponding to 50 Hz and 60 Hz power line frequencies with a quality factor of 60. These filters are applied forward and backward to remove phase effects.

The accurate estimation of the significance of a signal depends on the correct evaluation of the noise around that signal. Since the data have been rolling averaged, only one point each 20 s contains independent information. Only these points are considered to estimate the noise. The standard deviation is calculated using 100 points around each point. Frequently, samples featuring a large deviation from the mean can be found in the data. These are not part of the stochastic noise but possible signals or glitches of unknown origin. These can considerably bias the estimation of the local noise. An iterative process is employed to ignore such points when estimating the noise around each binned point.

The iterative process starts with the calculation of the standard deviation of the entire segment. Assuming Gaussian statistics, a threshold amplitude above which only 0.1 points are expected in the segment is calculated based on this standard deviation. The points above that amplitude are flagged. Second, the standard deviation in the segment is calculated again ignoring the flagged points. The threshold amplitude is newly calculated and points are flagged. The process is repeated until the ratio between the previous and current standard deviation is less than one. Then 100 points around each point are used to assign a standard deviation, s_σ. This ignores the flagged data during the previous step. Finally the last standard deviation obtained for the whole segment is assigned to the flagged points.

Instances in which the data is flagged as unreliable by the sanity monitor or in which the data is not existent produce discontinuous segments. An heterogeneous data structure irregular segments hinders the efficient processing. It is cumbersome to search the segments to check which magnetometers are contributing to the measurement at a given time. This is solved by filling up the data gaps with values which can be easily ignored in the analysis thereby maintaining continuous and regular data segments. When the data is insane or unavailable the magnetic field is given a value of zero and a noise value of one. Unavailable data is then flagged as insane. This way the data has a predictable and uniform structure. Moreover, the instances in which data are unavailable or insane do not contribute to the further analysis. Continuous segments are particularly important when using python since its numerical package numpy is optimized for matrix operations and benefits from calculating in bulk.

An example of the result of pre-processing can be seen in Fig. 6.2. One can see that the dispersion in the measurement is greatly reduced and the data is centered at zero magnetic field. Regions with unreliable data are given a value of zero, noise value of one and are marked as insane.

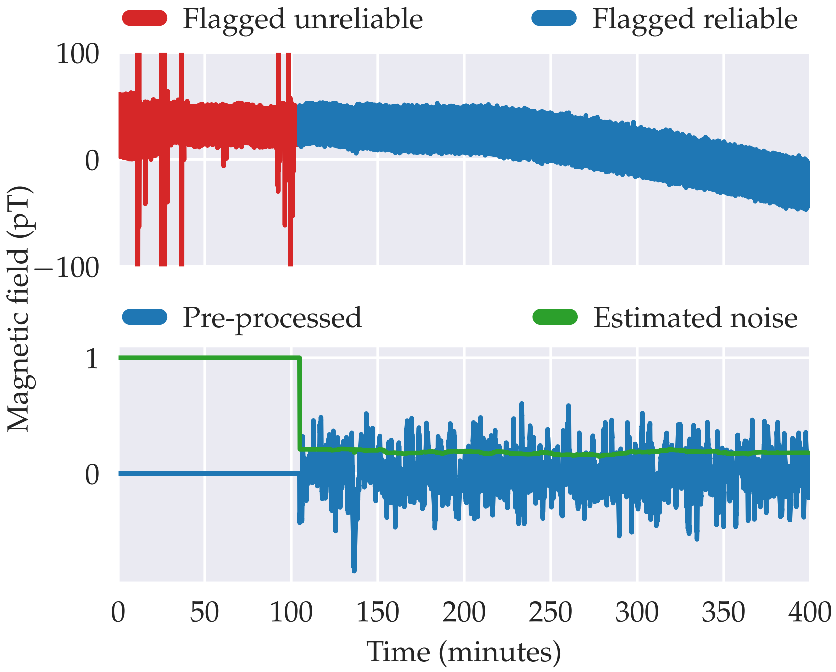

Figure 6.2: Fragment of magnetic field data before and after pre-processing. Above: raw magnetic field measurement from a single magnetometer during Science Run 2. Below: magnetic field measurement and noise estimation after applying the pre-processing steps.

6.2 SCANNING VELOCITIES

A domain-wall can cross Earth at any direction, and any relative speed between zero and the galaxy escape speed as discussed in Sec. 5.3. The velocity perpendicular to the domain wall plane determines the arrival time at different magnetometers. In addition the angle between $\boldsymbol{v}_\perp$ and the sensitive axes determines the relative signal amplitudes. Signals originated by a single domain wall are detected seconds apart by different sensors. The time delay can be expressed as

$$\Delta t_j = (\boldsymbol{x}_j - \boldsymbol{x}_0) \cdot \frac{\boldsymbol{v}_\perp}{\|\boldsymbol{v}_\perp\|^2}, \tag{6.1}$$

where $\boldsymbol{x}_j$ are the Cartesian coordinated of a sensor and $\boldsymbol{x}_0$ is a reference position which we choose to be the center of Earth. Systematically shifting the time series of each sensor with one another to find the matching delays can be time-consuming. Additionally, such operation does not scale favorably with the number of sensors. In order to avoid such a blind search for the right set of delays, a set of encounter velocities is chosen in advance based on the SHM (see. Fig. 5.1).

6.2.1 *The scanning lattice*

Assuming the SHM, the probability distribution of domain-wall velocities can be predicted (see Sec. 5.3). Ranges in $v_\perp$ and θ_{rel} are selected to consider 97.5 % of the crossing parameters. As seen in Fig. 5.1 one needs to scan $v_\perp$ from 47 to 770 km/s, and θ_{rel} from 0 to π to guarantee a 97.5 % coverage. The range in θ_{rel} means that the directions, $\hat{\boldsymbol{n}}_{\text{scan}}$, have to be scan over the full 4π solid angle.

The range of speeds and directions is discretized in order to scan it. The scanning step size is estimated by considering two antipodal magnetometers. From Eq. (6.1) the changes in the delay time with respect to variation in the speed can be estimated. Note that the delay is also dependent on the considered direction. In order to give an upper bound, the crossing direction is fixed to maximize variation of the delay. For the speed, this is accomplished if a domain wall is parallel to the line joining the two antipodal magnetometers. For the angle, this is accomplished if a domain wall is perpendicular to the line joining the two antipodal magnetometers. The upper bound on the change in the delay is required to be smaller than half the bin size, $T_{\text{avg}}/2 = 10\,\text{s}$. This assures that the signal remains in the same bin for adjacent scanning velocities.

The speed range is scanned in steps of

$$\delta v \leqslant \frac{T_{\text{avg}} v_\perp^2}{4 R_\oplus}, \tag{6.2}$$

where $R_\oplus$ is the radius of the Earth. The array of speeds is generated iteratively. It starts with the lowest speed, 47 km/s and continues adding the updated step until the escape speed is reached. This way an array of k perpendicular speeds is obtained. Each element of the array is denoted by $v_\perp^k$.

A similar procedure can be followed to establish a scanning step for the directions. This is estimated in terms of the angle between adjacent scanning directions. Such angle step is given by

$$\delta\theta \leqslant \frac{T_{\text{avg}} v}{4R_{\oplus}} \,. \tag{6.3}$$

In order to generate the array of directions we consider a sphere. A direction can be constructed by a vector pointing from the center of the sphere to a point on the surface. The scanning directions can be generated by a lattice of points on the surface so that a point always exists within every circle whose diameter spans an arc of $\delta\theta$. Each element of the array is denoted by $\hat{\boldsymbol{n}}^{kl}_{\text{scan}}$, where l indexes the directions for the k^{th} speed. A roughly even distribution of points on the surface is generated using the Fibonacci lattice method (see, e.g., Ref. [133] for a description of the method and Ref. [128] for the implementation in the GNOME case).

The Fibonacci lattice method is a means of generating a sequence of points that uniformly covers a surface. This way the lattice for each speed is created while assuring that they are separated by an angle $< \delta\theta_{\text{rel}}$. The array of l scan directions $\hat{\boldsymbol{n}}^{kl}_{\text{scan}}$ for each $v^k_{\perp}$ is expressed in spherical coordinates. The Polar angle is defined with respect to the z-axis and the azimuthal angle is defined relative to the x-axis (using right-handed coordinate system). A scan over a hemisphere is possible if the polar angles are constrained to be $< \pi/2$.

6.2.2 *Temporal shift*

After the pre-processing stage, the data are time-shifted according to each $v^k_{\perp}$ and $\hat{\boldsymbol{n}}^{kl}_{\text{scan}}$, such that a domain-wall crossing would be observed at all magnetometers simultaneously. In case of a crossing, signals appear in the network in a predictable pattern given by a plane with constant velocity crossing Earth.

Earth travels among the center galaxy at an apparent velocity towards the Cygnus constellation. Deneb is the brightest star in this constellation. Due to this relative movement, domain walls are expected to most probably cross Earth from that direction. The geocentric coordinates of Deneb are calculated at a time corresponding to the midpoint of the time-series using the python astropy package. Such vector is defined as the z-axis for the scanning directions. The direction towards Deneb is rotated according to the spherical coordinates of $\hat{\boldsymbol{n}}^{kl}_{\text{scan}}$ to reproduce all scanning directions. These vectors are again rotated to simulate the daily rotation of Earth. This generates the scanning directions in geocentric coordinates for each down-sampled data point (with period $T_{\text{avg}}/2$). This method assures that Deneb is located along the z-axis independent of Earth rotation. This allowed to scan a hemisphere around Deneb at each time. Ninety-five percent of domain walls are expected to have perpendicular velocities opposite to Earth's movement relative to the galactic rest frame [134]. However, the necessity to cover 97.5% of the domain-wall dynamics required the scan of all directions. Although it was not anymore relevant to

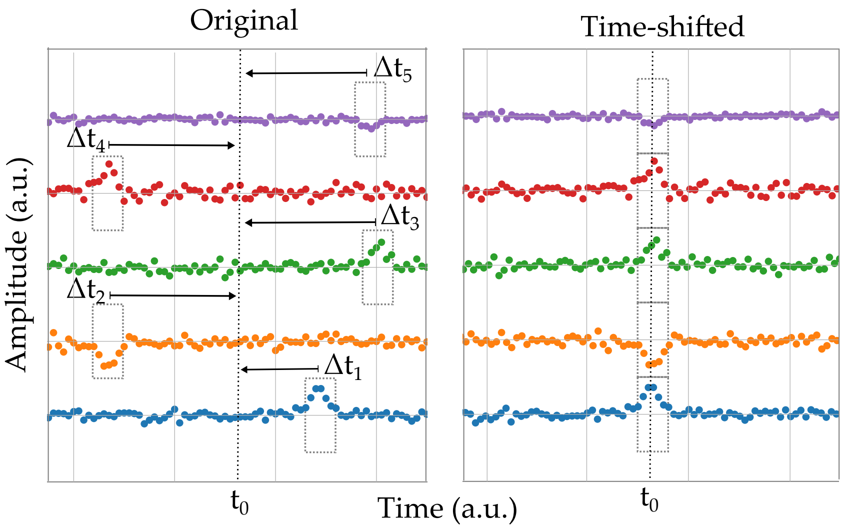

Figure 6.3: Visualization of the time shifting operation. A domain wall produces signal at different times at each sensor. The time is shifted so that all signal appear at t_0. This is the time at which the domain wall reaches the center of Earth.

scan around Deneb this feature was kept unchanged. The speed of the code could be improved by using a fix array of direction since the location of Deneb is irrelevant if a 4π solid angle is scanned.

One can use Eq. (6.1) to calculate the time delay between the crossing with Earth center and each magnetometer, Δt_{tj}^{kl}. The delays Δt_{tj}^{kl} are calculated for the down-sampled data (with period $T_{avg}/2$). However, the delayed measurements are extracted from the rolling averaged data from each magnetometer. This allows greater accuracy on selecting the domain wall signal peak from each magnetometer since the data is extracted from a time-series at the original sampling rate 512 Samples/s. Therefore, the calculated delay is not limited by the down-sampled resolution. After this operation, an aligned set of measurements calculated with overlapping averaged windows is obtained. A graphical representation of the time shifting operation can be seen in Fig. 6.3. The temporal shift operation greatly increases the amount of data to be processed. The data for each time-shift is considered independent. Preprocessed data provides a point for each down-sampled time and magnetometer, denoted as s_{tj}. However, after time shifting, each delay creates independent points. As a result, an array s_{tj}^{kl} is obtained. An agreement with a domain wall crossing is searched comparing the data from all magnetometers (j index) for each time (t index) and velocity (k and l indexes).

6.3 FIT AMPLITUDES TO THE DOMAIN-WALL MODEL

After time-shifting the data, one obtains a measurement time-series s_{tj}^{kl} and the corresponding noise estimation $(s_\sigma)_{tj}^{kl}$ at every time and velocity for all active sensors. To check the agreement with a domain wall crossing, the same operation is applied for each time and velocity.

The notation is simplified to $\boldsymbol{s}$ ($\boldsymbol{s}_\sigma$), a vector whose components are the values (standard deviations) measured at each magnetometer for the same time, and scanning velocity.

The signal expected by a domain-wall crossing in the network is given by $\boldsymbol{\mu} \equiv \mathrm{D}\boldsymbol{m}$, where $\boldsymbol{m}$ describes the normalized pseudo-magnetic field associated with the domain-wall-crossing event as $\boldsymbol{m} = \mathcal{B}_\mathrm{p}\hat{\boldsymbol{n}}_{\mathrm{dw}}$. The matrix D contains the directional sensitivities of the magnetometers. The components of $\boldsymbol{\mu}$ describe the pseudo-magnetic field expected at each magnetometer $\mu_j = B_j$. To simplify the equations, the response factor of each sensor to the ALP field is set to one. These are later included by multiplying the corresponding row in D by the appropriate response factor (see. Table 4.3). In order to estimate the parameters of the domain-wall crossing, one finds the $\boldsymbol{m}$ that is expected to produce a the pseudo-magnetic field $\boldsymbol{\mu}$ most closely to $\boldsymbol{s}$. The agreement between $\boldsymbol{\mu}$ and $\boldsymbol{s}$ is quantified with the p-value.

The parameter estimation of the domain-wall is performed for a given scanning velocity. However, the fitted incoming direction of the domain wall is allowed to be different than the corresponding scanning velocity. The angle difference between scanning and domain wall directions provides an additional parameter to quantify the agreement. These two directions are expected to be parallel if a domain wall crossed GNOME. The angle difference is defined as

$$\theta_{\mathrm{diff}} = \arccos(\hat{\boldsymbol{n}}_{\mathrm{dw}} \cdot \hat{\boldsymbol{n}}_{\mathrm{scan}})\,. \tag{6.4}$$

The amplitudes from the n sensors $\{s_j\}$ (for $j = 1, \ldots, n$) obey a linear equation with the sensor's sensitive axes given by $\{\hat{\mathbf{n}}_j\}$:

$$\mathrm{D}\boldsymbol{m} = \boldsymbol{s} \quad \text{for } \mathrm{D} \equiv \begin{bmatrix} \hat{\boldsymbol{n}}_1^{\mathrm{T}} \\ \hat{\boldsymbol{n}}_2^{\mathrm{T}} \\ \vdots \\ \hat{\boldsymbol{n}}_n^{\mathrm{T}} \end{bmatrix}, \ \boldsymbol{s} \equiv \begin{bmatrix} s_1 \\ s_2 \\ \vdots \\ s_n \end{bmatrix}, \tag{6.5}$$

The best estimate for the normalized pseudo-magnetic field given a measured set of values $\boldsymbol{s}$ is found by solving Eq. (6.5) as a least-squares minimization problem. The χ^2 value to minimize is given by

$$\chi^2 = (\mathrm{D}\boldsymbol{m} - \boldsymbol{s})^{\mathrm{T}} \Sigma_s^{-1} (\mathrm{D}\boldsymbol{m} - \boldsymbol{s})\,, \tag{6.6}$$

where Σ_s is the covariance matrix of the measurement. The covariance matrix is a diagonal matrix whose values are the square of the standard deviation calculated in the pre-processing stage $\boldsymbol{s}_\sigma$ (see Sec. 6.1). An analytical expression can be found for the minimum of χ^2 as

$$\boldsymbol{m} = \Sigma_m \mathrm{D}^{\mathrm{T}} \Sigma_s^{-1} \boldsymbol{s} \quad \text{for} \quad \Sigma_m = (\mathrm{D}^{\mathrm{T}} \Sigma_s^{-1} \mathrm{D})^{-1}\,, \tag{6.7}$$

where Σ_m is the covariance matrix for the inferred domain-wall crossing. Details on the derivation of this analytical expression can be found in Ref. [128].

A maximum on the norm of $\boldsymbol{m}$ is expected at the insertion time when the scanned velocity corresponds to the domain-wall-crossing

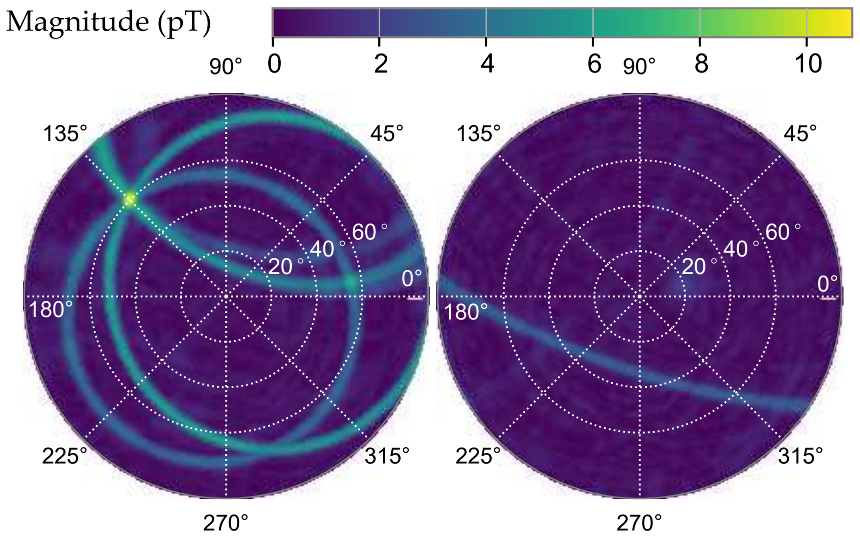

Figure 6.4: Visualization of the lattice scanning for a fixed speed and time. A simulated domain wall is inserted in a time-series with Gaussian background. The direction of the simulated $\mathcal{B}_p\hat{\boldsymbol{n}}_{dw}$ is taken to be 60° polar and 135° azimuth angle with respect to Deneb's direction with a magnitude of 20 pT. The amplitudes at each sensors are given by Eq. (6.5) and the delays by Eq. (6.1). The figures show the magnitude of $\boldsymbol{m}$ when scanning over a single hemisphere centered at Deneb. Left: The maximum magnitude is found at the insertion direction. Right: The delay times of the signals at the different sensors is randomized. Therefore no maximum point is found.

velocity, as can be seen in Fig. 6.4. The figure shows the norm of $\boldsymbol{m}$ for different directions at the insertion time and speed. The origin of the arcs in Fig. 6.4 has not been studied in detail. It could be originated by some magnetometers featuring a strong signal. An arc could be the set of angles which produces a delay for a magnetometer (or a subset of them) coinciding which the expected time. However, as shown later (see Fig. 6.5), the agreement of the reconstructed signal at the arc's angles with the crossing model is poor. The maximum is found at the direction of the insertion (60°,135°) where the corresponding delay coincides with the inserted time for all magnetometers. Therefore, after performing the velocity lattice scan, only the $\boldsymbol{m}$ corresponding to the velocity $(v_\perp^k, \hat{\boldsymbol{n}}_{\text{scan}}^{kl})$ producing the greatest magnitude is considered for further analysis at each down-sampled time.

An important statistical result from the estimation of $\boldsymbol{m}$ is the χ^2 value [see Eq. (6.6)], which describes the deviation between a measurement and expected signal pattern. Assuming that the noise in the measurements is normally distributed, the χ^2 values are distributed according to the number of degrees of freedom $(\dim(\boldsymbol{s}) - \dim(\boldsymbol{m}) = n - 3)$, where n is the number of active magnetometers. The p-value is given by the integrated right tail of this distribution starting from the measured χ^2. The p-value corresponds to the probability that the residual between the expected and measured values can be explained by deviations due to Gaussian noise. A small p-value indicates that the measurement cannot be explain by a domain wall and Gaussian noise.

The search algorithm outputs a most likely $\boldsymbol{m}$ and Σ_{m} together with a p-value for each down-sampled time. Three quantities are used to characterize the possible domain wall crossing. These are: the magnitude-to-uncertainty ratio $\zeta = |\boldsymbol{m}|^2/\sqrt{\boldsymbol{m}^{\intercal}\Sigma_{\mathrm{m}}^{-1}\boldsymbol{m}}$, the angle θ_{diff}, and the p-value.

6.4 POST-SELECTION

Measurement vectors $\boldsymbol{s}$ consistent with domain-wall crossings must be distinguished from signals originated by noise or systematic effects. This identification is accomplished by imposing thresholds on the p-value and θ_{diff}. The magnitude-to-uncertainty ratio ζ of the remaining events is compared to magnitude-to-uncertainty ratio of the events in the background. This allows to quantify the significance of the remaining events.

The p-value is a powerful tool for rejecting large signals not related to domain walls, as can be seen in Fig. 6.5. The p-value is given by the integrated right tail of the χ^2 distribution starting at the value given by Eq. (6.6). The p-value quantifies the probability that the residual between the expected and measured values can be explained by deviations due to Gaussian noise. A signal set agreeing with the model plus Gaussian white noise produces a flat distribution of p-values from 0 to 1. This property allows a one-to-one correspondence between a p-value threshold and probability of detection. For example, allowing p-values> 0.05 means that 95 % of the crossings will be accepted. In contrast, large signals which do not agree with the crossing model feature a skewed p-value distribution towards small p-values. This is the case because the χ^2 value tends to be large for signals not agreeing with the model. Therefore, discarding low p-values, is expected to reject spurious peaks while retaining a high probability of detection to domain walls. However, the sensors feature non-Gaussian noise. This affects the distribution of p-values. Therefore, the correspondence between p-value and probability of detection has to be explicitly calculated.

The direction $\hat{\boldsymbol{n}}_{\mathrm{dw}}$ is reconstructed independent of the scanning velocity, $\hat{\boldsymbol{n}}_{\mathrm{scan}}$. Therefore, the agreement between the scanned and estimated directions must be checked. Since the scanning lattice angular spacing depends on the speed, a normalized quantity is used to characterize the angular difference. The normalized angular difference is defined as $\theta_{\mathrm{diff}}/\delta\theta$, where $\delta\theta$ in Eq. (6.3) depends on the speed.

6.4.1 *Detection probability*

Finding the adequate thresholds for p-value and $\theta_{\mathrm{diff}}/\delta\theta$ is complex. The thresholds do not only optimize the number of events originated by the noise but also affect the probability of detection. Their calibration is set to reject the most noise but guaranteeing a minimum probability of detection of 97.5 % for events exhibiting a magnitude-to-uncertainty ratio $\zeta > 5$.

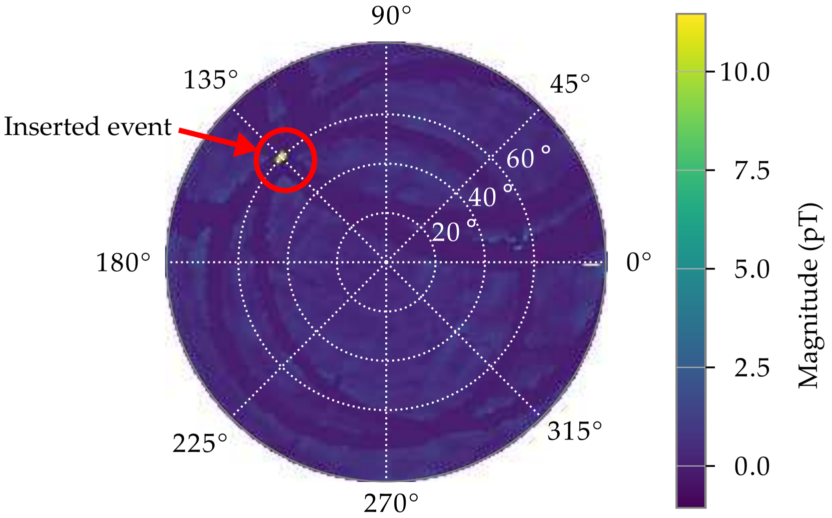

Figure 6.5: Visualization of the effect of applying a p-value threshold. In contrast to Fig. 6.4, directions producing a large magnitude but differing from the inserted direction are eliminated since these feature small p-values.

The evaluation of the detection probability of the search algorithm requires a well-characterized dataset that includes domain-wall-crossing signals with known properties. For this purpose, a background dataset is generated by randomly time-shuffling the search data so that the relative timing of measurements from different GNOME stations is shifted by amounts so large that no true-positive events could occur. By repeating the process of time shuffling, the length of the background data can be made to far exceed the search data. This method is used to generate background data with noise characteristics closely reproducing those of the search data [135]. A domain wall is inserted into the background data to create the test data.

Multiple 400 minute test datasets are created, each featuring a domain-wall-signal pattern with random parameters. The domain-crossing events have $\mathcal{B}_p$ randomly selected between 0.1 pT and 10^4 pT and Δt randomly selected between 10^{-2} s and $2 \cdot 10^3$ s. The distributions of these randomized parameters are chosen to be flat on a logarithmic scale. Additionally, the signals are inserted at random times with random directions $\hat{\boldsymbol{n}}_{\text{dw}}$. In order to simulate calibration error effects, the pulse amplitudes B_j inserted in each magnetometer are weighted by a random factor reflecting the uncertainties listed in Table 4.2. The crossing speed is also randomized within 47 km/s up to the galactic escape speed (see Fig. 5.1). The analysis algorithm is applied to each 400 minute test dataset. The characteristics of the event at down-sampled time closest to the insertion time are extracted. Only that point is used to characterize the detection probability.

Figure 6.6a shows the detection probability as a function of the threshold on the lower-limit of the p-value and the threshold on the upper-limit of the normalized angular difference. The detection probability is calculated as the ratio between the inserted events surpassing the thresholds and the total number of segments. The results showed in Fig. 6.6a are restricted to events inserted with a magnitude-to-uncertainty ratio between 5 and 10. The consideration of magnitude-to-uncertainty ratio events above 5 is intended to limit the possibility of evaluating background events instead of the inserted domain wall event. Considering only Gaussian noise, the background event probability above $\zeta = 5$ is below $10^{-4}\,\%$. Since the detection probability increases with the signal magnitude, we focus on the events below $\zeta = 10$. In total 46261 test data segments were analyzed. The black line marks the numerically evaluated boundary of the area guaranteeing at least $\epsilon > 97.5\,\%$ detection probability.

Figure 6.6b shows the false-positive probability. An amount of $T_b = 10.7$ years of background data are analyzed. The false-positive probability is given by the fraction of events surpassing the thresholds (p-value, $\theta_{dw}/\delta\theta$) with respect to total number of events featuring $\zeta > 5$. The black line marks the same path as Fig. 6.6a. Ideally, one would like to minimize the number of false-positives keeping a 97.5 % detection probability. All points along the black line will yield the desired detection probability, so the particular choice is made to minimize the false-positive probability. These values are p-value> 0.001 and $\theta_{diff}/\delta\theta < 3.5$ (represented as a white dot in both figures). The false-positive probability at this point is 13 %.

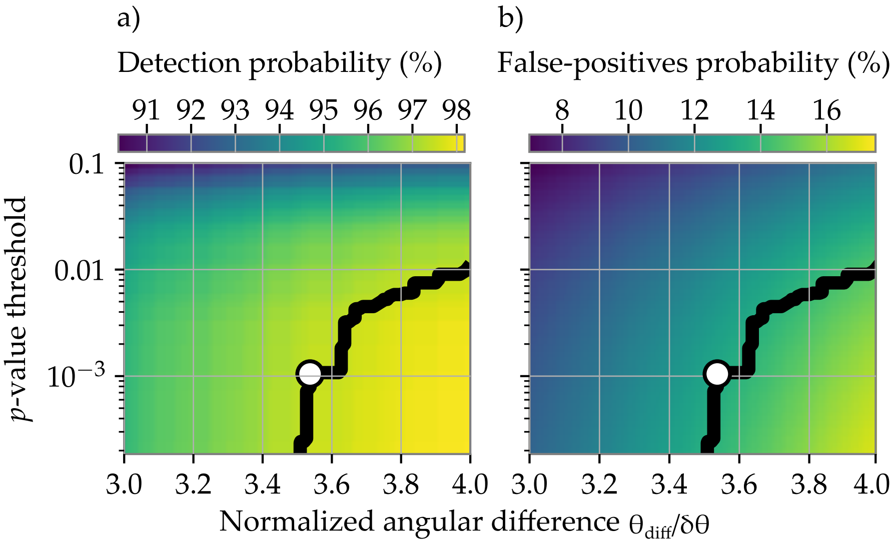

Figure 6.6: Optimization of the detection thresholds. a) Shows the cumulative detection probability as a function of the thresholds. The black line indicates the boundary to 97.5 % detection probability while the white dot shows the optimal thresholds. b) Shows the cumulative false-positives probability as a function of the thresholds. The black line shows the same path as a). The optimal thresholds are contained in the black line and minimize the false-positives probability.

After fixing the detection thresholds, the sensitivity of GNOME to domain walls can be evaluated. Figure 6.7 shows the detection probability for inserted domain walls producing a magnitude-to-uncertainty ratio of at least a five. This probability was numerically evaluated by analyzing the test data for subsections of the parameter space. The black line limits the region featuring a detection probability $\epsilon > 97.5\,\%$.

The sensitivity can also be theoretically evaluated from the characteristic noise of each station. The effects of pre-processing steps on the signal are carefully studied in Appendix A in Ref. [36]. Given the configuration of the network, the $\mathcal{B}_p$ producing a magnitude-to-uncertainty ratio of five at the worse direction can be calculated. Such estimation assumes an ideal behavior of the network in which all the magnetometers are active and feature the mean noise. This estimation on the characteristics of the domain wall producing a $\zeta \geqslant 5$ is shown by the white curve in Fig. 6.7.

One can see that the theoretical estimation greatly differs from the 97.5% detection probability line. This is due to the fact that not all magnetometers are consistently active and that the noise level can differ from the average level. When fewer magnetometers are active the uncertainty on the determination of $\boldsymbol{m}$ grows and the magnitude-to-uncertainty ratio degrade. The same event detected by fewer station produces a smaller magnitude-to-uncertainty ratio. Note that Fig. 6.6a just considers events with measured $\zeta \geqslant 5$. Additionally, noise in the sensors can distort the amplitude pattern and degrade the p-value estimation.

The characteristic shape of the sensitive region is a result of the filtering and averaging of the raw data. Averaging reduces the sensitivity of the search data to short pulse durations. The amplitude of a Lorentzian signals is linearly attenuated as the duration decreases. The high-pass filtering suppresses sensitivity for long Δt. The amplitude of a Lorentzian signal decreases exponentially with increasing duration [128]. The detection probability $\epsilon(\mathcal{B}_p, \Delta t, \zeta)$, is used to assess the sensitivity of the network to the parameter space of ALP domain walls.

6.4.2 *Background characterization*

Since the noise has a nonzero probability of mimicking the signal pattern expected from an ALP domain-wall crossing well enough to pass the p-value and directional consistency tests, the background-only data is also searched. This allows to quantify the significance of a signal observed in the search data.

The analysis algorithm is applied to $T_b = 10.7\,\text{years}$ of time-shuffled data in order to establish the rate of events expected solely from background. A large amount of background data are analyzed in order to characterize the number of rare high magnitude-to-uncertainty ratio events. The probability of finding one or more events in the search data above ζ from background is [136]

$$P(\geqslant 1 \text{ above } \zeta) = 1 - \exp\left(-\frac{T}{T_b}\left[1 + n_b(\zeta)\right]\right). \tag{6.8}$$

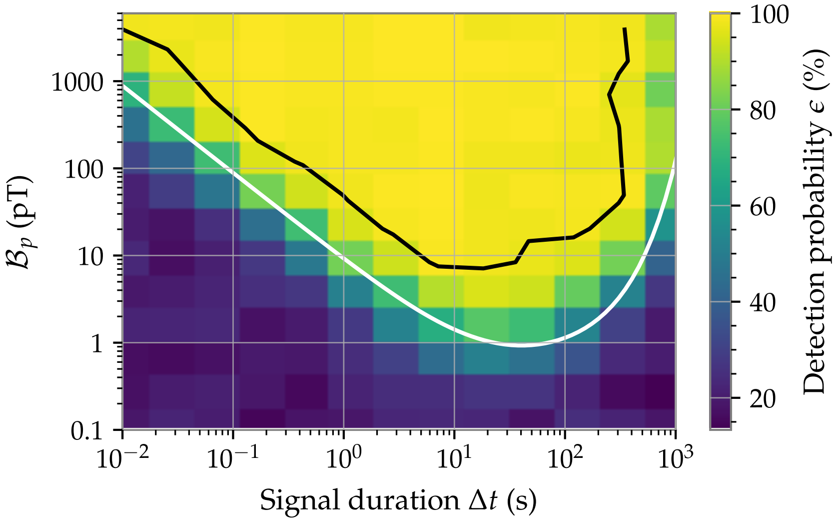

Figure 6.7: Detection probability for $\zeta > 5$ as a function of the domain wall parameters: magnitude and signal duration. The white line indicates the estimated $\mathcal{B}_p$ and Δt above which a domain wall produces a $\zeta = 5$ assuming all sensors are active, and feature their mean Gaussian noise level. The black line shows a bound above which the detection probability is greater than 97.5 %.

The duration of Science Run 2 was $T = 23$ days, and $n_b(\zeta)$ is the number of candidate events found in the background data above ζ. The statistical significance for finding a single event is then defined as

$$S = -\sqrt{2}\,\mathrm{erf}^{-1}\left[1 - 2(1 - P)\right], \tag{6.9}$$

where erf^{-1} is the inverse error function. The significance is given in units of the Gaussian standard deviation. The probability P denotes the probability of the random variable taking a value above $S\sigma$, where σ here is the standard deviation of the Gaussian.

Figure 6.8 shows the background number of counts at different magnitude-to-uncertainty ratios. The significance for finding one event given the background counts is given in the upper axis of the plot. One can see that the GNOME background is strongly non-Gaussian.

The limiting case of the magnetometers featuring pure Gaussian noise is given by the red dashed line. To construct this line, it is assumed that the components of $\boldsymbol{m}$ are Gaussian distributed. Then the magnitude-to-uncertainty ratio follows a χ distribution. Considering such a distribution and the number of data points measured one can estimate the number of events expected in function of the magnitude-to-uncertainty ratio. The number of events expected from Gaussian noise decays much faster than for the experimentally observed noise in GNOME as a function of magnitude-to-uncertainty ratio. However, note that it is still highly likely to find an event featuring a magnitude-to-uncertainty ratio of 5 originating from pure Gaussian noise.

The significance of finding one or more events is never higher than three sigma for the whole range of ζ presented in Fig. 6.8. A significance higher than three is typically a hint to an interesting event. The analysis of Science Run 2 would not have been able to

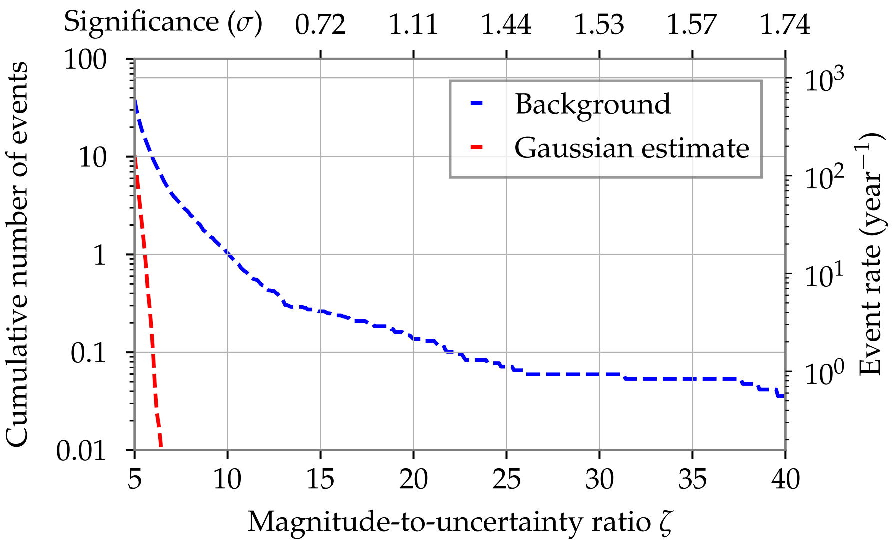

Figure 6.8: Evaluation of the background events for 10.7 years of time-shuffled data. The blue line shows the cumulative number of events normalized to the duration of Science Run 2 featured in background data. The red line shows the expected number of event if the data would solely contain Gaussian noise.

identify a discovery up to a magnitude-to-uncertainty ratio of 40. More background data is needed to investigate the expected rate at higher magnitude-to-uncertainty ratios. In order to lower the event background, more emphasis has to be taken on improving the noise characteristics of the network. Event if a detection cannot be claimed up to a magnitude-to-uncertainty ratio of 40, the possible characteristics of domain walls can be constraint by the measurement. The maximum event detected in the search data can be used to constrain the domain wall characteristics. Domain walls producing a greater magnitude-to-uncertainty ratio have not existed at least during our measuring time.

7

ALP DOMAIN SEARCH

The domain-walls search algorithm was calibrated and tested with simulated domain-wall crossings and background data (see Chapter 6). Thresholds on the analysis parameters, p-value and normalized angular difference, allow to discard events that most likely arise from noise (see Fig. 6.6). However, sensitivity to domain wall events is shown to be maintained (see Fig. 6.7). The evaluation of the background allows to quantify the significance of detected events in search data.

In this chapter, the results of the search for ALP domain walls are presented. Since no significant evidence for domain-wall crossings was found, the existence of ALPs in a region of their parameter space is excluded. Note that the parameter-space constraints here are based on the cosmological model in which ALPs form domain walls. These results were presented in Ref. [3]. Previously unexplored parameter space by direct searches has been constrained. The results contribute to the dynamic and developing field of direct dark matter and ALP searches.

7.1 SEARCH THE DATA FOR ALP DOMAIN WALLS

The search algorithm discussed in detail in Chapter 6 is applied to the search data after being carefully characterized. The domain-wall search on Science Run 2 data is summarized in Figure 7.1. Similarly to Fig. 6.8 the cumulative number of events found is plotted against the magnitude-to-uncertainty ratio threshold. On the upper axis, the significance in units of standard deviations of finding one or more events above a given ζ is given as defined in Eq. (6.8).

For $\zeta > 6$ only a few events were found. The event with largest magnitude-to-uncertainty ratio, ζ_{max} was measured at 12.6 followed by additional events at 6.2 and 5.6. The significance associated with finding one or more events in the search data above ζ_{max} magnitude-to-uncertainty ratio is lower than one sigma. Therefore, all events found are fully compatible with background. No events have been observed with a higher magnitude-to-uncertainty ratio than 12.6, even though the network was shown to be sensitive to such events (see Fig. 6.7). This fact is used to constrain the ALP parameter space.

7.2 ASSUMPTIONS FOR THE ALP SEARCH

Science Run 2 is used to constrain the existence of ALPs under the assumption that ALPs form domain walls which remain stable until present times. The formation of these topological defects is allowed but not necessary. Typically, the persistence of QCD axion domain walls until today is incompatible with cosmological observations. The

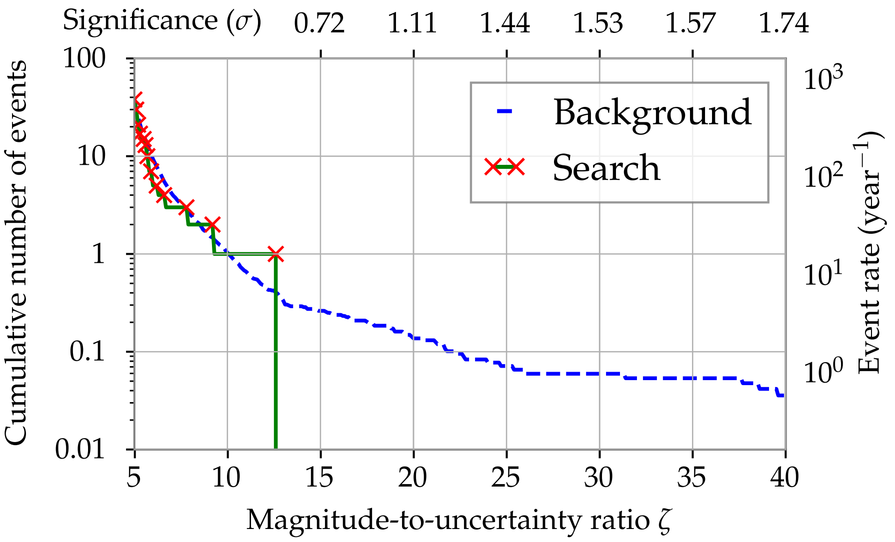

Figure 7.1: Results of the domain-wall crossing search in Science Run 2. Green line indicates the cumulative number of events found at different magnitude-to-uncertainty ratio thresholds. The red crosses indicate the point at which the number of events changes. As can be seen in the upper axes, the event with the highest magnitude-to-uncertainty ratio does not exhibit a significant deviation from the background.

energy contained in QCD domain walls would exceed the critical density for the universe to be flat, meaning that it will collapse [15]. The consideration of ALPs allow the energy density to be lower than the critical density while allowing domain walls to remain until today. In contrast to the QCD axion, for ALPs symmetry breaking scale, interaction scale and mass are independent. The larger number of parameters governing ALP domain walls, in comparison to the QCD axion, leaves them largely unconstrained. By making a variety of simplifying assumptions one can interpret the outcome of the domain-wall search to infer the properties of the ALPs under such scenario.

A peak-shaped signal is expected in the magnetometers based on the result from Eq. (5.6) and the consideration that only a linear coupling acts between spins and ALPs (see Eq. (5.11)). Such a signal is enhanced by averaging the data at similar time scales to the signal width. However, further generalizations of the coupling gives rise to signals with positive and negative components which are strongly suppressed by the averaging procedure. These generalizations were presented in Ref. [128].

The dynamics of ALP domain-walls are an open problem. However, their determination is crucial to extract ALP parameters from the experimental observables. Signal duration and average rate of crossings depend on the dynamics as well as on the ALP parameters as expressed in Eqs. (5.7) and (5.19). We consider domain walls to be non-interacting, trapped in the galaxy, and virialized. Therefore, they behave similarly to a gas of non-interacting particles trapped in the galactic gravitational potential (see Eq. (5.15)). This may not be the most accurate description of domain walls since these are typically described as a network structure permeating the galaxy with some degree of self-interaction [92]. However, the SHM assumption allows for an interpretation of the data in terms of the ALP theory.

The analysis assumes that the rate of domain-wall crossings is low compared to the duration of the measurement. No more that one event is expected to be found in the one month of data. In this regime, it is natural to consider the crossings to follow a Poisson distribution with some characteristic rate (see Eq. (5.21)). This justifies the fact that only the strongest event in the data is considered to draw conclusions about the ALPs. This method can be extended to consider larger rates, however the results are only slightly improved [128].

Even though ALPs can couple to different SM particles such as: protons, neutrons and electrons, the search is constrained solely to the coupling with protons. Due to the configuration of the GNOME sensors, the experiment is most sensitive to the proton coupling. The relation between the signal observed and the perturbation due to the ALP field is approximated by Eq. (5.13). Neutrons lie in closed shells for our probed atoms. Therefore, a signal arising from an interaction with neutrons is expected to be strongly suppressed. A component of the signal due to coupling with electrons is ignored since it will be suppressed by the magnetic shielding [121].

ALP domain walls could be a subdominant component of dark matter. Their energy density could be $\rho_{dw} < 0.4\ \mathrm{GeV/cm^3}$[1]. However, as it is typically assumed, we consider that all the dark matter energy density is stored in ALP domain walls.

7.3 CONSTRAINING THE ALP PARAMETER SPACE

No ALP domain-wall signals have been found above ζ_{max}. The region of ALP parameters producing signal above ζ_{max} can be therefore excluded. The area guaranteeing a confidence level $C > 90\,\%$ for the exclusion is evaluated using Eq. (5.23). The experimental parameters limiting this area are the detection probability $\epsilon(\mathcal{B}_p, \Delta t, \zeta < \zeta_{max})$ and the measurement time.

The colored region in Fig. 7.2 describes the interaction scale up to which GNOME was sensitive with at least 90 % confidence. This means that if ALPs exists within the colored region and form domain walls, we would have 90 % probability of detecting them. The parameter space is spanned by ALP mass and ratio between symmetry breaking and interaction scales. The shape of the sensitive area is largely determined by the shape of the detection probability. For light masses, the signal duration becomes long and the high-pass filter exponentially suppresses the signals. For heavy masses, the signal duration becomes short and the averaging linearly suppresses the signals. Additionally, for heavy masses, the signal amplitude increases linearly. This compensates the suppression of the averaging and GNOME remains sensitive to increasingly heavy masses. The ratio, ξ, scales linearly with the normalized magnetic field produced

---

[1] Note that this value has an statistical uncertainty of ~ 30 %[129].

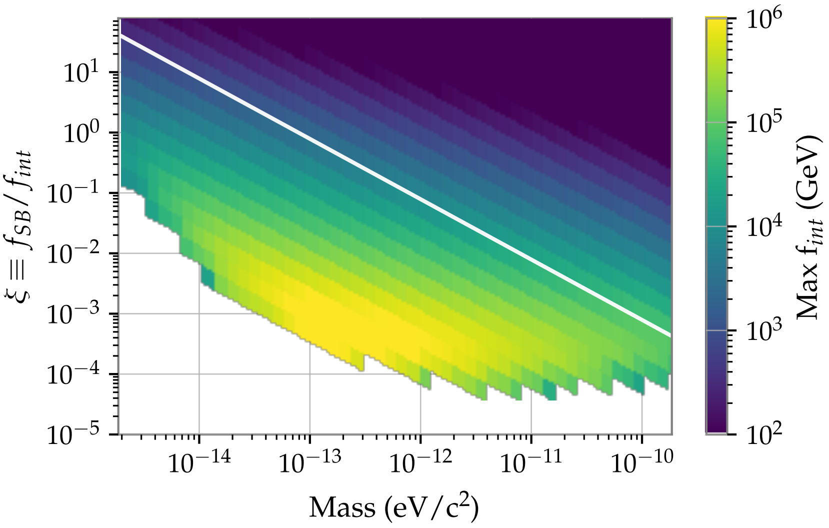

Figure 7.2: Constraints on symmetry breaking scale, interaction scale and mass of the ALPs resulting from the domain wall search in Science Run 2. The colored area featuring smaller interaction scale than Max f_{int} is excluded. Above the white line it is assumed that GNOME is sensitive to domain walls producing normalized pseudo-magnetic fields larger that the ones probed in Fig. 6.7.

by a domain wall. As ξ decreases, signals eventually falls out of the sensitive region of GNOME.

Even though $\mathcal{B}_p$ increases for heavy m_a, the mean rate of domain-wall encounters decreases[see Eqs. (5.9) and (5.19)]. Correspondingly, the upper limit for the interaction scale f_{int} degrades $\propto 1/\sqrt{m_a}$. Additionally, f_{int} is $\propto 1/\xi$ which produces tighter constraints for small ξ. Note that the area above the white line assumes that a domain-wall producing $\mathcal{B}_p$ larger than explored by Fig. 6.7 would be detected.

7.4 GNOME ALP DOMAIN WALLS SEARCH IN CONTEXT

Up to now the nature of dark matter has not been discovered. Large efforts are devoted to probe the parameter space of the QCD axion. As mentioned in Chapter 2, such a particle is a very promising dark matter candidate since it would solve the dark matter and the strong CP problems at the same time. Broadly speaking, current predictions set a range of masses between 10^{-6} to 10^{-3} eV/c^2 for the QCD axion to be the dark matter [78]. Experimental efforts like HAYSTACK and ADMX measure in this mass range and they have been able to rule out some of the parameter space [17, 18]. Most of the efforts in this mass range focus on the coupling of the QCD axion to photons. However, the exploration of other coupling is necessary to cover the whole plausible parameter space of the axion.

Highly motivated beyond-SM-physics such as the original axion with a symmetry breaking scale at the electroweak scale have been excluded. See a review about current constraints and discussion in Ref. [137]. These previously frustrated searches encourages researchers to expand their reach to less motivated but possible candidates. Even

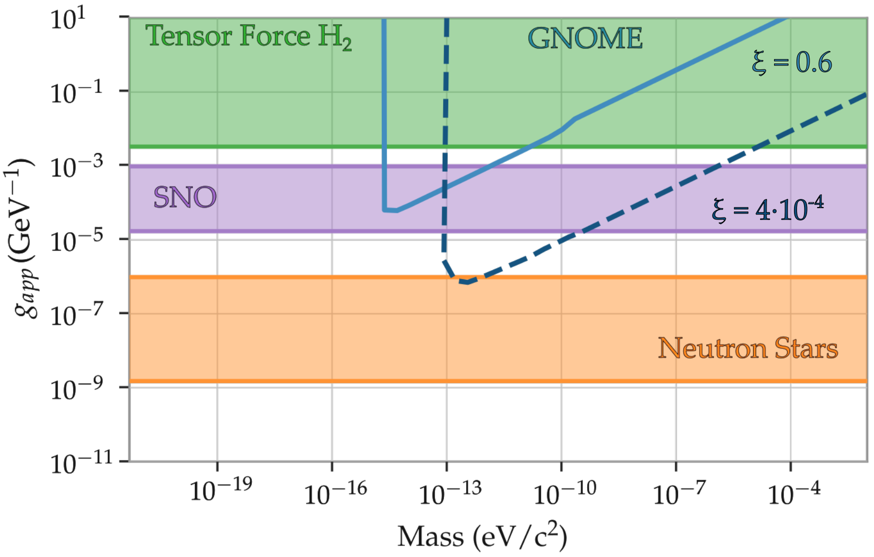

Figure 7.3: Constraints to the ALP proton coupling by GNOME compared to results of other experiments. GNOME is compared to dark matter independent constraints on the axion-proton coupling. These are: tensor force [30]; astrophysical constraints: Sudbury Neutrino Observatory (SNO) [24] and neutron stars [23]. Note that this plot assumes $\xi = 0.6$. However, GNOME is most sensitive to g_{ap} for $\xi = 6 \times 10^{-4}$ which is shown by the dashed dark blue line.

though the ALP cannot solve the strong CP problem, it can account for the dark matter. This is possible even at masses smaller than 10^{-6} eV [21]. The exact interval depends on the mechanism generating the their mass. Fortunately, the ALP cosmic phenomenology does not depend on the particular mechanism generating its mass [16]. This means that the same dark matter signatures will be observed independent of the mass range; such as annual modulation of signals or virialized velocity distribution of the particles. Since GNOME is solely sensitive to couplings with the proton spin, only constraints on the proton coupling are further discussed.

The axial-vector coupling of the axion (see Eq. (5.2)) can produce several observable effects. Accelerated nucleons can dissipate energy through emission of ALPs. This effect can be important in astrophysical objects like supernovae and neutron stars. There are several cooling effects of nucleons emitting axion; such as nucleon scattering, axion bremsstrahlung, and axion production from Cooper pair breaking and formation. Simulations are performed to evaluate their effect in the luminosity of astrophysical objects and then this is compared to observations. Currently, the most robust constraint originate from observation of neutron stars [23]. The supernova SN1987A was also used to constrain ALPs [22, 138]. This constraints are based on the cooling of the proto-neutron star assumed to form after the supernova explosion. However, this assumption has received some criticism which can invalidate the constraints [139]. Since the constraints from SN1987A and the cooling of neutron stars are comparable, for the sake of simplicity, only the ones extracted from the neutron stars are shown in Fig. 7.3. Note that these constraints are also bound for strong coupling because then ALPs cannot escape and cool the neutron star down.

The axial-vector coupling also allows the emission of high energy ALPs in nuclear transitions occurring in the Sun. The relevant transition happening in the Sun which can produce axions is

$$p + d \rightarrow 3He + ALP(5.5MeV), \tag{7.1}$$

where p denotes a proton and d a deuteron. Based on the standard solar model, this flux of high energy ALPs can be related to the know proton-proton neutrino flux. The ALPs emitted can dissociate deuterium on Earth into a neutron and a proton leaving an observable signal. Both interactions are governed by a single axion-nucleon coupling. This is the isovector coupling $g^3_{aN} = (g_{an} - g_{ap})/2$ from which the proton coupling can be extracted. The Sudbury Neutrino Observatory relies on large quantities of heavy water for resolving solar neutrinos. The abundance of deuterium in this experiment was used to constrain the ALP parameter space [24].

To find direct laboratory measurements of exotic forces in protons, one has to go back to 1979 [30]. Norman Ramsey performed accurate measurements of the vibration and rotational states of H_2 molecules. Such a precision measurement set limits on exotic tensor forces between protons. These constraint can be reinterpreted to constrain the proton coupling of ALPs [32]. Note that this is a highly model independent measurement. Recently, experiments searching for exotic spin dependent forces between a ^{3}He sample and a K-^{3}He comagnetometer can also be used to constrain the coupling to protons [31]. Reinterpreting the results in Ref. [31] sets a limit on the proton coupling to $g_{app} \gtrsim 4 \times 10^{-4}$ in range of masses from 0 to 10^{-6} eV.

It is important to note that typically, exotic-force searches publish their constrains as a function of the dimensionless coupling $g^N_p/\sqrt(4\pi\hbar c)$ while dark matter searches use g_{aNN} which has units of inverse energy. One can change from one convention to the other as $g^N_p/\sqrt(4\pi\hbar c) = g_{aNN} 2m_N$, where m_N is the mass of the nucleon being considered.

Searches for the ALP axial-vector coupling can be extended by assuming that ALPs are the main component of dark matter. In this scenario, the sensitive apparatus interacts with the local ALP dark-matter background. GNOME's spatial resolution and data redundancy make it particularly suitable for the detection of transient phenomena. This contrasts with the most common assumption for ALP dark matter cosmology. Most commonly it is assumed that the ALP field continuously oscillates around their potential minimum creating a constant oscillating signal. However, a rich amount of proposed scenarios producing transient signal exist, such as; topological defects like domain walls [2], boson stars [140], dark matter blobs [7]. These can be probed by GNOME and other sensor networks. Searches for dark matter structures have been realized using; GPS atomic clocks [141], accelerometer networks [8], quantum gravimeters [142]. However, GNOME is the first quantum sensor network dedicated to exotic physics searches.

GNOME explored the ALP parameter space formed by coupling scale, symmetry breaking scale and mass assuming that the whole dark matter density is in the form of ALP domain walls. The dark matter independent experiments reviewed in the previous paragraphs are sensitive to the coupling scale and mass. In order to make the results comparable, we assume $f_{SB}/f_{int} = 0.6$ which is the expected value for the QCD axion [14]. The projection of Fig. 7.2 onto $\xi = 0.6$ is plotted in Fig. 7.3. In this figure, the proton coupling is given by $g_{app} = f_{int}^{-1}$. The GNOME constrains go beyond that excluded by the search for tensor forces in hydrogen molecules which have shown that $f_{int} \gtrsim 300\,\text{GeV}$ and reach up to the Sudbury Neutrino Observatory (SNO) constrains. The best bound on g_{app} by GNOME is obtained for $\xi = 4 \times 10^{-4}$ which is plotted with a dashed dark blue line in the figure even though such ratio is not possible for the QCD axion. Note that cosmological constraints given by neutron star cooling ar not sensitive to couplings larger than $\sim 10^{-6}$. Therefore, laboratory experiments, even if less sensitive can still explore unconstrained parameter space.

8

FEATURES AND EXPECTED SENSITIVITY TO ULTRALIGHT BOSONIC DARK MATTER FIELDS

GNOME has targeted its data analysis efforts to search for clumped dark matter. The global network of sensors allows to spatially resolve structures such as domain walls [3], boson stars [4, 143], Earth or Solar axion halos [144] and dark blobs [7]. However, GNOME could also be sensitive to uniformly distributed dark matter [6]. If the ALP field is composed of a large number of virialized bosons, it will exhibit finite coherence time and length. The motion of the ALPs slightly alters their Compton frequency. The interference of the Doppler-shifted boson waves produces stochastic fluctuations in the amplitude of the field. GNOME, due to its limited bandwidth, is sensitive to frequencies $\lessapprox 100\,\mathrm{Hz}$ which correspond to very low ALP masses $\lessapprox 10^{-13}\,\mathrm{eV}$. However, if the ALPs interact with the protons through a coupling quadratic in the field, the signal will feature a near-dc frequency component. The fluctuations in the amplitude result in a characteristic signal 10^6 slower than the Compton frequency. Therefore, the sensitive mass range of GNOME can be considerably improved towards higher masses. For a certain range of parameters this signal will be correlated between the GNOME magnetometers. This correlation is signature of dark matter which could be observed by GNOME.

This chapter discusses the use of a technique inspired by the Hanbury Brown and Twiss intensity interferometry experiment to search for this globally correlated signal. First, the stochastic properties of the ALP field are discussed and an interaction term quadratic on the field is proposed. Then the expected signature of the ALP field interacting through this quadratic coupling is modeled. Finally, an estimation of the ALP parameter space accessible by the network is presented. This discussion was published in Ref. [6] and parts of this chapter are adapted from that publication.

8.1 STOCHASTIC AXION-LIKE DARK MATTER FIELD

Even if the formation of sub-galactic ALP dark matter structures is possible [82, 88], as it was discussed in the previous chapters, it requires additional assumptions and tuning of the ALP parameters to remain stable. Therefore, an intrinsic interest exists in the GNOME collaboration to probe the conventional dark matter paradigm in which the ALP field is expected to be uniform at the solar system scale.

In the lack of structures, ALP dark matter can be described as a gas of non-interacting particles trapped in the galaxy. In the low-mass range, $m_a \ll 1\,\mathrm{eV/c^2}$, the high occupation number allows to describe the field as a superposition of plane waves. Therefore, the field can be modeled as the superposition of N oscillators [1]

$$\varphi(\boldsymbol{r},t) = \sum_{n=1}^{N} \frac{\varphi_0}{\sqrt{N}} \cos\left(\omega_n t - \boldsymbol{k}_n \cdot \boldsymbol{r} + \theta_n\right) , \tag{8.1}$$

where m_a is the boson mass and ρ_{dw} is the local dark-matter energy density. The amplitude of oscillation is given by [16]

$$\varphi_0 = \frac{\hbar}{m_a c}\sqrt{2\rho_{\mathrm{dm}}}, \tag{8.2}$$

such that the average energy density in the ALP field comprises the totality of the local dark matter. Here, a local dark matter density of $\rho_{\mathrm{dm}} = 0.3\,\mathrm{GeV/cm^3}$ is assumed[2]. The wave-vector $\boldsymbol{k}_n = m_a \boldsymbol{v}_n/\hbar$ corresponds to the velocity $\boldsymbol{v}_n$ of the n^{th} oscillator in the laboratory frame. The phase θ_n of each oscillator follows a flat distributed between 0 and 2π. The oscillation frequency ω_n is determined mostly by the Compton frequency ω_c of the underlying ultralight boson. Kinetic energy corrections to the rest energy introduces small deviations from ω_c, so that

$$\omega_n = \omega_c\left(1 + \frac{\boldsymbol{v}_n^2}{2c^2}\right). \tag{8.3}$$

Therefore, the distribution of ω_n (and $\boldsymbol{k}_n$) is determined by the velocity distribution as observed in the laboratory frame. According to the standard halo model, $\boldsymbol{v}_n$ follows a displaced Maxwell-Boltzmann distribution given by

$$f^{(3)}_{\mathrm{lab}}(\boldsymbol{v}_n) = f^{(3)}_{\mathrm{gal}}(\boldsymbol{v}_n - \boldsymbol{v}_{\mathrm{L}})\,. \tag{8.4}$$

The probability distribution $f^{(3)}_{\mathrm{gal}}$ was presented in Sec. 5.3. In this case, the oscillators do not feature internal degrees of freedom related to the motion and a truncation at the escape velocity is omitted. Therefore, no further modifications are needed unlike the domain-wall case discussed in Sec. 5.3.

The field in Eq. (8.1) is characterized by an oscillation at the Compton frequency, ω_c and a stochastic varying amplitude. Studying the distribution of oscillators in each velocity class, the power spectral density of the ALPs can be estimated [145]. Approximating the power spectral density with a Lorentzian, the characteristic coherence time of the field $\varphi(\boldsymbol{r},t)$ is given by [146]

$$\tau_\varphi \approx \frac{2\hbar}{m_a v_0^2}\,. \tag{8.5}$$

---

[1] The individual bosons should be modeled as quantum objects not classical fields. However, the huge occupancy numbers of each mode allows to accurately model the ALP field as a superposition of classical oscillators. For example, a boson mass of $10^{-11}\,\mathrm{eV/c^2}$ (and $\rho_{\mathrm{dm}} = 0.3\,\mathrm{GeV/cm^3}$) results in a number density of particles of $\sim 10^{19}\,\mathrm{cm^3}$. The de Broglie wavelength for particles moving with v_{L}, is $\sim 10^{10}$ cm.

[2] Note that this value has as estimated statistical uncertainty of 30 % [129]

This is the time after which the phase of the field becomes unpredictable. This is also the characteristic time at which the stochastic fluctuations of the amplitude occur.

An important feature of the coherence time τ_φ is that it is six orders of magnitude larger than the period given by the Compton frequency [146]. This is a consequence of the kinetic energy corrections to the rest energy (see Eq. (8.3)) in which the ALP speed is weighted with the speed of light. Therefore, the spread in frequencies is $\boldsymbol{v}_0^2/c^2 \approx 10^{-6}$. An ALP with Compton frequency $\approx 100\,\mathrm{Hz}$ would have a mass of $\approx 10^{-12}\,\mathrm{eV}/c^2$. Being sensitive to the amplitude fluctuations will move the observable range of masses to $\approx 10^{-6}\,\mathrm{eV}/c^2$ with the same apparatus. This approaches an interesting mass range in which the QCD axion can reproduce the observed dark matter relic abundance [78].

8.2 QUADRATIC INTERACTION WITH ORDINARY MATTER

In addition to the linear interaction presented in Eq. (5.2), a coupling quadratic in the field is also possible. The phenomenological interaction Lagrangian can be written as [4]

$$\mathcal{L}_q = \pm\frac{1}{f_q^2}\underbrace{\bar{\psi}_f\gamma^\mu\gamma_5\psi_f}_{\substack{\text{fermion axial}\\\text{vector current}}}\partial_\mu\varphi^2(\boldsymbol{r},t)\,, \tag{8.6}$$

where f_q parameterizes the quadratic coupling to fermion spins, γ^μ and γ_5 are the Dirac matrices. Note that the constant governing the interaction, f_q, is independent of f_{int}. Moreover, f_q appears squared in Eq. (8.6) which implies that large f_q are increasingly difficult to measure.

In the nonrelativistic limit, Eq. (8.6) yields the interaction Hamiltonian

$$\mathcal{H}_q = \mp\frac{2\hbar^2c^2}{f_q^2}\hat{\boldsymbol{S}}\cdot\boldsymbol{\nabla}\varphi^2(\boldsymbol{r},t)\,. \tag{8.7}$$

Such Hamiltonian features similar properties to the one characterizing the domain wall interaction (see Eq. (5.11)) with the novelty of being quadratic on the field. Now, the term $\boldsymbol{\nabla}\varphi^2(\boldsymbol{r},t)$ plays the role of the pseudo-magnetic field $\mathcal{B}_p$.

The quadratic interaction is proportional to $\boldsymbol{\nabla}\varphi^2(\boldsymbol{r},t)$ which is composed of two terms: one near-dc component and one fast oscillating component at $\approx 2\omega_c$. Considering sensors with a limited bandwidth $\Delta\omega \ll \omega_c$ the fast oscillating terms can be ignored. Using this approximation the near-dc component (denoted by the subscript s) can be written as

$$\boldsymbol{\nabla}\varphi_s^2(\boldsymbol{r},t) = \frac{\varphi_0^2}{2N}\sum_{n,m=1}^{N}\boldsymbol{k}_{nm}\sin\left(\omega_{nm}t - \boldsymbol{k}_{nm}\cdot\boldsymbol{r} + \theta_{nm}\right), \tag{8.8}$$

where $\omega_{nm} = \omega_n - \omega_m$, $\boldsymbol{k}_{nm} = \boldsymbol{k}_n - \boldsymbol{k}_m$, and $\theta_{nm} = \theta_n - \theta_m$.

For simplicity, the sensors are assumed to be within the same coherence patch (such that $\Delta \boldsymbol{k} \cdot \Delta \boldsymbol{r} \approx 0$, where $\Delta \boldsymbol{k}$ is the characteristic spread of $\boldsymbol{k}_{\mathrm{nm}}$ and $\Delta \boldsymbol{r}$ is characteristic distance between sensors), the $\boldsymbol{r}$ dependence can be neglected and the expressions are evaluated at $\boldsymbol{r} = 0$ in the following calculations [147]. Note that the coherence length, λ_c, depends on the mass, $\lambda_c = \hbar/(m_a v_0)$ [95]. Therefore, for sufficiently large masses ($>2 \times 10^{-11}\,\mathrm{eV}/c^2$) the coherence patch is smaller than Earth diameter which means that the assumption for the presented analysis breaks down.

Equation (8.8) dictates the properties of the dark matter signature. The equation is composed of two elements: an oscillating part $\sin(\omega_{\mathrm{nm}} t + \theta_{\mathrm{nm}})$ and a weight given by $\boldsymbol{k}_{\mathrm{nm}}$. These two quantities have a common dependence on the velocity. The relative wave-vector $\boldsymbol{k}_{\mathrm{nm}}$ depends on the difference in the velocity components while ω_{nm} depends on the difference in speeds. Oscillating terms with larger value of $\boldsymbol{k}_{\mathrm{nm}}$ will contribute more to the sum.

Note that if $\boldsymbol{k}_{\mathrm{nm}}$ and ω_{nm} were uncorrelated, Eq. (8.8) could be split into two independent sums. In that case, the behavior of $\nabla\varphi^2(\boldsymbol{r}, t) \sim \varphi^2(\boldsymbol{r}, t)$ since the sum of $\boldsymbol{k}_{\mathrm{nm}}$ will be a constant multiplying the sum of the sines. The spectral composition[3] of $\varphi(\boldsymbol{r}, t)$ is known [145] therefore, the convolution theorem[4] could be used to extract the spectral properties of $\varphi^2(\boldsymbol{r}, t)$. Unfortunately, such a trick cannot be applied to $\nabla\varphi^2(\boldsymbol{r}, t)$. Even though the spectral composition of $\nabla\varphi(\boldsymbol{r}, t)$ is also known [146], the properties of $\nabla\varphi^2(\boldsymbol{r}, t)$ have to be studied numerically.

In order to gain intuition on the difference expected between $\nabla\varphi^2(\boldsymbol{r}, t)$ and $\varphi^2(\boldsymbol{r}, t)$, one can decompose $\boldsymbol{k}_{nm}$ into parallel and perpendicular components to $\boldsymbol{v}_{\mathrm{L}}$. This yields the following relationships:

$$\boldsymbol{k}^{\parallel}_{\mathrm{nm}} = \frac{m_a \boldsymbol{v}^{\parallel}_{\mathrm{nm}}}{\hbar}, \text{ and } \boldsymbol{k}^{\perp}_{\mathrm{nm}} = \frac{m_a \boldsymbol{v}^{\perp}_{\mathrm{nm}}}{\hbar}. \tag{8.9}$$

The velocity differences are indicated by $\boldsymbol{v}_{\mathrm{nm}} = \boldsymbol{v}_{\mathrm{n}} - \boldsymbol{v}_{\mathrm{m}}$. The superscripts $\parallel$ and $\perp$ indicate whether the component is parallel or perpendicular to $\boldsymbol{v}_{\mathrm{L}}$. Note that $\boldsymbol{v}_{\mathrm{nm}}$ are independent on $\boldsymbol{v}_{\mathrm{L}}$. One can also write the frequency differences in terms of the velocity components as

$$\begin{aligned}\frac{2c^2\omega_{\mathrm{nm}}}{\omega_c} = {} & (\boldsymbol{v}^{\parallel}_{\mathrm{n}} + \boldsymbol{v}^{\parallel}_{\mathrm{m}}) \cdot \boldsymbol{v}^{\parallel}_{\mathrm{nm}} + (\boldsymbol{v}^{\perp}_{\mathrm{n}} + \boldsymbol{v}^{\perp}_{\mathrm{m}}) \cdot \boldsymbol{v}^{\perp}_{\mathrm{nm}} \\ & - 2\boldsymbol{v}_{\mathrm{L}} \cdot \boldsymbol{v}^{\parallel}_{\mathrm{nm}}.\end{aligned} \tag{8.10}$$

Even if the relation is not linear, one can see in the first two terms in the right part of Eq. (8.10) that the frequency difference increases with $\boldsymbol{v}^{\parallel}_{\mathrm{nm}}$ and $\boldsymbol{v}^{\perp}_{\mathrm{nm}}$. In contrast, a proportional dependence of the frequency difference is found in the third term with $\boldsymbol{v}^{\parallel}_{\mathrm{nm}}$ being weighted with the speed of Earth. These relationships are illustrated in Fig. 8.1.

---

[3] The Wiener–Khinchin theorem establishes a link between the power spectrum and the autocorrelation function.

[4] A consequence of the convolution theorem states for two functions g and f that $g \cdot f = \mathcal{F}^{-1}\{\mathcal{F}\{g\} \star \mathcal{F}\{f\}\}$, where $\mathcal{F}$ indicates the Fourier transform, $\cdot$ the pointwise multiplication and $\star$ the convolution.

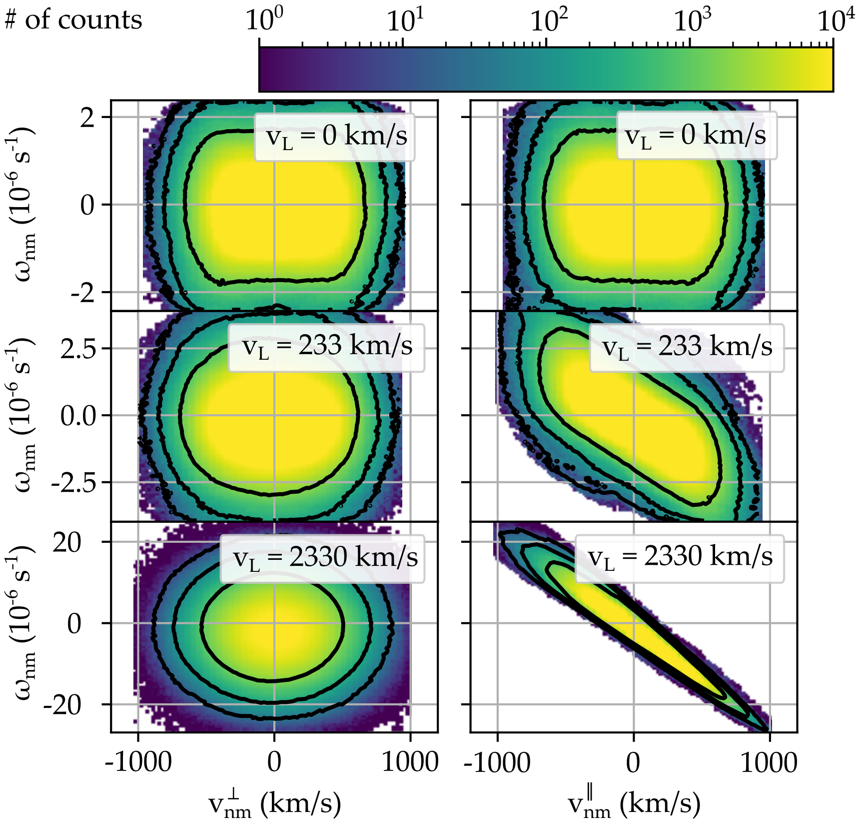

Figure 8.1: Visualization of the dependence between the frequency differences ω_{nm} and the difference of velocities v_{nm}. Note that v_{nm} are proportional to the difference of wave-vectors k_{nm}. The components of the velocities are expressed as perpendicular and parallel with respect to Earth velocity $\boldsymbol{v}_L$. This dependence is plotted for different values of $|\boldsymbol{v}_L|$

Figure 8.1 shows the simulation of 10^2 runs of 10^3 oscillators moving according to the probabilities defined in Eq. (8.4) with varying v_L. For each run the difference of frequencies is plotted with respect to the difference in velocities. The components perpendicular and parallel to v_L are plotted separately. One can see that for $v_L = 0$ the non-linear relationship in the first two terms in Eq. (8.10) produces a square-like shape. Large $\boldsymbol{v}_{nm}^{\perp}$ tend to produce larger ω_{nm}. The coherence time of $\boldsymbol{\nabla}\varphi^2(\boldsymbol{r}, t)$ is therefore expected to shorten with respect to φ^2. Such dependence fades away with increasing v_L. In contrast, the third term in Eq. (8.10) results in a linear dependence that elongates the distribution for velocity differences along v_L. Larger parallel velocity differences produce larger frequency differences. This implies that, for the parallel component of $\boldsymbol{\nabla}\varphi_s^2(\boldsymbol{r}, t)$, higher frequencies have more weight in the sum. For the perpendicular component all contributions are mostly equal. Due to this, the coherence time measured along v_L is shorter than the coherence time measured perpendicular to v_L.

8.3 SIGNATURE OF THE STOCHASTIC BACKGROUND FIELD

Direct detection of ALP dark matter is typically based on the fact that the ALP background field oscillates at the Compton frequency of the particle, $\omega_c = m_a c^2/\hbar$. Experimental parameters are scanned with the hope of tuning to this unknown frequency. When the Compton frequency is matched, a characteristic signal is expected. Such an approach boosts the sensitivity but involves a cumbersome scanning of the sensitive frequency range [17, 18, 150]. In contrast, the stochastic fluctuations of the field background occur at a frequency $\approx 10^6$ slower than the Compton frequency. If these fluctuations can be resolved, their coherence properties can be exploited to preform a search covering a broad range of masses.

8.3.1 *First order degree fo coherence*

The correlation between measured signals in different sensors can be quantified using the degree of first-order coherence $g^{(1)}(\tau)$. For a delay time τ and some signal $\Upsilon(t)$ the first-order coherence is defined as

$$g^{(1)}(\tau) = \frac{\langle \Upsilon(t)\Upsilon(t+\tau)\rangle_t}{\langle \Upsilon^2\rangle_t} , \tag{8.11}$$

where $\langle\cdots\rangle_t$ denotes the time average. In our application $\Upsilon(t)$ corresponds to any projection of the field to the sensitive axis $\hat{\boldsymbol{n}}_j \cdot \boldsymbol{\nabla}\varphi_s^2$. Where $\boldsymbol{n}_j$ is the directional sensitivity of a given sensor.

The value of $g^{(1)}(\tau)$ is a measure of the degree of correlation between $\Upsilon(t)$ and $\Upsilon(t+\tau)$. Based on degree of first-order coherence, the coherence time can be defined as the power-equivalent width of $g^{(1)}(\tau)$ as

$$\tau_c = \int_{-\infty}^{+\infty} |g^{(1)}(\tau)|^2 d\tau. \tag{8.12}$$

This describes the characteristic temporal width of $g^{(1)}(\tau)$ [151]. Note that there is an ambiguity, up to a factor of 2π, in the definitions of τ_c used in the literature [5].

8.3.2 *Numerical simulation*

To study the stochastic properties of $\boldsymbol{\nabla}\varphi^2(0,t)$, its time evolution was simulated and then the degree of first-order coherence is calculated. In order to numerically calculate the near-dc components of φ^2 and avoid the double summation in Eq. (8.8), it is convenient to introduce the field in complex notation

$$\varphi_c(0,t) = \frac{\varphi_0}{\sqrt{N}} \sum_{n=1}^{N} \exp\left[i(\omega_n t + \theta_n)\right], \tag{8.13}$$

so that $\varphi(0,t) = \mathcal{R}[\varphi_c(0,t)]$. The near-dc component of the field squared is given by

$$\varphi_s^2 = \frac{1}{2}\varphi_c\varphi_c^*. \tag{8.14}$$

This is a real number describing the time average of φ^2 over a cycle of oscillation. The chain rule is applied to numerically evaluate $\boldsymbol{\nabla}\varphi_s^2$,

$$\begin{aligned}\boldsymbol{\nabla}\varphi_s^2(\boldsymbol{r},t)\Big|_{\boldsymbol{r}=0} =& \frac{i}{2}\varphi_c\frac{\varphi_0}{\sqrt{N}}\sum_{n=1}^{N}\boldsymbol{k}_n \exp\left[-i(\omega_n t+\theta_n)\right] \\ & -\frac{i}{2}\varphi_c^*\frac{\varphi_0}{\sqrt{N}}\sum_{n=1}^{N}\boldsymbol{k}_n \exp\left[i(\omega_n t+\theta_n)\right].\end{aligned} \tag{8.15}$$

Note that by first evaluating Eq. (8.13) to obtain $\varphi_c(0,t)$ and then evaluating Eq. (8.15) to find $\boldsymbol{\nabla}\varphi_s^2$, the sum to be performed contains N terms corresponding to the number of bosons simulated. In contrast, the equivalent Eq. (8.8), contains N^2 terms. This makes numerical calculations with Eq. (8.15) considerably more efficient for large N. In addition, Eq. (8.14) allows to obtain the near-dc component of φ^2 without the need of resolving the Compton frequency in the simulation.

The individual wave vectors $\boldsymbol{k}_n$ and frequencies ω_n are calculated from the velocities $\boldsymbol{v}_n$. These velocities are drawn from the displaced Maxwell-Boltzmann distribution in Eq. (8.4). The phases θ_n are drawn from a uniform distribution spanning from 0 to 2π.

The simulations consider $N = 10^3$ oscillators evolving during $20\,\tau_\varphi$ with a time resolution of $0.05\,\tau_\varphi$, where τ_φ is given by Eq. (8.5). The temporal resolution and the duration of the simulated were chosen considering plausible values for an experimental search. After generating $\boldsymbol{\nabla}\varphi_s^2$, $g^{(1)}(\tau)$ is calculated using Eq. (8.11). Note that the mean value of the field is subtracted so that $g^{(1)}(\tau) \to 0$ for $\tau \gg \tau_\varphi$. The coherence time [as defined in Eq. (8.12)] can be obtained by integrating numerically. The integration is realized considering the data over the time interval $[0, 5\tau_\varphi]$, and multiplying by two in order to account for the negative segment of the range since the line-shape is symmetric around $\tau = 0$. Plots of $g^{(1)}(\tau)$ for the projections of $\boldsymbol{\nabla}\varphi_s^2(t)$ onto parallel and perpendicular directions with respect to $\boldsymbol{v}_{\text{lab}}$ can be seen in Fig. 8.2a.

In order to check the results of the simulation, three arguments are used. First, an analytical expression for the first order degree of coherence of $\boldsymbol{\nabla}\varphi_s^2$ was calculated. Due to integrals involved only the limit for $v_L \gg v_0$ can be expressed analytically. The simulation shows good agreement with this analytical solution as can be seen in Ref. [6] Appendix D.

Second, the simulated power spectrum of φ_s^2 was compared with a theoretical calculation. The power spectrum of the ALP field φ was published in Ref. [145]. Using this information and applying the convolution theorem φ_s^2 can be calculated. These two results agreed.

Third, Fig. 8.2b shows the behavior of the coherence time of the different fields $\boldsymbol{\nabla}\varphi_s^2$, φ_s^2 and φ_s as a function of Earth speed. From

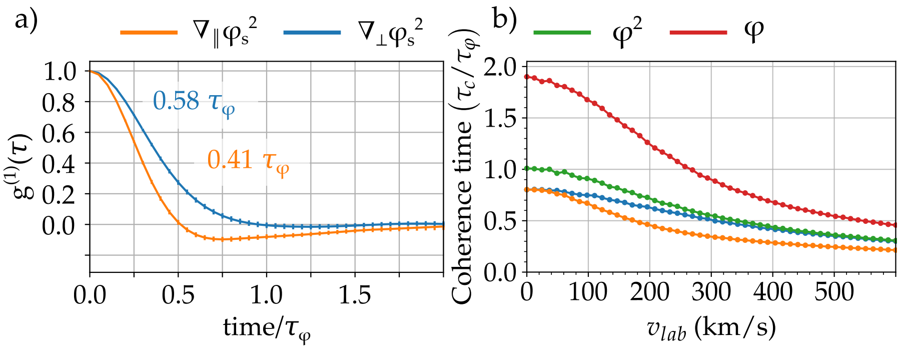

Figure 8.2: Study of the coherence time of the ALP field. a) Simulation of the first order of coherence for $\boldsymbol{\nabla}_{\perp}\varphi_s^2$ and $\boldsymbol{\nabla}_{\parallel}\varphi_s^2$ averaged for 10^3 times. b) Simulation of the coherence time calculated as defined in Eq. (8.12) for varying v_{lab} and different fields $\boldsymbol{\nabla}_{\perp}\varphi_s^2$, $\boldsymbol{\nabla}_{\parallel}\varphi_s^2$, φ_s^2 and φ_s averaged for $2 \cdot 10^3$ times.

Eq. (8.10), it is expected that for $v_L \gg v_0$ the coherence time of $\boldsymbol{\nabla}_{\perp}\varphi_s^2$ tend to the coherence time of φ_s^2 while $\boldsymbol{\nabla}_{\parallel}\varphi_s^2$ continually decreases. For $v_L \ll v_0$ the coherence time of $\boldsymbol{\nabla}_{\perp}\varphi_s^2$ and $\boldsymbol{\nabla}_{\parallel}\varphi_s^2$ should be the same. Additionally, the coherence time of φ should be approximately double with respect to the φ_s^2 at any v_L due to the convolution theorem. These characteristics are checked in Fig. 8.2b.

Because the actual lineshape describing φ is expected to be non-Lorentzian [146], τ_φ slightly differs from the coherence time of the field φ derived from the simulations. The simulations show a coherence time $\approx 1.12(1)\tau_\varphi$ for $v_L = 233\,\text{km/s}$. These checks assure that our simulations accurately describe the coherence properties of $\boldsymbol{\nabla}\varphi_s^2$ and φ_s^2.

8.3.2.1 *Search method*

In order to illustrate a method that could be used to search for ALP fields using intensity interferometry, let us consider a measured time-series $\mathcal{S}_{A,B}(t)$ lasting several τ_φ from two different sensors, A and B. When using pairs of independent and geographically distributed sensors, a correlated global background field will produce a nonzero cross-correlation $g^{(1)}_{AB}(\tau)$ between sensors A and B. However, not only the coherence properties of the field are important but also the amplitude of the correlated signal. Therefore, it is convenient to not normalize the first degree of coherence. Such observable can be defined as

$$\mathcal{O}(\tau) = \langle \mathcal{S}_A(t)\mathcal{S}_B(t+\tau)\rangle_t \,. \tag{8.16}$$

In the presence of a stochastic ALP field, the measured time-series can be expressed as $\mathcal{S}_{A,B} = \kappa_{A,B}s_{A,B}(t) + \mathcal{N}_{A,B}(t)$. Where $\mathcal{N}_{A,B}(t)$ accounts for the local noise sources which are assumed to be Gaussian distributed with mean zero and variance σ^2. The ALP signal is given by $\kappa_{A,B}s_{A,B}(t)$. Where the factor $\kappa_{A,B}$ accounts for coupling of the sensor to the ALP field, and $s_{A,B}(t) = \hat{\boldsymbol{n}}_{A,B} \cdot \boldsymbol{\nabla}\varphi_s^2$. For simplicity in the notation, the factors $\kappa_{A,B} = 1$ and the two sensors point along the same direction, $\hat{\boldsymbol{n}}$. Generally, there will be a difference between $s_A(t)$ and $s_B(t)$ because of the spatial dependence $\nabla\varphi^2$ that arises from the $\boldsymbol{k}\cdot\boldsymbol{r}$ term in Eq. (8.1). However, for the considered ALP mass range, the coherence length is much larger than the distance between the sensors. Then the ALP field observed is considered to be the same for both sensors, $s_{A,B}(t) = s(t)$.

The quantity $\mathcal{O}(0)$ can be used to determine whether or not a global correlated signal is present in the data. A $\mathcal{O}(0) > 0$ will hint to the presence of an ALP stochastic background field. While $\mathcal{O}(0) = 0$ within the accuracy of the experiment would place a bound on the strength of the interaction. In order to quantify the significance of a measurement $\mathcal{O}(0)$, a signal-to-noise ratio is defined as

$$\mathcal{O}_{S/N} = \frac{E[\mathcal{O}(0)]}{\sqrt{Var[\mathcal{O}(0)]}} = \frac{E[\mathcal{S}_A\mathcal{S}_B]}{\sqrt{Var[\mathcal{S}_A\mathcal{S}_B]}}\,. \tag{8.17}$$

Over many measurements of $\mathcal{O}(0)$, E denotes the expected value and Var the variance. Note that $\langle ...\rangle_t$ and E are effectively the same operation. Therefore, $E[\langle\mathcal{S}_A\mathcal{S}_B\rangle_t] = E[\mathcal{S}_A\mathcal{S}_B]$ and the same applies for the variance. Measuring $\mathcal{O}(0)$ several times is equivalent to performing longer time averages.

The field term $s(t)$ follows a probability distribution with $E[s(t)] = 0$ and $Var[s(t)] = s_0^2$. The variance of $s(t)$ can be interpreted as the square of the root-mean-squared (RMS^2) of the field. This characterizes the strength of the measurable signal produced by the ALP field. Since the noise sources of the two sensors are uncorrelated, $E[\mathcal{S}_A\mathcal{S}_B] = s_0^2$[5]. The variance in the product of the two time series is more challenging to evaluate. By definition the variance is given by

$$Var[\mathcal{S}_A\mathcal{S}_B] = E[\mathcal{S}_A\mathcal{S}_B\mathcal{S}_A\mathcal{S}_B] - E^2[\mathcal{S}_A\mathcal{S}_B]\,. \tag{8.18}$$

The term $E[\mathcal{S}_A\mathcal{S}_B\mathcal{S}_A\mathcal{S}_B]$ has to be carefully expanded since the terms in the expansion exhibits correlation. Exploiting that $E[XY] = E[X]E[Y]$ for uncorrelated random variables and the identity of the covariance $Cov[XY, X] = E[X^2, Y] - E[X, Y]E[X]$, one finds that

$$E[\mathcal{S}_A\mathcal{S}_B\mathcal{S}_A\mathcal{S}_B] = s_0^4 + 2s_0^2\sigma^2 + \sigma_{AB}^2\,. \tag{8.19}$$

For random variables with expectation value equal to zero $E[X^2] = Var[X]$ therefore $E[\mathcal{N}_A^2] = E[\mathcal{N}_A^2] \equiv \sigma^2$ and $E[\mathcal{N}_A\mathcal{N}_B\mathcal{N}_A\mathcal{N}_B] \equiv \sigma_{AB}^2$. Interestingly, for independent variables with $E[X] = E[Y] = 0$, $Var[XY] = Var[X]Var[Y]$. Therefore, $\sigma_{AB}^2 = \sigma^4$. Finally, the signal-to-noise ratio for our observable is given by

$$\mathcal{O}_{S/N} = \frac{s_0^2}{\sqrt{2s_0^2\sigma^2 + \sigma^4}}\,. \tag{8.20}$$

Even though $s(t)$ averages to zero for times longer than the coherence time, $\mathcal{O}(0)$ converges to s_0^2. Since $\mathcal{O}(0)$ is the sum of a large

---

[5] This easily follows from the definition of variance, $Var[X]] = E[X^2] - E[X]^2$, for probability distributions with zero mean.

amount of terms, the central limit theorem states that its probability distribution follows a Gaussian. Therefore, the variance of $\mathcal{O}(0)$ scales as $\mathrm{Var}[\mathcal{O}(0)]/N$, where N is the number of samples.

It is important to note that our observable (see Eq. (8.16)) is quadratic with the ALP interaction (see Eq. (8.7)). Therefore, it interesting to consider how the s_0 needed to reach a certain $\mathcal{O}_{S/N}$ scales with the number of averages of $\mathcal{O}(0)$. Two regimes can be differentiated: signals above the noise background $s_0^2/\sigma^2 \to \infty$ and signals bellow the noise background $s_0^2/\sigma^2 \to 0$.

For the first case, taking the first term of an expansion at $s_0^2/\sigma^2 = \infty$ one finds that

$$s_0 \approx \frac{\sigma\sqrt{2}}{\mathcal{O}_{S/N}\sqrt{N}}. \tag{8.21}$$

The value of s_0 needed to reach a given $\mathcal{O}_{S/N}$ scales with $1/\sqrt{N}$. Such result is equivalent to using linear propagation of errors.

However, in the case where $s_0^2/\sigma^2 \to 0$, the first term of the expansion at $s_0^2/\sigma^2 = 0$ produces the following relationship

$$s_0 \approx \frac{\sigma}{\sqrt{\mathcal{O}_{S/N}}N^{1/4}}. \tag{8.22}$$

The needed value of s_0 to reach a given $\mathcal{O}_{S/N}$ scales with $1/N^{1/4}$. This means that if a dark matter signal lies under the sensitivity limit, the sensitivity improves with further measurements only as $1/N^{1/4}$. A similar result is presented in Ref. [150] for an ALP search in Fourier space.

Additionally, if sensors have different directional sensitivities, an attenuation of $\mathcal{O}(0)$ is expected. The attenuation is given by

$$\mathcal{O}(0) \to \left(\cos\vartheta_{AB}/3\right)\mathcal{O}(0), \tag{8.23}$$

where ϑ_{AB} is the angle between the sensitive axes of the two sensors. A formal derivation of this effect can be seen in Ref. [6] Appendix C.

8.4 ACCESSIBLE ALP PARAMETER SPACE

Atomic magnetometers can search for ALP fields by detecting Zeeman shifts caused by the interaction described in Eq. (8.7). The pseudo-magnetic field produced by this quadratic interaction is given by

$$\mathcal{B}_q \approx \mp\frac{2\hbar^2c^2}{g_F\mu_B f_q^2}\boldsymbol{\nabla}\varphi^2(\boldsymbol{r},t)\,, \tag{8.24}$$

where g_F is the Landé factor, μ_B is the Bohr magneton (or, for nuclear-spin-based magnetometers, the nuclear magneton). The projection of the near-dc component of $\mathcal{B}_q$ along the sensitive axis of a magnetometer $\hat{\boldsymbol{n}}$ can be estimated by evaluating the sum in Eq. (8.8). Assuming that ω_{nm} and $\boldsymbol{k}_{nm}$ are uncorrelated, the sum can be split into two independent sums: $\Sigma_{nm}^{N}\boldsymbol{k}_{nm}$ and the sum of the sines. This is a good approximation for directions perpendicular to $\boldsymbol{v}_L$ (see Fig. 8.1). If the two sensors measure along the same direction, $\mathcal{O}(0)$ is equivalent to $\mathrm{Var}[\hat{\boldsymbol{n}} \cdot \boldsymbol{\mathcal{B}}_q]$. This can be related to the properties of the ALP field as

$$\mathcal{O}(0) \equiv \mathrm{Var}[\hat{\boldsymbol{n}} \cdot \boldsymbol{\mathcal{B}}_q] \sim \left(\frac{\hbar^3 \rho_{dm} v_0}{g_F \mu_B m_a f_q^2} \right)^2 . \tag{8.25}$$

In the derivation of the above equation the average spread of $\hat{\boldsymbol{n}} \cdot \boldsymbol{k}_{nm} \approx m_a v_0 / \hbar$. Factors of order one are omitted.

In order to estimate the sensitivity of a magnetometer network, consider N_m identical sensors having the same directional sensitivity and dominated by Gaussian noise with the same variance. This is not the case for real networks. Typically, the sensors feature different directional sensitivities and are affected by $1/f$ noise. Despite the simplification, this exercise serves to produce an estimate on the expected sensitivity of GNOME to the stochastic properties of the ALP field.

To evaluate the scaling of the sensitivity with N_m, τ_φ, and total acquisition time T, suppose that we divide the network into two distinct groups each with $N_m/2$ sensors and average the data in each group. Furthermore, suppose that the timeseries data are binned in τ_φ-long segments and time-averaged in each bin. Based on this approach, in the absence of a correlated signal, each group of sensors will exhibit a bin-to-bin variance in the measured magnetic field of approximately $\delta B / \sqrt{\tau_\varphi N_m / 2} \sim \delta B / \sqrt{\tau_\varphi N_m}$, where δB is the sensitivity of a single magnetometer in units of magnetic field strength times the square root of time. For a total acquisition time T, there will be $N_b = T / \tau_\varphi$ bins. This corresponds to the case studied in Eq. (8.22), where $\sigma^2 = \delta B^2 / (N_m \tau_\varphi)$ and N_b is the number of averages of $\mathcal{O}(0)$. The expected minimum measurable value of the observable between the two groups provides an estimate of the network resolution,

$$\mathcal{O}(0)_{\min} \approx \frac{\delta B^2}{N_m \tau_\varphi} \frac{1}{\sqrt{N_b}} \approx \frac{\delta B^2}{N_m \sqrt{\tau_\varphi T}} . \tag{8.26}$$

An in-depth discussion of the T and N_m scaling for a similar case can be found in Ref. [95].

Assuming that the minimum detectable signal in Eq. (8.26) is given by Eq. (8.25), a bound on the coupling constant to which a magnetometer network would be sensitive is given by

$$f_q^2 \lesssim \frac{\hbar^3 \rho_{dm} v_0}{g_F \mu_B m_\varphi \delta B} (\tau_\varphi T)^{1/4} \sqrt{N_m} . \tag{8.27}$$

Figure 8.3 shows sensitivity estimates for the Global Network of Optical Magnetometers for Exotic physics searches (GNOME) based on alkali vapor magnetometers with $\delta B \approx 100\,\mathrm{fT}/\sqrt{\mathrm{Hz}}$ and the Advanced GNOME network based on noble gas comagnetometers with $\delta B \approx 1\,\mathrm{fT}/\sqrt{\mathrm{Hz}}$, assuming $T = 100\,$days and $N_m = 10$. Note that for $\tau_c \gg 24\,$hours, the signal amplitude is partially modulated at the frequency of Earth's rotation since the signals are $\propto \hat{\boldsymbol{n}} \cdot \boldsymbol{\mathcal{B}}_q$ and $\hat{\boldsymbol{n}}$ rotates with the Earth while $\boldsymbol{\mathcal{B}}_q$ does not, which can in principle enable the detection of coherence times much longer than a day. Notable is the extent to which GNOME and Advanced GNOME can probe Compton frequencies far beyond the nominal sensor bandwidths. Ultimately, the sensitivity of sensor networks used to search for correlated dark matter signals may be limited by systematic effects due to prosaic natural phenomena. Known natural phenomena that could generate noise with long-range correlations include, for example, time-dependent electromagnetic fields associated with cavity resonances of the conducting Earth-ionosphere cavity [155] (such as the Schumann resonances [156]) and vibrational noise due to free oscillations of the Earth excited by large earthquakes [157] (such as the "breathing" mode of the Earth at $\approx 800\,\mu\mathrm{Hz}$ [158]). In the event of a non-null result, auxiliary measurements with other instruments may be able to rule out such systematic effects. For example, GNOME uses unshielded magnetometers to monitor the magnetic environment near the shielded dark matter sensors to veto signals from anomalously large local magnetic field excursions [120]. Additionally, as showed in Fig. 8.2, the coherence time of the ALP field has a dependence on the measurement axis relative to \$v_{\mathrm{L}}$. The characteristic daily and annual modulation of the coherence time due to Earth motion can be used to confirm an ALP signal.

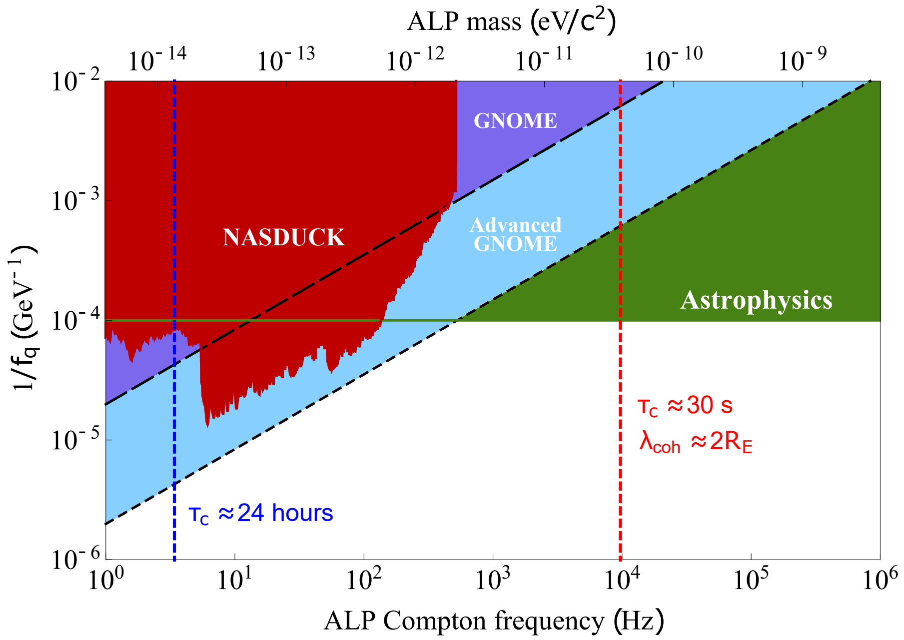

Figure 8.3: Estimated parameter space describing ALP dark matter that can be probed by GNOME and Advanced GNOME using intensity interferometry. GNOME is indicated by the dashed line and purple shaded region. Advanced GNOME is indicated by the dotted line and light blue shaded region. The estimation assumes ≈ 100 days of searching for correlated stochastic fluctuations using $N_m = 10$ magnetometers. GNOME and Advanced GNOME are sensitive to the interaction of the ALP field with proton spins described by Eq. (8.7); f_q parameterizes the ALP-fermion coupling strength. The vertical dashed red line marks the Compton frequency and mass for which the ALP coherence length equals the Earth's diameter, $\lambda_{coh} \approx 2R_E$, corresponding to a characteristic coherence time scale for fluctuations of $\nabla\varphi_s^2$ of $\tau_c \approx 30$ s. The vertical dashed blue line marks the Compton frequency and mass for which $\tau_c \approx 24$ hours; for m_a much smaller than this value, the pseudo-magnetic field is quasi-static in the galactic rest frame and thus the signals are frequency upconverted in the sensor network due to Earth's rotation. The dark red shaded region shows constraints from the Noble and Alkali Spin Detectors for Ultra-light Coherent darK matter (NASDUCK) experiment [152]. The dark green shaded area represents astrophysical bounds on spin-dependent ALP interactions with nucleons [138, 153]. Note, however, that there are theoretical scenarios where these astrophysical bounds can be circumvented [154], and thus laboratory searches are complementary to astrophysical observations.

9

CONCLUSIONS AND OUTLOOK

During this work the Global Network of Optical Magnetometers for Exotic physics searches was developed. Several coordinated calibrations and tests were carried out by the different members of the collaboration. These efforts culminated with several data acquisition campaigns. Here, the state of the network during Science Run 2 was described including the sensor physics, network characteristics and software employed for synchronization.

The main part of this thesis was devoted to the development of an analysis procedure to search for ALP domain walls. This resulted in the ALP parameter exclusion plot shown in Fig. 7.2. Several limitations were encountered during the process. On the hardware side, our sensors featured different bandwidths which perturbs a signal differently for each sensor. The use of a relatively long averaging time (20 s motivated by software limitations) limited the search to a frequency window in which the sensors respond equally. The magnetometers had frequent data streaming interruptions due to missing and flagged data. The analysis algorithm, however, requires continuous datasets to process the data efficiently. Since the measurement points are treated independently, data gaps could be filled with zeros for magnetic data and ones for noise data while flagging such points as insane. Then a continuous time-series could be processed. Since the added values were flagged, they were efficiently ignored. Late in the analysis, we realized that the calibration factors of the magnetometers were unreliable. An additional noise source proportional to the measured amplitude was added to the p-value calculation to account for this.

On the software side, different challenges were encountered. Signals from a domain wall crossing appear in the sensors at different times. Given a signal with unknown parameters one would need to explore all possible convolutions between the data streams to find the corresponding signals. This results in a m-dimensional convolution whose computational complexity scales as $\approx \mathcal{O}(n^m)$. Here, m is the number of magnetometers, n the number of points. Instead we decided to scan a fixed amount of domain wall velocities. These were determined by assuming that the dynamics of the domain walls are governed by the SHM. The sky coverage had to be dense enough to detect domain walls whose velocities lie between two scanning velocities. To ensure this, the number of velocities scales as $\mathcal{O}(\delta\tau^{-4})$, where $\delta\tau$ is the sampling period of the time-series (see Eqs. (6.2) and (6.3)). Such scaling forced the search to down-sample the data into 10 s periods to be processed within a manageable time. This scaling in the number of scanning velocities makes difficult an increase of the bandwidth in the search. The number of scanning velocities must be greatly increased to be sensitive to shorter signal durations.

An additional limitation is derived from the discrete scanning of the possible domain wall velocities. The required density in the scanning velocities not only dependents on the duration of the domain walls but also on the amplitude. If the velocity of a domain wall do not exactly correspond to a scanning velocity, the overlap of the signal peaks is not exact. Therefore, the p-value calculation is performed with values taken slightly off from the peak center. This produces an error proportional to the amplitude. As a consequence large amplitudes are misidentified (they produce small p-values). However, since the calibration error added an ad-hoc uncertainty proportional to the amplitude, this issue was circumvented. The possibility of using the supercomputer facilities in Mainz to increase the density of the scanning velocities was explored. However, with the mentioned scaling, no significant improvement was expected.

A Monte Carlo method was employed to numerically evaluate the sensitivity of GNOME to domain walls in Fig. 6.7. This study was compared to a theoretical estimation of the sensitivity based on the magnetometers average noise. These two approaches agreed which assured that the algorithm was working properly.

Despite all the efforts, it was disappointing to discover that SR 2 data is unable to claim a discovery due to the high rate of large magnitude-to-uncertainty events in the background (see Fig. 6.8). The background seem to approach a constant rate of events for large magnitude-to-uncertainty ratios. Extrapolation of the background to larger magnitude-to-uncertainty ratios will not considerably improve the significance of a detection.

The bounds on ALPs by the domain wall search set a milestone for GNOME being the first exotic physics constraints published by the collaboration. Nevertheless, the search procedure has room for improvement. A detailed study on the optimal position and orientation of additional magnetometers in GNOME has been published in Ref. [126]. More sensors and better sensitivity increase the detection probability for smaller domain wall magnitudes. Sensors with higher long term stability improve sensitivity to longer domain walls while a higher bandwidth improves sensitivity to shorter domain walls. Optimized software solutions are needed to extract the full potential of the sensors.

Improvements in sensitivity and bandwidth of the network are explored in Fig. 9.1a. The figure shows the expected detection probability. Inside the colored area it is $100\,\%$ and outside $0\,\%$. The influence of these improvements on the sensitivity to the ALP parameter space is plot in Fig. 9.1b. The accessible parameter space expands to smaller ξ by increasing network sensitivity or bandwidth to higher frequencies. Increasing bandwidth to lower frequencies, expands the accessible parameter space to lower masses and larger ξ. Note that improvements on the sensors do not increase the maximum f_{int} detectable for a given m_a and ξ. Greater sensitivity to f_{int} is accomplished with the square root of the measuring time as can be seen in Eq. (5.23). Even if the sensitivity to f_{int} is not improved with sensor improvements, a greater area of the parameter space can be covered. This is of critical importance because the specific combination of parameters allowing domain walls is uncertain.

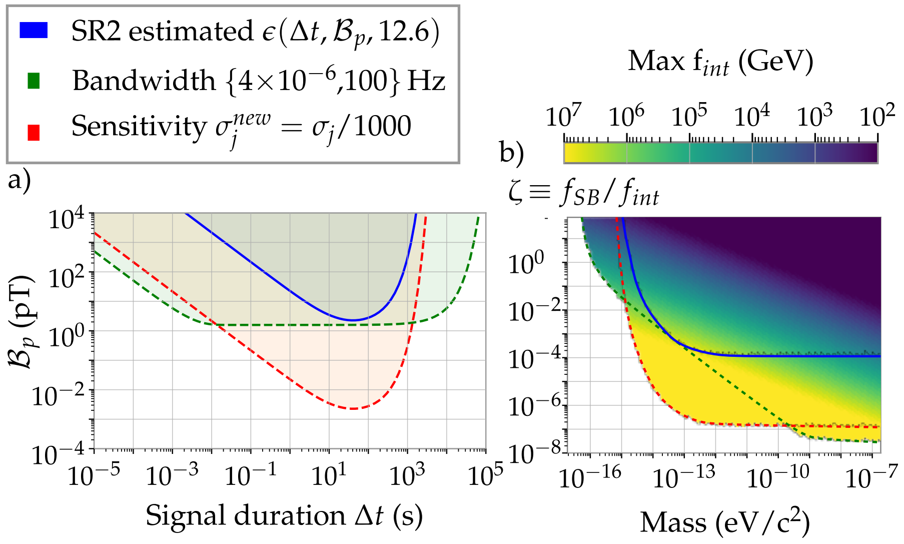

Figure 9.1: Projected exclusion plot for different improvements in the GNOME sensors. a) Estimated detection probability. Blue shows current SR2 estimation. Green improves on the bandwidth of the network and assumes it to be from 4×10^{-6} Hz (3 days period) to 100 Hz. Red improves on the sensitivity of each sensor by three orders of magnitude. b) Shows the effect of the improvements in the ALP parameter exclusion plot using the same color-code.

Looking into the future, the collaboration will focus both, on upgrades to the experimental apparatuses as well as on new data-analysis strategies. An ongoing challenge is posed by the overall reliability and continuous operation of the sensors. This has been partially solved by using Quspin commercial magnetometers. These sensors probed reliable continuous operation for over a week. Additionally, periodic pulses have been implemented to monitor changes in sensitivity and bandwidth of each sensor during continuous data taking. These periodic pulses monitor the magnetic field sensitivity of the sensors and allow the re-calibration of the data. Since very slow frequency signals (< 1/day) could be of scientific interest, the collaboration aims to reduce long term noise sources, increase the time in which the sensors operate uninterrupted, and explore different calibration pulse strategies.

A great leap for the network sensitivity to exotic spin couplings will be the wide implementation of noble-gas-based comagnetometers [159, 160] (Advanced GNOME). The high sensitivity of such devices to the nuclear spin is expected to greatly improve the performance of the network. SERF and NMOR magnetometers are sensitive to perturbations to the total atomic angular momentum. In contrast, comagnetometers are sensitive to the nuclear spin. In addition, they are insensitive to magnetic fields which is expected to considerably reduce the noise background. However, a comagnetometer is challenging to set-up. The relevant operation regime for exotic field detection is the self-compensation regime. The response to magnetic fields of two atomic species present in the cell compensate each other. In order to have a stable self-compensation operation, magnetic field gradients have to be sufficiently suppressed. Appropriate vapor cells for comagnetometry are not broadly available, since a specific gas mixture at high pressure is required. An important point for reliable operation of the GNOME sensors is a periodic calibration pulse. However, a calibration strategy for the comagnetometers within GNOME is still in development. An equivalent response to exotic couplings could be simulated by rotation of the setup since comagnetometers can also act as precision gyroscopes. Solutions to these challenges are currently being developed.

The presented algorithm could be applied out-of-the-box to later runs. However, we are eager to include improvements. The periodic calibration pulses remove the need for the calibration error since the sensitivity is hourly tracked. However, by removing the calibration error, large signals are misidentified. The bandwidth of the sensors was increased and homogenized in latter runs, therefore the bandwidth of the search can be improved towards shorter domain wall durations.

To include such hardware improvements in the search, the algorithm has to be updated upon our experience. The presented version has three main drawbacks. The discretization of the delays imposed by the velocity scanning hinders the correct identification of domain walls with large amplitudes. The scaling of the required density of points in the velocity scanning makes it difficult to search for short duration domain walls. Finally, the algorithm applies the whole analysis to all downsampled points which may mean that many irrelevant points are considered.

A possible way to accelerate the code is to implement simple conditions to pre-select relevant points. An approach being developed at the moment is based on the search for peaks surpassing the neighboring data (prominence) by a certain number of standard deviations of the noise ($\sim 3\sigma$) at each magnetometer. Then, if peaks appear within a ~ 4.5 minutes time window [1] in more than four magnetometers such group of peaks is selected for further analysis. This pre-selection process is fast and drastically reduces the number of points to be processed. Additionally, this peak search already provides the times of signals most probably belonging to the same domain wall crossing. Therefore the necessity for scanning all possible domain walls velocities is circumvented. The reduction of the points to be scrutinized would allow the increase of the sample rate of the search or a more accurate characterization. Within the GNOME collaboration a machine-learning-based algorithm was developed to perform a global fit to the network data [161]. In contrast to the fitting procedure used here, the machine-learning-based algorithm is able to fit the complete domain wall crossing model to a time series. The complete line-shapes are fitted and no estimated delays are required. Applying the algorithm to the whole data-set is not practical due to the computer processing required. However, it can be applied to a

---

[1] This is an upper bound for coincident signals given by the minimum domain wall speed considered in Fig. 5.1 (47 km/s) and the diameter of Earth ($\sim 1.2 \times 10^3$ km)

reduced number of data segment in which the coincidence search identified a candidate. Such combination could accomplish a more stringent identification and characterization of candidate events.

An ambitious goal of the GNOME collaboration is the implementation of a model-independent coincidence search for transient signals that operates in real time. In principle, an encounter with a dark matter structure is expected to leave a characteristic signal shape in each magnetometer. It would also produce a characteristic signal pattern in the network within a time window which can be estimated based on the SHM. These two facts could be used to generally search for dark matter related transients. Recently, machine learning techniques for data analysis are being broadly available. Algorithms to identify anomalies in time-series data have been developed. Such algorithms can identify anomalies in the data, not only based on their amplitude but also considering their shape though multiple observations, and their rarity (see Ref. [162] and references herein). After identifying anomalous events, time coincidence within the network can be exploited to extract interesting global events. Such ideas can be explored and implemented in the future to accomplish a model-independent coincidence search with GNOME.

The great potential of GNOME arises from the large range of cosmological dark matter models that it can probe. GNOME data can be searched for signatures of physics beyond the Standard Model such as boson stars [4], relaxion halos [143], stochastic fluctuations of a bosonic dark matter field [6], bursts of exotic low-mass fields from black-hole mergers [163] and more. Several of such analyses are already being carried out by the GNOME collaboration.

Part I

APPENDIX

A

TABLES OF SYMBOLS

Table A.1: List of constants relevant for the domain wall search.

Symbol	Value	Description
$\hbar$	6.582×10^{-16} eV s	Reduced Plank constant.
c	299792458 m/s	Speed of light.
μ_B	5.788×10^{-5} eV/T	Bohr magneton.
ρ_{dw}	0.4 GeV/cm^3	Domain wall energy density.
ρ_{dm}	0.3 GeV/cm^3	Local dark matter energy density [129].
$R_\oplus$	6378 km	Earth radius.
g_F^j	See Table 4.3	Landé g-factor for magnetometer j and hyperfine level F.
$\sigma_{p,F}$	See Table 4.3	Fractional proton spin polarization.
$\langle\sigma_p\rangle_{hf}$	See Table 4.3	Average fractional proton spin polarization over the hyperfine states. Relevant for SERF magnetometers.
$\bar{v}$	300 km/s	Expected domain wall speed.
v_0	220 km/s	Local velocity spread of the dark matter halo.
v_L	220 km/s	Earth speed with respect to the center of the Galaxy.
v_e	544 km/s	Galactic escape speed.

Table A.2: List of analysis parameters relevant for the domain wall search.

Symbol	Value	Description
j		Indexes the magnetometers in GNOME.
$\hat{\boldsymbol{n}}$		Directional sensitivity of a magnetometer.
$\hat{\boldsymbol{n}}_{\text{dw}}$		ALP domain wall direction.
$\hat{\boldsymbol{n}}_{\text{scan}}$		Direction in the scanning lattice.
δv	Speed dependent	Speed step in the scanning lattice.
$\delta\theta$	Speed dependent	Angle step in the scanning lattice.
θ_{rel}	0 to $\pi\,\text{rad}$	Angle between $\boldsymbol{v}_{\text{L}}$ and $\hat{\boldsymbol{n}}_{\text{dw}}$.
$\boldsymbol{v}_{\perp}$	47 to $770\,\text{km/s}$	Velocity component perpendicular to the plane of a domain wall.
ε_{s}	$97.5\,\%$	Fraction of domain wall velocities.
θ_{dw}		Angle between $\hat{\boldsymbol{n}}$ and $\hat{\boldsymbol{n}}_{\text{dw}}$.
$\theta_{\text{diff}}/\delta\theta$	< 3.5	Normalized angle between $\hat{\boldsymbol{n}}_{\text{scan}}$ and $\hat{\boldsymbol{n}}_{\text{dw}}$.
p-value	> 0.001	Quantifies the agreement with domain wall.
ζ		Magnitude-to-uncertainty ratio of an event´.
ζ_{max}	12.6	Maximum magnitude-to-uncertainty measured.
B_j		Pseudo-magnetic field. Local magnetic response to an ALP domain wall.
$\mathcal{B}_{\text{p}}$		Normalized pseudo-magnetic field. Magnetic field phenomenologically describing a domain wall.
Δt		Domain wall signal duration.
Δx		Spatial extension of the domain wall.
$\epsilon(\Delta t, \mathcal{B}_{\text{p}}', \zeta)$		Detection probability.
C	$> 90\,\%$	Confidence level on the constraints.
r		Expected rate of events.
R_C		Data driven bound on the event rate.
T	$23\,\text{days}$	Duration of science run 2.
		direction and the estimated direction.
T_{avg}	$20\,\text{s}$	Averaging time
T_{b}	$10.7\,\text{years}$	Duration of simulated background.
$n_{\text{b}}(\zeta)$		Number of background events above ζ

Table A.3: List of parameter in the domain wall fitting.

Symbol	Value	Description
D		Matrix containing the directional sensitivities of the sensors
$\boldsymbol{m}$		Pseudo-magnetic field associated with an event
$\boldsymbol{\mu}$		Pseudo-magnetic field expected at each magnetometer
$\boldsymbol{s}$		Measurement time series
$\boldsymbol{s}_\sigma$		Noise estimation time-series
Σ_s		Covariance matrix of $\boldsymbol{s}$.
Σ_m		Covariance matrix of $\boldsymbol{m}$.

Table A.4: List of ALP parameters relevant for the domain wall search.

Symbol	Value	Description
a		Axion-like particle(ALP) field
m_a		Axion-like particle(ALP) mass
f_{SB}		Symmetry breaking scale. Energy scale at which the ALP acquires mass.
$\bar{L}$		Average characteristic domain size.
f_{int}		Interaction scale. Energy scale governing the interaction to protons
ξ	f_{SB}/f_{int}	Ratio between symmetry breaking and interaction constants

BIBLIOGRAPHY

[1] S. Afach et al. *What can a GNOME do? Search targets for the Global Network of Optical Magnetometers for Exotic physics searches*. 2023. arXiv: `2305.01785 [hep-ph]`.

[2] M. Pospelov, S. Pustelny, M. P. Ledbetter, D. F. Jackson Kimball, W. Gawlik, and D. Budker. “Detecting Domain Walls of Axionlike Models Using Terrestrial Experiments.” In: *Phys. Rev. Lett.* 110 (2013), p. 021803.

[3] Samer Afach et al. “Search for topological defect dark matter with a global network of optical magnetometers.” In: *Nature Physics* 17.12 (Dec. 2021), pp. 1396–1401. ISSN: 1745-2481. DOI: `10.1038/s41567-021-01393-y`. URL: `https://doi.org/10.1038/s41567-021-01393-y`.

[4] DF Jackson Kimball, D Budker, J Eby, M v, Szymon Pustelny, Theo Scholtes, YV Stadnik, Antoine Weis, and A Wickenbrock. “Searching for axion stars and Q-balls with a terrestrial magnetometer network.” In: *Phys. Rev. D* 97.4 (2018), p. 043002.

[5] G. P. Centers et al. “Stochastic fluctuations of bosonic dark matter.” In: *Nature communications* 12 (2021), p. 7321.

[6] Hector Masia-Roig et al. “Intensity interferometry for ultralight bosonic dark matter detection.” In: (Feb. 2022). arXiv: `2202.02645 [hep-ph]`.

[7] Dorota M. Grabowska, Tom Melia, and Surjeet Rajendran. “Detecting dark blobs.” In: *Phys. Rev. D* 98 (11 Dec. 2018), p. 115020. DOI: `10.1103/PhysRevD.98.115020`. URL: `https://link.aps.org/doi/10.1103/PhysRevD.98.115020`.

[8] Nataniel L Figueroa, Dmitry Budker, and Ernst M Rasel. “Dark matter searches using accelerometer-based networks.” In: *Quantum Science and Technology* 6.3 (May 2021), p. 034004. DOI: `10.1088/2058-9565/abef4f`. URL: `https://doi.org/10.1088/2058-9565/abef4f`.

[9] Kiwoon Choi, Sang Hui Im, and Chang Sub Shin. “Recent Progress in the Physics of Axions and Axion-Like Particles.” In: *Annual Review of Nuclear and Particle Science* 71.1 (2021), pp. 225–252. DOI: `10.1146/annurev-nucl-120720-031147`. eprint: `https://doi.org/10.1146/annurev-nucl-120720-031147`. URL: `https://doi.org/10.1146/annurev-nucl-120720-031147`.

[10] L. D. Duffy and K. van Bibber. “Axions as dark matter particles.” In: *New J. Phys.* 11 (2009), p. 105008.

[11] Roberto D Peccei and Helen R Quinn. “CP Conservation in the Presence of Instantons.” In: *Phys. Rev. Lett.* 38 (1977), pp. 1440–1443.

[12] C. Abel et al. “Measurement of the Permanent Electric Dipole Moment of the Neutron.” In: *Phys. Rev. Lett.* 124 (8 Feb. 2020), p. 081803. DOI: 10.1103/PhysRevLett.124.081803. URL: https://link.aps.org/doi/10.1103/PhysRevLett.124.081803.

[13] J. Preskill, M. B. Wise, and F. Wilczek. “Cosmology of the invisible axion.” In: *Phys. Lett. B* 120 (1983), p. 127.

[14] Giovanni Grilli di Cortona, Edward Hardy, Javier Pardo Vega, and Giovanni Villadoro. “The QCD axion, precisely.” In: *Journal of High Energy Physics* 2016.1 (Jan. 2016), p. 34. ISSN: 1029-8479. DOI: 10.1007/JHEP01(2016)034. URL: https://doi.org/10.1007/JHEP01(2016)034.

[15] P Sikivie. “Axions, domain walls, and the early universe.” In: *Phys. Rev. Lett.* 48.17 (1982), p. 1156.

[16] P. W. Graham and S. Rajendran. “New observables for direct detection of axion dark matter.” In: *Phys. Rev. D* 88 (2013), p. 035023.

[17] C. Bartram et al. “Search for Invisible Axion Dark Matter in the $3.3--4.2\ \mu$eV Mass Range.” In: *Phys. Rev. Lett.* 127 (26 Dec. 2021), p. 261803. DOI: 10.1103/PhysRevLett.127.261803. URL: https://link.aps.org/doi/10.1103/PhysRevLett.127.261803.

[18] K. M. Backes et al. “A quantum enhanced search for dark matter axions.” In: *Nature* 590.7845 (Feb. 2021), pp. 238–242. ISSN: 1476-4687. DOI: 10.1038/s41586-021-03226-7. URL: https://doi.org/10.1038/s41586-021-03226-7.

[19] C. Abel et al. “Search for Axionlike Dark Matter through Nuclear Spin Precession in Electric and Magnetic Fields.” In: *Phys. Rev. X* 7 (4 Nov. 2017), p. 041034. DOI: 10.1103/PhysRevX.7.041034. URL: https://link.aps.org/doi/10.1103/PhysRevX.7.041034.

[20] Deniz Aybas et al. “Search for Axionlike Dark Matter Using Solid-State Nuclear Magnetic Resonance.” In: *Phys. Rev. Lett.* 126 (14 Apr. 2021), p. 141802. DOI: 10.1103/PhysRevLett.126.141802. URL: https://link.aps.org/doi/10.1103/PhysRevLett.126.141802.

[21] J. Jaeckel, G. Rybka, and L. Winslow. *Axion Dark Matter*. 2022. DOI: 10.48550/ARXIV.2203.14923. URL: https://arxiv.org/abs/2203.14923.

[22] Pierluca Carenza, Tobias Fischer, Maurizio Giannotti, Gang Guo, Gabriel Martínez-Pinedo, and Alessandro Mirizzi. “Improved axion emissivity from a supernova via nucleon-nucleon bremsstrahlung.” In: *Journal of Cosmology and Astroparticle Physics* 2019.10 (Oct. 2019), p. 016. DOI: 10.1088/1475-7516/2019/10/016.

[23] Malte Buschmann, Christopher Dessert, Joshua W. Foster, Andrew J. Long, and Benjamin R. Safdi. "Upper Limit on the QCD Axion Mass from Isolated Neutron Star Cooling." In: *Phys. Rev. Lett.* 128 (9 Mar. 2022), p. 091102. DOI: `10.1103/PhysRevLett.128.091102`. URL: `https://link.aps.org/doi/10.1103/PhysRevLett.128.091102`.

[24] Aagaman Bhusal, Nick Houston, and Tianjun Li. "Searching for Solar Axions Using Data from the Sudbury Neutrino Observatory." In: *Phys. Rev. Lett.* 126 (9 Mar. 2021), p. 091601. DOI: `10.1103/PhysRevLett.126.091601`. URL: `https://link.aps.org/doi/10.1103/PhysRevLett.126.091601`.

[25] J. E. Moody and F. Wilczek. "New macroscopi forces?" In: *Phys. Rev. D* 30 (1984), p. 130.

[26] Pavel Fadeev, Yevgeny V Stadnik, Filip Ficek, Mikhail G Kozlov, Victor V Flambaum, and Dmitry Budker. "Revisiting spin-dependent forces mediated by new bosons: Potentials in the coordinate-space representation for macroscopic-and atomic-scale experiments." In: *Phys. Rev. A* 99.2 (2019), p. 022113.

[27] Asimina Arvanitaki and Andrew A. Geraci. "Resonantly Detecting Axion-Mediated Forces with Nuclear Magnetic Resonance." In: *Phys. Rev. Lett.* 113 (16 Oct. 2014), p. 161801. DOI: `10.1103/PhysRevLett.113.161801`. URL: `https://link.aps.org/doi/10.1103/PhysRevLett.113.161801`.

[28] Yuanhong Wang et al. "Limits on Axions and Axionlike Particles within the Axion Window Using a Spin-Based Amplifier." In: *Phys. Rev. Lett.* 129 (5 July 2022), p. 051801. DOI: `10.1103/PhysRevLett.129.051801`. URL: `https://link.aps.org/doi/10.1103/PhysRevLett.129.051801`.

[29] Attaallah Almasi, Junyi Lee, Himawan Winarto, Marc Smiciklas, and Michael V. Romalis. "New Limits on Anomalous Spin-Spin Interactions." In: *Phys. Rev. Lett.* 125 (20 Nov. 2020), p. 201802. DOI: `10.1103/PhysRevLett.125.201802`. URL: `https://link.aps.org/doi/10.1103/PhysRevLett.125.201802`.

[30] Norman F Ramsey. "The tensor force between two protons at long range." In: *Physica A: Statistical Mechanics and its Applications* 96.1-2 (1979), pp. 285–289.

[31] G. Vasilakis, J. M. Brown, T. W. Kornack, and M. V. Romalis. "Limits on New Long Range Nuclear Spin-Dependent Forces Set with a K-^{3}He Comagnetometer." In: *Phys. Rev. Lett.* 103 (2009), p. 261801.

[32] D. F. Jackson Kimball. "Nuclear spin content and constraints on exotic spin-dependent couplings." In: *New J. Phys.* 17 (2015), p. 073008.

[33] Teng Wu, John W Blanchard, Gary P Centers, Nataniel L Figueroa, Antoine Garcon, Peter W Graham, Derek F Jackson Kimball, Surjeet Rajendran, Yevgeny V Stadnik, Alexander O Sushkov, et al. "Search for axionlike dark matter with a liquid-state nuclear spin comagnetometer." In: *Phys. Rev. Lett.* 122.19 (2019), p. 191302.

[34] Antoine Garcon, John W Blanchard, Gary P Centers, Nataniel L Figueroa, Peter W Graham, Derek F Jackson Kimball, Surjeet Rajendran, Alexander O Sushkov, Yevgeny V Stadnik, Arne Wickenbrock, et al. "Constraints on bosonic dark matter from ultralow-field nuclear magnetic resonance." In: *Science advances* 5.10 (2019), eaax4539.

[35] Itay M. Bloch, Roy Shaham, Yonit Hochberg, Eric Kuflik, Tomer Volansky, and Or Katz. *NASDUCK SERF: New constraints on axion-like dark matter from a SERF comagnetometer*. 2022. DOI: `10.48550/ARXIV.2209.13588`. URL: `https://arxiv.org/abs/2209.13588`.

[36] Hector Masia-Roig et al. "Analysis method for detecting topological defect dark matter with a global magnetometer network." In: *Phys. Dark Universe* 28 (May 2020), p. 100494. ISSN: 22126864. DOI: `10.1016/j.dark.2020.100494`. URL: `https://linkinghub.elsevier.com/retrieve/pii/S2212686419303760` (visited on 02/17/2020).

[37] Ciaran O'Hare. *cajohare/AxionLimits: AxionLimits*. `https://cajohare.github.io/AxionLimits/`. Version v1.0. July 2020. DOI: `10.5281/zenodo.3932430`.

[38] S. Afach et al. "Characterization of the global network of optical magnetometers to search for exotic physics (GNOME)." In: *Physics of the Dark Universe* 22 (2018), pp. 162–180. ISSN: 2212-6864. DOI: `https://doi.org/10.1016/j.dark.2018.10.002`. URL: `https://www.sciencedirect.com/science/article/pii/S2212686418301031`.

[39] B P Abbott et al. "Direct Observation of Gravitational Waves from a Binary Black Hole Merger." In: *Phys. Rev. Lett.* 116.6 (2016), p. 61102. ISSN: 0031-9007. DOI: `10.1103/PhysRevLett.116.061102`. arXiv: `1602.03837`. URL: `http://link.aps.org/doi/10.1103/PhysRevLett.116.061102`.

[40] R.L. Workman et al. "Dark Matter." In: (). to be published (2022).

[41] Kimmo Tuominen. "Cold Particle Dark Matter." In: *Symmetry* 13.10 (2021). ISSN: 2073-8994. DOI: `10.3390/sym13101945`. URL: `https://www.mdpi.com/2073-8994/13/10/1945`.

[42] Andrei Derevianko. "Atomic clocks and dark-matter signatures." In: *Journal of Physics: Conference Series* 723 (June 2016), p. 012043. DOI: `10.1088/1742-6596/723/1/012043`. URL: `https://doi.org/10.1088/1742-6596/723/1/012043`.

[43] Jeppe Trøst Nielsen, Alberto Guffanti, and Subir Sarkar. "Marginal evidence for cosmic acceleration from Type Ia supernovae." In: *Nature Publishing Group* (2015), p. 5. ISSN: 2045-2322. DOI: `10.1038/srep35596`. arXiv: `1506.01354`.

[44] Colin, Jacques, Mohayaee, Roya, Rameez, Mohamed, and Sarkar, Subir. "Evidence for anisotropy of cosmic acceleration." In: *A&A* 631 (2019), p. L13. DOI: `10.1051/0004-6361/201936373`. URL: `https://doi.org/10.1051/0004-6361/201936373`.

[45] MS Safronova, D Budker, D DeMille, Derek F Jackson Kimball, A Derevianko, and Charles W Clark. "Search for new physics with atoms and molecules." In: *Rev. Mod. Phys.* 90.2 (2018), p. 025008.

[46] L. F. Abbott and P. Sikivie. "A cosmological bound on the invisible axion." In: *Phys. Lett. B* 120 (1983), p. 133.

[47] M. Dine and W. Fischler. "The not-so-harmless axion." In: *Phys. Lett. B* 120 (1983), p. 137.

[48] P. W. Graham, D. E. Kaplan, and S. Rajendran. "Cosmological Relaxation of the Electroweak Scale." In: *Phys. Rev. Lett.* 115 (2015), p. 221801.

[49] Raymond T Co, Lawrence J Hall, and Keisuke Harigaya. "Predictions for Axion Couplings from ALP Cogenesis." In: *arXiv:2006.04809* (2020).

[50] F. Zwicky. "On the Masses of Nebulae and of Clusters of Nebulae." In: *The Astrophysical Journal* 86 (1937), p. 217. DOI: `10.1086/143864`. arXiv: `1937ApJ....86..217Z`.

[51] Y. Sofue and V. Rubin. "Rotation Curves of Spiral Galaxies." In: *Annu. Rev. Astron. Astrophys.* 39 (2001), p. 137.

[52] Stacy McGaugh. "Predictions and Outcomes for the Dynamics of Rotating Galaxies." In: *Galaxies* 8.2 (2020). ISSN: 2075-4434. DOI: `10.3390/galaxies8020035`. URL: `https://www.mdpi.com/2075-4434/8/2/35`.

[53] E. Pécontal, T. Buchert, Ph. Di Stefano, Y. Copin, and K. Freese. "Review of Observational Evidence for Dark Matter in the Universe and in upcoming searches for Dark Stars." In: *European Astronomical Society Publications Series* 36 (2009), pp. 113–126. DOI: `10.1051/eas/0936016`.

[54] Volker Springel et al. "Simulations of the formation, evolution and clustering of galaxies and quasars." In: *Nature* 435.7042 (2005), pp. 629–636. ISSN: 0028-0836. DOI: `10.1038/nature03597`. arXiv: `0504097 [astro-ph]`.

[55] Maxim Markevitch, Anthony H. Gonzalez, D. Clowe, Alexey Vikhlinin, Laurence P. David, William R. Forman, Christine Jones, Stephen S. Murray, and W. Tucker. "Direct constraints on the dark matter self-interaction cross-section from the merging galaxy cluster 1E0657-56." In: *The Astrophysical Journal* 606.2 (2003), p. 6. ISSN: 0004-637X. DOI: `10.1086/383178`. arXiv: `0309303 [astro-ph]`.

[56] Douglas Clowe, Maruša Bradač, Anthony H. Gonzalez, Maxim Markevitch, Scott W. Randall, Christine Jones, and Dennis Zaritsky. “A Direct Empirical Proof of the Existence of Dark Matter.” In: *The Astrophysical Journal* 648.2 (2006), pp. L109–L113. DOI: 10.1086/508162. arXiv: 0608407 [astro-ph].

[57] R Massey, T Kitching, and J Richard. “The dark matter of gravitational lensing.” In: *Reports on Progress in Physics* 73.8 (2010), pp. 086901–+. DOI: 10.1088/0034-4885/73/8/086901. arXiv: 1001.1739 [astro-ph.CO].

[58] Planck Collaboration et al. “Planck 2018 results - VI. Cosmological parameters.” In: *A&A* 641 (2020), A6. DOI: 10.1051/0004-6361/201833910. URL: https://doi.org/10.1051/0004-6361/201833910.

[59] A. Einstein. “Die Grundlage der allgemeinen Relativitätstheorie.” In: *Annalen der Physik* 354.7 (1916), pp. 769–822. DOI: https://doi.org/10.1002/andp.19163540702. eprint: https://onlinelibrary.wiley.com/doi/pdf/10.1002/andp.19163540702. URL: https://onlinelibrary.wiley.com/doi/abs/10.1002/andp.19163540702.

[60] Frank Watson Dyson, Arthur Stanley Eddington, and C. Davidson. “IX. A determination of the deflection of light by the sun’s gravitational field, from observations made at the total eclipse of May 29, 1919.” In: *Philosophical Transactions of the Royal Society of London. Series A, Containing Papers of a Mathematical or Physical Character* 220.571-581 (1920), pp. 291–333. DOI: 10.1098/rsta.1920.0009. eprint: https://royalsocietypublishing.org/doi/pdf/10.1098/rsta.1920.0009. URL: https://royalsocietypublishing.org/doi/abs/10.1098/rsta.1920.0009.

[61] Albert Einstein. “Lens-Like Action of a Star by the Deviation of Light in the Gravitational Field.” In: *Science* 84.2188 (1936), pp. 506–507. DOI: 10.1126/science.84.2188.506. eprint: https://www.science.org/doi/pdf/10.1126/science.84.2188.506. URL: https://www.science.org/doi/abs/10.1126/science.84.2188.506.

[62] Yiannis Tsapras. “Microlensing Searches for Exoplanets.” In: *Geosciences* 8.10 (2018). ISSN: 2076-3263. DOI: 10.3390/geosciences8100365. URL: https://www.mdpi.com/2076-3263/8/10/365.

[63] P. Popowski et al. “Microlensing Optical Depth toward the Galactic Bulge Using Clump Giants from the MACHO Survey.” In: *The Astrophysical Journal* 631.2 (Oct. 2005), pp. 879–905. DOI: 10.1086/432246. URL: https://doi.org/10.1086/432246.

[64] Richard J. Massey et al. “Dark matter maps reveal cosmic scaffolding.” In: *Nature* 445 (2007), pp. 286–290.

[65] Massimo Meneghetti et al. “An excess of small-scale gravitational lenses observed in galaxy clusters.” In: *Science* 369.6509 (2020), pp. 1347–1351. DOI: `10.1126/science.aax5164`. eprint: `https://www.science.org/doi/pdf/10.1126/science.aax5164`. URL: `https://www.science.org/doi/abs/10.1126/science.aax5164`.

[66] Rachel Mandelbaum, Uroš Seljak, Guinevere Kauffmann, Christopher M. Hirata, and Jonathan Brinkmann. “Galaxy halo masses and satellite fractions from galaxy–galaxy lensing in the Sloan Digital Sky Survey: stellar mass, luminosity, morphology and environment dependencies.” In: *Monthly Notices of the Royal Astronomical Society* 368.2 (Apr. 2006), pp. 715–731. ISSN: 0035-8711. DOI: `10.1111/j.1365-2966.2006.10156.x`. eprint: `https://academic.oup.com/mnras/article-pdf/368/2/715/3077507/mnras0368-0715.pdf`. URL: `https://doi.org/10.1111/j.1365-2966.2006.10156.x`.

[67] August E. Evrard. “Well of darkness.” In: *Nature* 394.6689 (1998), pp. 122–123. URL: `https://EconPapers.repec.org/RePEc:nat:nature:v:394:y:1998:i:6689:d:10.1038_28034`.

[68] Gianfranco Bertone, Dan Hooper, and Joseph Silk. “Particle dark matter: Evidence, candidates and constraints.” In: *Physics Reports* 405.5-6 (2005), pp. 279–390. DOI: `10.1016/j.physrep.2004.08.031`. arXiv: `0404175 [hep-ph]`.

[69] E. Aprile et al. “Dark Matter Search Results from a One Ton-Year Exposure of XENON1T.” In: *Phys. Rev. Lett.* 121 (11 Sept. 2018), p. 111302. DOI: `10.1103/PhysRevLett.121.111302`. URL: `https://link.aps.org/doi/10.1103/PhysRevLett.121.111302`.

[70] E. Aprile et al. “Light Dark Matter Search with Ionization Signals in XENON1T.” In: *Phys. Rev. Lett.* 123 (25 Dec. 2019), p. 251801. DOI: `10.1103/PhysRevLett.123.251801`. URL: `https://link.aps.org/doi/10.1103/PhysRevLett.123.251801`.

[71] E. Aprile et al. “Excess electronic recoil events in XENON1T.” In: *Phys. Rev. D* 102 (7 Oct. 2020), p. 072004. DOI: `10.1103/PhysRevD.102.072004`. URL: `https://link.aps.org/doi/10.1103/PhysRevD.102.072004`.

[72] Stephen J Asztalos, Leslie J Rosenberg, Karl van Bibber, Pierre Sikivie, and Konstantin Zioutas. “Searches for Astrophysical and Cosmological Axions*.” In: *Annual Review of Nuclear and Particle Science* 56.1 (2006), pp. 293–326. ISSN: 0163-8998. DOI: `10.1146/annurev.nucl.56.080805.140513`.

[73] P.A. Zyla et al. “Review of Particle Physics.” In: *PTEP* 2020.8 (2020), p. 083C01. DOI: `10.1093/ptep/ptaa104`.

[74] R. D. Peccei and Helen R. Quinn. “CP Conservation in the Presence of Pseudoparticles.” In: *Phys. Rev. Lett.* 38 (25 June 1977), pp. 1440–1443. DOI: `10.1103/PhysRevLett.38.1440`. URL: `https://link.aps.org/doi/10.1103/PhysRevLett.38.1440`.

[75] Steven Weinberg. “A New Light Boson?” In: *Phys. Rev. Lett.* 40 (4 Jan. 1978), pp. 223–226. DOI: 10.1103/PhysRevLett.40.223. URL: https://link.aps.org/doi/10.1103/PhysRevLett.40.223.

[76] F. Wilczek. “Problem of Strong P and T Invariance in the Presence of Instantons.” In: *Phys. Rev. Lett.* 40 (5 Jan. 1978), pp. 279–282. DOI: 10.1103/PhysRevLett.40.279. URL: https://link.aps.org/doi/10.1103/PhysRevLett.40.279.

[77] S. J. Asztalos et al. “Experimental Constraints on the Axion Dark Matter Halo Density.” In: *The Astrophysical Journal* 571.1 (2002), pp. L27–L30. ISSN: 0004637X. DOI: 10.1086/341130. arXiv: 0104200 [astro-ph].

[78] Igor G Irastorza and Javier Redondo. “New experimental approaches in the search for axion-like particles.” In: *Prog. Part. Nucl. Phys.* 102 (2018), p. 89.

[79] A Ringwald. “Axions and axion-like particles.” In: *Proceedings, 49th Rencontres de Moriond on Electroweak Interactions and Unified Theories: La Thuile, Italy, March 15-22, 2014, March 15-22, 2014*. 1. 2014, pp. 223–230. arXiv: 1407.0546. URL: https://inspirehep.net/record/1304441/files/arXiv:1407.0546.pdf.

[80] Yakov Boris Zel’dovich, I Yu Kobzarev, and Lev Borisovich Okun. “Cosmological consequences of spontaneous violation of discrete symmetry.” In: *Zh. Eksp. Teor. Fiz.* 40 (1974), p. 3.

[81] Alexander Vilenkin. “Gravitational field of vacuum domain walls and strings.” In: *Phys. Rev. D* 23.4 (1981), p. 852.

[82] A. Vilenkin. “Cosmic strings and domain walls.” In: *Phys. Rep.* 121 (1985), p. 263.

[83] A. Derevianko and M. Pospelov. “Hunting for topological dark matter with atomic clocks.” In: *Nat. Phys.* 10.12 (2014), p. 933.

[84] Masahiro Kawasaki, Ken’ichi Saikawa, and Toyokazu Sekiguchi. “Axion dark matter from topological defects.” In: *Phys. Rev. D* 91.6 (2015), p. 065014.

[85] D. J. Kaup. “Klein-Gordon Geon.” In: *Phys. Rev.* 172 (5 1968), p. 1331.

[86] E. Braaten, A. Mohapatra, and H. Zhang. “Dense Axion Stars.” In: *Phys. Rev. Lett.* 117 (2016), p. 121801.

[87] S. Coleman. “Q-balls.” In: *Nucl. Phys. B* 262 (1985), p. 263.

[88] A. Kusenko and P. J. Steinhardt. “Q-ball candidates for self-interacting dark matter.” In: *Phys. Rev. Lett.* 87 (2001), p. 141301.

[89] William H Press, Barbara S Ryden, and David N Spergel. “Dynamical evolution of domain walls in an expanding universe.” In: *Astrophys. J.* 347 (1989), p. 590.

[90] Martin Bucher and David Spergel. “Is the dark matter a solid?” In: *Phys. Rev. D* 60.4 (1999), p. 043505.

[91] PP Avelino, CJAP Martins, J Menezes, R Menezes, and JCRE Oliveira. "Dynamics of domain wall networks with junctions." In: *Phys. Rev. D* 78.10 (2008), p. 103508.

[92] Takashi Hiramatsu, Masahiro Kawasaki, Ken'ichi Saikawa, and Toyokazu Sekiguchi. "Axion cosmology with long-lived domain walls." In: *J. Cosmol. Astropart. Phys.* 2013.01 (2013), p. 001.

[93] Seungwon Baek, P Ko, and Wan-Il Park. "Hidden sector monopole, vector dark matter and dark radiation with Higgs portal." In: *J. Cosmol. Astropart. Phys.* 2014.10 (2014), p. 067.

[94] Joerg Jaeckel, Sebastian Schenk, and Michael Spannowsky. "Probing dark matter clumps, strings and domain walls with gravitational wave detectors." In: *arXiv:2004.13724* (2020).

[95] Andrei Derevianko. "Detecting dark-matter waves with a network of precision-measurement tools." In: *Phys. Rev. A* 97.4 (2018), p. 042506.

[96] Mariangela Lisanti, Matthew Moschella, and William Terrano. "Stochastic properties of ultralight scalar field gradients." In: *Phys. Rev. D* 104 (5 Sept. 2021), p. 055037. DOI: `10.1103/PhysRevD.104.055037`.

[97] William E. Bell and Arnold L. Bloom. "Optical Detection of Magnetic Resonance in Alkali Metal Vapor." In: *Phys. Rev.* 107 (6 Sept. 1957), pp. 1559–1565. DOI: `10.1103/PhysRev.107.1559`. URL: `https://link.aps.org/doi/10.1103/PhysRev.107.1559`.

[98] Elena Boto et al. "Moving magnetoencephalography towards real-world applications with a wearable system." In: *Nature* 555.7698 (Mar. 2018), pp. 657–661. ISSN: 1476-4687. DOI: `10.1038/nature26147`. URL: `https://doi.org/10.1038/nature26147`.

[99] Anne Fabricant, Geoffrey Z. Iwata, Sönke Scherzer, Lykourgos Bougas, Katharina Rolfs, Anna Jodko-Władzińska, Jens Voigt, Rainer Hedrich, and Dmitry Budker. "Action potentials induce biomagnetic fields in carnivorous Venus flytrap plants." eng. In: *Scientific reports* 11 (2021), p. 1438. ISSN: 2045-2322. DOI: `http://doi.org/10.25358/openscience-6319`. URL: `https://doi.org/10.1038/s41598-021-81114-w`.

[100] Kasper Jensen, Mark Alexander Skarsfeldt, Hans Stærkind, Jens Arnbak, Mikhail V. Balabas, Søren-Peter Olesen, Bo Hjorth Bentzen, and Eugene S. Polzik. "Magnetocardiography on an isolated animal heart with a room-temperature optically pumped magnetometer." In: *Scientific Reports* 8.1 (Nov. 2018), p. 16218. ISSN: 2045-2322. DOI: `10.1038/s41598-018-34535-z`. URL: `https://doi.org/10.1038/s41598-018-34535-z`.

[101] Yinan Hu, Geoffrey Z. Iwata, Lykourgos Bougas, John W. Blanchard, Arne Wickenbrock, Gerhard Jakob, Stephan Schwarz, Clemens Schwarzinger, Alexej Jerschow, and Dmitry Budker. "Rapid Online Solid-State Battery Diagnostics with Optically Pumped Magnetometers." In: *Applied Sciences* 10.21 (2020). ISSN:

2076-3417. DOI: 10.3390/app10217864. URL: https://www.mdpi.com/2076-3417/10/21/7864.

[102] Kasper Jensen, Michael Zugenmaier, Jens Arnbak, Hans Stærkind, Mikhail V. Balabas, and Eugene S. Polzik. "Detection of low-conductivity objects using eddy current measurements with an optical magnetometer." In: *Phys. Rev. Research* 1 (3 Nov. 2019), p. 033087. DOI: 10.1103/PhysRevResearch.1.033087. URL: https://link.aps.org/doi/10.1103/PhysRevResearch.1.033087.

[103] C.J. Foot, C.J.F. Foot, and D.P.C.J. Foot. *Atomic Physics*. Oxford Master Series in Physics. OUP Oxford, 2005. ISBN: 9780198506959.

[104] S. J. Seltzer. "Developments in Alkali-Metal Atomic Magnetometry." PhD thesis. Princeton University, 2008.

[105] Peter van der Straten and Harold Metcalf. *Atoms and Molecules Interacting with Light: Atomic Physics for the Laser Era*. Cambridge University Press, 2016. DOI: 10.1017/CBO9781316106242.

[106] M. Auzinsh, D. Budker, and S. Rochester. *Optically Polarized Atoms: Understanding Light-atom Interactions*. OUP Oxford, 2010. ISBN: 9780199565122.

[107] D. F. Jackson Kimball, J. Dudley, Y. Li, S. Thulasi, S. Pustelny, D. Budker, and M. Zolotorev. "Magnetic shielding and exotic spin-dependent interactions." In: *Phys. Rev. D* 94.8 (2016), p. 082005. DOI: 10.1103/PhysRevD.94.082005.

[108] Th. Schmidt. "Über die magnetischen Momente der Atomkerne." In: *Zeitschrift für Physik* 106.5 (May 1937), pp. 358–361. ISSN: 0044-3328. DOI: 10.1007/BF01338744. URL: https://doi.org/10.1007/BF01338744.

[109] Jonathan Engel and Petr Vogel. "Spin-dependent cross sections of weakly interacting massive particles on nuclei." In: *Phys. Rev. D* 40.9 (1989), p. 3132.

[110] VV Flambaum and AF Tedesco. "Dependence of nuclear magnetic moments on quark masses and limits on temporal variation of fundamental constants from atomic clock experiments." In: *Phys. Rev. C* 73.5 (2006), p. 055501.

[111] J Engel, MT Ressell, IS Towner, and WE Ormand. "Response of mica to weakly interacting massive particles." In: *Phys. Rev. C* 52.4 (1995), p. 2216.

[112] P Toivanen, M Kortelainen, J Suhonen, and J Toivanen. "Large-scale shell-model calculations of elastic and inelastic scattering rates of lightest supersymmetric particles (LSP) on I 127, Xe 129, Xe 131, and Cs 133 nuclei." In: *Phys. Rev. C* 79.4 (2009), p. 044302.

[113] Francesco Iachello, Lawrence M Krauss, and Giuseppe Maino. "Spin-dependent scattering of weakly interacting massive particles in heavy nuclei." In: *Physics Letters B* 254.1-2 (1991), pp. 220–224.

[114] T. W. Kornack. “A test of CPT and Lorentz Symmetry Using a K-3He Co-magnetometer.” PhD thesis. Princeton University, 2005.

[115] *Optical Magnetometry*. Cambridge University Press, 2013. DOI: 10.1017/CBO9780511846380.

[116] H. N. de Freitas, M. Oria, and M. Chevrollier. “Spectroscopy of cesium atoms adsorbing and desorbing at a dielectric surface.” In: *Applied Physics B* 75.6 (Nov. 2002), pp. 703–709. ISSN: 1432-0649. DOI: 10.1007/s00340-002-1029-y. URL: https://doi.org/10.1007/s00340-002-1029-y.

[117] W. Happer and A. C. Tam. “Effect of rapid spin exchange on the magnetic-resonance spectrum of alkali vapors.” In: *Phys. Rev. A* 16 (5 Nov. 1977), pp. 1877–1891. DOI: 10.1103/PhysRevA.16.1877. URL: https://link.aps.org/doi/10.1103/PhysRevA.16.1877.

[118] JC Allred, RN Lyman, TW Kornack, and Michael V Romalis. “High-sensitivity atomic magnetometer unaffected by spin-exchange relaxation.” In: *Phys. Rev. Lett.* 89.13 (2002), p. 130801.

[119] Ricardo Jimenez Martinez. “Microfabricated Spin Polarized Atomic Magnetometers.” PhD thesis. University of Colorado, 2013.

[120] S. Afach et al. “Characterization of the global network of optical magnetometers to search for exotic physics (GNOME).” In: *Physics of the Dark Universe* 22 (2018), pp. 162–180. ISSN: 2212-6864. DOI: https://doi.org/10.1016/j.dark.2018.10.002. URL: https://www.sciencedirect.com/science/article/pii/S2212686418301031.

[121] D. F. Jackson Kimball, J. Dudley, Y. Li, S. Thulasi, S. Pustelny, D. Budker, and M. Zolotorev. “Magnetic shielding and exotic spin-dependent interactions.” In: *Phys. Rev. D* 94 (2016), p. 082005.

[122] P. Włodarczyk, S. Pustelny, D. Budker, and M. Lipiński. “Multichannel data acquisition system with absolute time synchronization.” In: *Nucl. Instr. Meth. Phys. Res. A* 763 (2014), p. 150.

[123] Subhas C. Mukhopadhyay Asaf Grosz Michael J. Haji-Sheikh. *High Sensitivity Magnetometers*. Springer, Cham, 2017. ISBN: 978-3-319-34070-8. DOI: 10.1007/978-3-319-34070-8.

[124] Mikhail Padniuk, Marek Kopciuch, Riccardo Cipolletti, Arne Wickenbrock, Dmitry Budker, and Szymon Pustelny. “Response of atomic spin-based sensors to magnetic and nonmagnetic perturbations.” In: *Scientific Reports* 12.1 (Jan. 2022), p. 324. ISSN: 2045-2322. DOI: 10.1038/s41598-021-03609-w. URL: https://doi.org/10.1038/s41598-021-03609-w.

[125] The HDF Group. *Hierarchical Data Format, version 5*. www.hdfgroup.org. 1997-2022.

[126] Joseph A. Smiga. "Assessing the quality of a network of vector-field sensors." In: *The European Physical Journal D* 76.1 (Jan. 2022), p. 4. ISSN: 1434-6079. DOI: `10.1140/epjd/s10053-021-00328-9`. URL: `https://doi.org/10.1140/epjd/s10053-021-00328-9`.

[127] S. Pustelny et al. "The Global Network of Optical Magnetometers for Exotic physics (GNOME): A novel scheme to search for physics beyond the Standard Model." In: *Ann. Phys. (Berl.)* 525 (2013), p. 659.

[128] Joseph A. Smiga. "Theoretical aspects and data analysis for topological dark matter searches." PhD thesis. Johannes Gutenberg-Universität Mainz, 2021.

[129] N. Wyn Evans, Ciaran A. J. O'Hare, and Christopher McCabe. "Refinement of the standard halo model for dark matter searches in light of the Gaia Sausage." In: *Phys. Rev. D* 99.2 (2019), p. 023012. ISSN: 2470-0029. DOI: `10.1103/PhysRevD.99.023012`.

[130] Andrzej K. Drukier, Katherine Freese, and David N. Spergel. "Detecting cold dark-matter candidates." In: *Phys. Rev. D* 33 (12 June 1986), pp. 3495–3508. DOI: `10.1103/PhysRevD.33.3495`. URL: `https://link.aps.org/doi/10.1103/PhysRevD.33.3495`.

[131] B. M. Roberts, G. Blewitt, C. Dailey, and A. Derevianko. "Search for transient ultralight dark matter signatures with networks of precision measurement devices using a Bayesian statistics method." In: *Phys. Rev. D* 97 (8 Apr. 2018), p. 083009. DOI: `10.1103/PhysRevD.97.083009`. URL: `https://link.aps.org/doi/10.1103/PhysRevD.97.083009`.

[132] Patrick R Brady, Jolien D E Creighton, and Alan G Wiseman. "Upper limits on gravitational-wave signals based on loudest events." In: *Class. Quantum Grav.* 21.20 (Sept. 2004), S1775–S1781. DOI: `10.1088/0264-9381/21/20/020`. URL: `https://doi.org/10.1088/0264-9381/21/20/020`.

[133] Richard Swinbank and R. James Purser. "Fibonacci grids: A novel approach to global modelling." en. In: *Quarterly Journal of the Royal Meteorological Society* 132.619 (July 2006), pp. 1769–1793. ISSN: 00359009, 1477870X. DOI: `10.1256/qj.05.227`. URL: `http://doi.wiley.com/10.1256/qj.05.227` (visited on 12/04/2019).

[134] Benjamin M Roberts, Geoffrey Blewitt, Conner Dailey, Mac Murphy, Maxim Pospelov, Alex Rollings, Jeff Sherman, Wyatt Williams, and Andrei Derevianko. "Search for domain wall dark matter with atomic clocks on board global positioning system satellites." In: *Nat. Commun.* 8.1 (2017), pp. 1–9.

[135] B. P. Abbott et al. "GW150914: First results from the search for binary black hole coalescence with Advanced LIGO." In: *Phys. Rev. D* 93 (12 June 2016), p. 122003. DOI: `10.1103/PhysRevD.93.`

122003. URL: https://link.aps.org/doi/10.1103/PhysRevD.93.122003.

[136] Samantha A Usman et al. "The PyCBC search for gravitational waves from compact binary coalescence." In: *Class. Quantum Grav.* 33.21 (Oct. 2016), p. 215004. DOI: 10.1088/0264-9381/33/21/215004. URL: https://doi.org/10.1088/0264-9381/33/21/215004.

[137] Daniele S. M. Alves and Neal Weiner. "A viable QCD axion in the MeV mass range." In: *Journal of High Energy Physics* 2018.7 (July 2018), p. 92. ISSN: 1029-8479. DOI: 10.1007/JHEP07(2018)092. URL: https://doi.org/10.1007/JHEP07(2018)092.

[138] Jae Hyeok Chang, Rouven Essig, and Samuel D McDermott. "Supernova 1987A constraints on sub-GeV dark sectors, millicharged particles, the QCD axion, and an axion-like particle." In: *Journal of High Energy Physics* 2018.9 (2018), p. 51.

[139] Nitsan Bar, Kfir Blum, and Guido D'amico. "Is there a supernova bound on axions?" In: *Phys. Rev. D* 101.12 (2020), p. 123025.

[140] J. Eby, C. Kouvaris, N. G. Nielsen, and L. C. R. Wijewardhana. "Boson stars from self-interacting dark matter." In: *J. High Energy Phys.* 2016 (2016), p. 28.

[141] BM Roberts, P Delva, A Al-Masoudi, A Amy-Klein, C Baerentsen, CFA Baynham, E Benkler, S Bilicki, W Bowden, E Cantin, et al. "Search for transient variations of the fine structure constant and dark matter using fiber-linked optical atomic clocks." In: *arXiv preprint arXiv:1907.02661* (2019).

[142] Rees L McNally and Tanya Zelevinsky. "Constraining domain wall dark matter with a network of superconducting gravimeters and LIGO." In: *Eur. Phys. J. D* 74 (2020), pp. 1–6.

[143] Abhishek Banerjee, Dmitry Budker, Joshua Eby, Hyungjin Kim, and Gilad Perez. "Relaxion stars and their detection via atomic physics." In: *Commun. Phys.* 2.1 (2020).

[144] Abhishek Banerjee, Dmitry Budker, Joshua Eby, Victor V. Flambaum, Hyungjin Kim, Oleksii Matsedonskyi, and Gilad Perez. "Searching for Earth/Solar axion halos." In: *Journal of High Energy Physics* 2020.9 (Sept. 2020), p. 4. ISSN: 1029-8479. DOI: 10.1007/JHEP09(2020)004. URL: https://doi.org/10.1007/JHEP09(2020)004.

[145] J. W. Foster, N. L. Rodd, and B. R. Safdi. "Revealing the Dark Matter Halo with Axion Direct Detection." In: *Phys. Rev. D* 97.12 (2018), p. 123006.

[146] Alexander V Gramolin, Arne Wickenbrock, Deniz Aybas, Hendrik Bekker, Dmitry Budker, Gary P Centers, Nataniel L Figueroa, Derek F Jackson Kimball, and Alexander O Sushkov. "Spectral signatures of axionlike dark matter." In: *arXiv:2107.11948* (2021).

[147] Note that the spatial dependence for coherence lengths smaller than the Earth's diameter could also be exploited to look for UBDM, for which portable sensors could be employed as in Refs. [148, 149].

[148] Jacopo Grotti, Silvio Koller, Stefan Vogt, Sebastian Häfner, Uwe Sterr, Christian Lisdat, Heiner Denker, Christian Voigt, Ludger Timmen, Antoine Rolland, et al. “Geodesy and metrology with a transportable optical clock.” In: *Nature Physics* 14.5 (2018), p. 437.

[149] Masao Takamoto, Ichiro Ushijima, Noriaki Ohmae, Toshihiro Yahagi, Kensuke Kokado, Hisaaki Shinkai, and Hidetoshi Katori. “Test of general relativity by a pair of transportable optical lattice clocks.” In: *Nature Photonics* 14.7 (2020), pp. 411–415.

[150] Dmitry Budker, Peter W Graham, Micah Ledbetter, Surjeet Rajendran, and Alexander O Sushkov. “Proposal for a cosmic axion spin precession experiment (CASPEr).” In: *Phys. Rev. X* 4.2 (2014), p. 021030.

[151] Rodney Loudon. *The quantum theory of light*. Oxford New York: Oxford University Press, 2000. ISBN: 978-0198501763.

[152] Itay M. Bloch, Gil Ronen, Roy Shaham, Ori Katz, Tomer Volansky, and Or Katz. “New constraints on axion-like dark matter using a Floquet quantum detector.” In: *Science Advances* 8.5 (2022), eabl8919. DOI: `10.1126/sciadv.abl8919`. eprint: `https://www.science.org/doi/pdf/10.1126/sciadv.abl8919`. URL: `https://www.science.org/doi/abs/10.1126/sciadv.abl8919`.

[153] K. A. Olive and M. Pospelov. “Environmental dependence of masses and coupling constants.” In: *Phys. Rev. D* 77 (2008), p. 043524.

[154] William DeRocco, Peter W Graham, and Surjeet Rajendran. “Exploring the robustness of stellar cooling constraints on light particles.” In: *Phys. Rev. D* 102.7 (2020), p. 075015.

[155] Michael A Fedderke, Peter W Graham, Derek F Jackson Kimball, and Saarik Kalia. “The Earth as a transducer for dark-photon dark-matter detection.” In: *Phys. Rev. D* 104 (2021), p. 075023.

[156] Winfried Otto Schumann. “Über die strahlungslosen Eigenschwingungen einer leitenden Kugel, die von einer Luftschicht und einer Ionosphärenhülle umgeben ist.” In: *Z. Naturforsch. A* 7.2 (1952), p. 149.

[157] Wenxiang Hu, Matthew M Lawson, Dmitry Budker, Nataniel L Figueroa, Derek F Jackson Kimball, Allen P Mills, and Christian Voigt. “A network of superconducting gravimeters as a detector of matter with feeble nongravitational coupling.” In: *Eur. Phys. J. D* 74.6 (2020), p. 115.

[158] Adam M Dziewonski and Don L Anderson. “Preliminary reference Earth model.” In: *Phys. Earth Planet. Inter.* 25.4 (1981), p. 297.

[159] T. W. Kornack and M. V. Romalis. “Dynamics of Two Overlapping Spin Ensembles Interacting by Spin Exchange.” In: *Phys. Rev. Lett.* 89 (2002), p. 253002.

[160] T. W. Kornack, R. K. Ghosh, and M. V. Romalis. “Nuclear Spin Gyroscope Based on an Atomic Comagnetometer.” In: *Phys. Rev. Lett.* 95 (2005), p. 230801.

[161] Dongok Kim, Derek F. Jackson Kimball, Hector Masia-Roig, Joseph A. Smiga, Arne Wickenbrock, Dmitry Budker, Younggeun Kim, Yun Chang Shin, and Yannis K. Semertzidis. “A machine learning algorithm for direct detection of axion-like particle domain walls.” In: *Physics of the Dark Universe* 37 (2022), p. 101118. ISSN: 2212-6864. DOI: `https://doi.org/10.1016/j.dark.2022.101118`. URL: `https://www.sciencedirect.com/science/article/pii/S2212686422000917`.

[162] Zsigmond Benkő, Tamás Bábel, and Zoltán Somogyvári. “Model-free detection of unique events in time series.” In: *Scientific Reports* 12.1 (Jan. 2022), p. 227. ISSN: 2045-2322. DOI: `10.1038/s41598-021-03526-y`. URL: `https://doi.org/10.1038/s41598-021-03526-y`.

[163] Conner Dailey, Colin Bradley, Derek F Jackson Kimball, Ibrahim Sulai, Szymon Pustelny, Arne Wickenbrock, and Andrei Derevianko. “Quantum sensor networks as exotic field telescopes for multi-messenger astronomy.” In: *Nat. Astron.* (2020).

DECLARATION

Herewith I, **Hector Masia Roig** declare that the present thesis, entitled: **Search for exotic spin couplings with the Global Network of Optical Magnetometers for Exotic physics searches**. I confirm that:

- This work was done wholly or mainly while in candidature for a research degree at the Johannes Gutenberg University.
- Where any part of this thesis has previously been submitted for a degree or any other qualification at the Johannes Gutenberg University or any other institution, this has been clearly stated.
- Where I have consulted the published work of others, this is always clearly attributed.
- Where I have quoted from the work of others, the source is always given. With the exception of such quotations, this thesis is entirely my own work.
- I have acknowledged all main sources of help.
- Where the thesis is based on work done by myself jointly with others, I have made clear exactly what was done by others and what I have contributed myself.

Mainz , May 2023

Hector Masia Roig